1-1-2002

Factors affecting the bit error rate performance of the indoor radio propagation channel for 2.3-2.5 GHz frequency band

Edward A. Walker

Edith Cowan University

Copyright Warning

USE OF THESIS

The Use of Thesis statement is not included in this version of the thesis.

Edith Cowan University

and

Cooperative Research Centre for Broadband Telecommunications and networking

Factors Affecting the Bit Error Rate Performance of the Indoor Radio Propagation Channel for 2.3 - 2.5 GHz Frequency Band

Edward A. Walker (M.App.Sc B.App.Sc)

This thesis is presented as part of the

requirements for the award of the

Degree of Doctor of Philosophy

of

Edith Cowan University

Date of submission: 9th January 2002

Acknowledgements

The preparation of this thesis has required not only a work commitment by myself for four years, but also continuous support and understanding from my wife Heather and granddaughter Brixley throughout this time period. They have had the number of hours we shared together reduced, with the demands of the thesis often placing a time restriction on my participation in family leisure activities. For their significant contribution towards its completion I offer my gratitude. I have also received advice and encouragement from Dr Tadeusz Wysoski, and Dr Hans Jurgen Zepernick, who were thesis supervisors for the first three years of the research work, and I thank them both for the support given. The gathering of data which was required for statistical analysis formed an important input requirement for the preparation of the thesis, this created a need for a measurement venue, and also the extensive use of a variety of specialised measurement equipment. The venue and all the necessary measurement equipment was kindly made available by the Co-operative Research Centre for Broadband Telecommunications and Networking, which is located at Curtin University of Technology Perth Australia. For the assistance and generosity of the staff at the centre I offer my sincere thanks. Dr Daryoush Habibi supervised the fourth and final year of research and the thesis preparation. For Dr Habibi's encouragement, understanding, support, and exceptional patience, I extend my sincere gratitude. Finally I offer my appreciation to Mr Brendon Moffatt for his generous assistance with the layout and presentation format of the print and figures for the finished thesis document.

Abstract

The use of wireless in buildings based on microwave radio technology has recently become a viable alternative to the traditional wired transmission media. Because of the portable nature of radio transceivers, the need for extensive cabling of buildings with either twisted pair, coaxial, or optical fibre cable is eliminated. This is particularly desirable where high user mobility occurs and existing wiring is not in place, or buildings are heritage in nature and extensive cabling is seen as intrusive. Economic analysis has also shown that significant labour cost savings can result by using a radio system or a hybrid mix of cable and radio for personal communication. The use of wireless systems within buildings introduces a new physical radio wave propagation medium, namely the indoor radio propagation channel. This physical medium has significantly different characteristics to some of the other forms of radio channels where elevated antennas, longer propagation path distances, and often minimally obstructed paths between transmit and receive antenna are common. Radio waves transmitted over the indoor channel at microwave frequencies behave much like light rays, they are blocked, scattered, and reflected by objects in the environment. As a direct result of this several phenomena unique to this form of physical medium become apparent, and they must be accounted for in the design and modelling of the indoor radio propagation channel transmission performance. In this thesis we analyse and characterise the indoor radio channel as a physical medium for data transmission. The research focuses on the influence of the radio physics aspects of an indoor microwave channel on the data transmission quality. We identify the associated statistical error performance for both time varying and temporally stationary indoor channels. Together with the theoretical analysis of the channel, a series of propagation measurements within buildings are completed to permit empirical validation of the theoretical predictions of how the indoor microwave

channel should perform. The measurements are performed in the frequency range 2.3-2.5 GHz, which includes the 2.4-2.4835 GHz band allocated by spectrum management authorities for industrial scientific and medical radio use, (ISM band).

As a direct result of our measurements, statistics related to channel noise, fading, and impulse response for the indoor microwave channel are obtained. The relationship between data transmission error statistics and the aforementioned phenomena is quantified and statistically analysed for the indoor radio channel and phase shift keyed (PSK) modulation. The results obtained from this research provide input data for the development of a simulation model of an indoor wireless mobile channel. Our measurements identify microwave ovens as a channel noise source of sufficient magnitude to corrupt data transmission in the ISM band, and an in depth analysis of the affect of noise emissions from operational microwave ovens on PSK modulation is presented in this thesis. As a result of this analysis, the estimated data error rates are calculated. Channel fading measurements provide results that will be used as the input data for the design of antennas for use on the indoor microwave channel. We also show that a data rate of eight megabits/second is possible over the typical indoor radio channel, with no requirement for adaptive delay equalisation to counter multipath signal delay spread.

Declaration

I certify that this thesis does not incorporate without acknowledgement any material previously submitted for a degree or diploma in any institution of higher education; and that to the best of my knowledge and belief it does not contain any material previously published or written by another person except where due reference is made in the text.

Signature

Date 16 OCTOBER 2002

Contents

Acronyms

AC	Alternating Current.
AF	Antenna Factor.
ADF	Average Duration of Fades.
AM	Amplitude Modulation.
AWGN	Additive White Gaussian Noise.
BER	Bit Error Rate.
BPSK	Binary Phase Shift Keying.
CDF	Cumulative Distribution Function.
CW	Continuous Wave.
dB	Decibel.
dBm	Decibels relative to a 1 milliwatt power level.
dBμV/m	Decibels relative to 1 microvolt per metre.
DC	Direct Current.

DFIR	Diffused Infra-red.
DSSS	Direct Sequence Spread Spectrum.
E field	Electric field.
EVM	Error Vector Magnitude.
FHSS	Frequency Hopping Spread Spectrum.
GHz	Gigahertz (10^9 Hertz).
Hz	Hertz (cycles/second).
IEEE	Institute of Electrical and Electronic Engineers.
IFT	Inverse Fourier Transform.
I-Q	In phase and Quadrature.
ISI	Inter Symbol Interference.
ISM	Industrial Scientific and Medical.
kHz	kilohertz (10^3 Hertz).
LCR	Level Crossing Rate.
LOS	Line Of Sight.
MAC	Media Access protocol.
MHz	Megahertz (10^6 Hertz).

MSK	Minimum Shift Keying.
NF	Noise Figure.
ns	nanosecond (10^{-9} seconds).
OQPSK	Offset Quadrature Phase Shift Keying.
QPSK	Quadrature Phase Shift Keying.
RBW	Resolution Band Width.
RF	Radio Frequency.
rms	root mean square.
RX	Receive.
SNR	Signal to Noise Ratio.
S-parameter	Scattering parameter.
TX	Transmit.
VCATT	Voltage Controlled Attenuator.
VSA	Vector Signal Analyser.
WLANs	Wireless Local Area Networks.
8-PSK	8 level Phase Shift Keying.

Symbols

a	Cathode radius of a microwave oven magnetron.
A	The peak amplitude of received signal envelope (R) in a fading channel.
A_R	The directional characteristic of a receive antenna.
A_{Reff}	The receive antenna effective aperture.
A_T	The directional characteristic of a transmit antenna.
AF	Antenna Factor.
b	Anode radius of a microwave oven magnetron.
B	Bin number for calculating the empirical CDF of amplitude fading distributions.
B_f	Bandwidth of Measurement Filter.
c	Speed of light in a vacuum.
C	Electron charge to mass ratio (e/m).

$C_{Rice}(R)$	The Rician CDF of received signal envelope (R) in a fading channel.
B_0	Magnetic Field Intensity (Magnetron Permanent Magnet).
d	rms delayspread (σ_t) normalised to symbol period (T).
d'	rms delayspread (σ_t) normalised to bit period (T_b).
d_{ij}	Euclidean distance between the I and j signal points within a constellation.
e	Charge on an electron.
erfc(x)	The complementary error function.
E_b	Energy per bit.
E_i	Received electric field intensity if i^{th} path.
E(t,z)	Electric field intensity as a function of time (t) in direction (z).
E_R	Received electric field intensity.
E_T	Transmitted electric field intensity.
f	Frequency.
f_c	Carrier wave frequency.
G_r	Maximum directive gain of the receive antenna relative to an isotropic antenna.

$G_x(f)$	Noise power spectral density function.
$h_c(t)$	Impulse response of a channel.
$h_r(t)$	Impulse response of the receive filter.
$h_t(t)$	Impulse response of the transmit filter.
$h(\tau,r)$	Impulse response of channel at range (r).
H(t,z)	Magnetic field intensity as a function of time (t) in direction (z).
k	Rician k-factor variable.
m	Mass of an electron.
L	A specified signal level of a received signal envelope (R) in a fading channel.
$n_o(t)$	Magnitude of additive channel noise at the receive filter output.
$n_i(t)$	In-phase component of additive channel noise at the receive filter output.
$n_q(t)$	Quadrature component of additive channel noise at the receive filter output.
N	Total envelope-fading crossings with positive slope at a specified signal level (L).
N_L	Level crossing rate at a specific level for a fading record of T_F seconds duration.

P_{AV}	The time average power density per unit area.
P_{rms}	The root mean square (rms) power flow per unit area.
P_R	The receive power level at range (r) from the transmit antenna.
P_T	The transmit power level from an antenna.
$P(t,z)$	The power as a function of time (t) in direction (z).
$P_{e\ BPSK}$	The average error probability for BPSK modulation.
$P_S(\varepsilon/s_i)$	The probability of error for a particular modulation signal (s_i).
$Q(x)$	The Q-function.
r	Range or lineal distance between transmit and receive antennae.
r	Radial distance from cathode for microwave oven magnetron, where $a \leq r \leq b$.
R	The reflection coefficient.
R_i	The reflection coefficient of the i^{th} path.
R_S	Radiation resistance of an antenna.
R_{UNAMB}	Range where $W_R(t)$ can be unambiguously related to a particular transmitted pulse.
S_1 & S_2	Antipodal signal vectors for BPSK constellation.
S_{dev}	Standard deviation.

t_j	Time duration of each individual fade at level (L).
$\bar{t}_L$	Average duration of fades at level (L).
T	Time period for one symbol.
T_b	Time period for one bit.
T_F	Total time duration for a fading record.
T_m	Time period for minimum sample record length.
v	Electron velocity between cathode and anode within a microwave oven magnetron.
V_a	Anode voltage applied to microwave ovens magnetron relative to cathode.
V_L	Voltage across load impedance Z_L connected to an antenna.
$V(r)$	Voltage potential at radius (r) from the cathode of a microwave ovens magnetron.
W_R	The power available at the receive antenna terminals.
Z_S	Antenna impedance.
α_{Ri}	Azimuth angle of incidence at the receive antenna with respect to the last point of scatter.
α_{Ti}	Azimuth angle of exit from the transmit antenna with respect to the first point of scatter (or reflection).

β	Phase constant.
β_{RI}	Elevation angle of incidence at the receive antenna with respect to the last point of scatter (or reflection).
β_{TI}	Elevation angle of exit at the transmit antenna with respect to the last point of scatter (or reflection).
$\delta(t)$	dirac delta function.
ϵ	A mediums permittivity.
ϵ_0	Permittivity of free space.
ϵ_r	Relative permittivity.
η	Intrinsic impedance of a medium, (120π for free space).
λ	Wavelength.
μ	A mediums permeability.
μ_0	Permeability of free space.
μ_r	Relative permeability.
ξ	Desired error limit for chosen noise filter measurement bandwidth.
σ	Conductivity of a medium.
$\sigma_{measured}$	rms delay spread of measurement.

σ_τ	rms delay spread.
σ_{system}	Calibration value of rms delay spread for the measurement system.
τ_i	Propagation delay of i^{th} path.
τ_m	Mean excess delay.
$\psi(r,\phi)$	Magnetron field component.
ω	Angular frequency.
ω_e	Angular velocity of an electron within a microwave oven magnetron.
χ	Fading variable.

Chapter 1

Introduction

The rapidly growing trend towards integrated voice and data telecommunications in our very mobile society has created the need for personal communications systems that will operate reliably inside buildings as well as outdoors. Analysis of indoor radio channel characteristics is important for the design and development of personal communications systems, and of particular interest is the frequency band of 2.4-2.4835 GHz which is one of the unlicensed Industrial Scientific and Medical (ISM) bands. Both Direct Sequence Spread Spectrum (DSSS) and Frequency Hopping Spread Spectrum (FHSS) systems operate in the 2.4-2.4835 GHz ISM band, and this band is selected in preference to the 918-926 MHz and 5.725-5.850 GHz ISM bands because of its wide availability in many parts of the world. This band has more than 80 MHz of bandwidth available for the transmission of data, and is also more cost effective for system implementation [1] when compared with frequencies that are a few GHz higher. The Institute of Electrical and Electronic Engineers (IEEE) standard IEEE 802.11 relates to the physical medium and the media access protocol (MAC) for DSSS, FHSS and diffused infra-red (DFIR) technologies using the ISM bands as the radio channel. The IEEE 802.11 standard supports the use of DSSS employing either binary phase shift keying (BPSK), or quaternary phase shift keying (QPSK) modulation for data rates of 1 and 2 megabits per second respectively. The suitability of this 2.4-2.4835 GHz ISM frequency band for the transmission of high speed data using BPSK and QPSK modulation as an integral part of networks such as Wireless Local Area Networks (WLANs) is the focus of this thesis.

In order to design reliable indoor communication systems in this 2.4 GHz band the channels radio propagation characteristics must be known. Two of the key characteristics are additive channel noise and the fading performance over the channel. The first of these key characteristics (additive channel noise for the 2.4 GHz band) has not been evaluated with sufficient rigour as to determine the nature and effect of noise sources that are external to personal communications system itself on the bit error rate of the data transmitted over the indoor radio channel. The sources of noise external to the personal communications system can be attributed to four main areas, all of which are considered in this thesis. In particular the measurement and modelling of one of these areas which is termed "man-made noise" is still embryonic and "as more data are obtained, the models will progress to allow a more complete characterisation of the man made noise in a particular environment by measuring just a few parameters in that locale" [2]. In order to progress the modelling of noise in the 2.4 GHz band being studied, a series of measurements have been completed at a selected range of locations. These measurements identify man-made noise generated by operational microwave ovens as a source of considerable concern [3] [4] for this band, and an in depth evaluation of the impact of this form of channel noise on the received data bit error rate is one objective of this thesis.

The second key characteristic is the fading performance over the indoor channel. There are two distinct types of fading; these being "flat fading" and "frequency selective fading". For the indoor channel flat fading occurs when a transmitted wave from a fixed base station antenna located within the channel scatters off many obstacles which are relatively close to the mobile unit receiving the wave. In this case a number of scattered rays arrive at the mobile unit from many directions with varying amplitude and phase. Because of the close proximity of the scattering objects to the receive mobile, the overall delay of each scattered path is approximately equal and the delay spread is minimal. Dependent on the amplitude and phase of the rays the combined sum may add destructively or constructively to provide either cancellation or reinforcement of the total output signal at the receive antenna. Flat fade depth, number, and duration below a specific receive power level are a function of Doppler frequency which is in turn proportional to carrier frequency and motion within the channel. This motion can be a result of the movement of the mobile (or portable) unit

itself, or as often the case the movement of people or inanimate objects close to the receiving antenna of the portable unit. The fading performance of the indoor radio channel at the 2.4 GHz frequency is statistically analysed from the data obtained from a controlled series of fading measurements performed for an indoor radio propagation channel where the Doppler shift is deliberately introduced by the motion of varying numbers of people moving in similar manner in close proximity to the portable units receive antenna.

The wide-band nature of the indoor radio propagation channel and the many reflective surfaces that may be encountered by the transmitted radio signal such as floor, roof, walls, furniture, and other inanimate objects, provide a static environment that creates multiple paths between the transmit and receive antenna. Introduce to this the temporal variations caused mainly by the motion of people within the indoor propagation channel, then a non-static resultant signal appears at the receive antenna output terminals. The resultant non-static signal is a vector summation of radio signals that propagate over many paths. These signals undergo a time dispersion caused by the unequal path lengths traversed, and have their amplitude and phase further modified by the nature of any reflective surfaces encountered before they intercept the receive antenna, and therefore differ in amplitude and phase. The resultant frequency selective fading caused by this multipath time delay spread degrades digital communication channels by causing intersymbol interference (ISI) [5]. The time dispersion for the indoor radio propagation channel is often characterised by impulse response measurements of the channel, and the computation of a numeric parameter from these measurements termed the delay spread, σ_τ, which is the power weighted root mean square (rms) width of the indoor channels impulse response. Impulse response measurements have been performed for many indoor propagation situations, including laboratories, offices, factories, lecture theatres, and others for both cluttered and uncluttered situations [6 – 30]. The size and construction materials employed for these measured indoor venues also varied widely. Omni-directional transmit and receive antennas such as dipoles or their equivalent monopoles of like radiation pattern and vertical (E field) polarisation have been used for the majority of reported impulse response measurements [6 – 10] [15] [18 – 21] [24] [28] [30]. This is a logical approach that has been taken in view of the fact that most personal

communications equipment in current use such as mobile telephones, cordless telephones, and WLAN portables, do indeed employ antennas with vertical polarisation for their transmit and receive antennae. It is widely accepted that when σ_τ becomes an appreciable fraction of the data symbol duration then ISI results in an irreducible error floor, where irreducible errors are defined as errors that occur at very high signal to noise ratio (SNR) [5]. Modelling and simulation of the affect of ISI on bit error rate (BER) has provided curves and tables that show the expected relationship between σ_τ and BER [2] [31 – 35]. The conclusions that can be drawn from these curves and tables is that for indoor radio system design σ_τ must be kept as low as possible if high symbol rate transmission is required. However a comprehensive theoretical treatise on σ_τ , ISI, and BER is still forthcoming, and a more precise prediction of digital system performance awaits verification of a relationship between σ_τ and the digital system error performance [7].

In order to gain insight into the BER performance of this 2.4-2.4835 GHz ISM frequency band a series of data gathering measurements relative to the indoor radio channel and for the frequency range of 2.3-2.5 GHz have been undertaken and statistically evaluated as a part of this thesis to enable predictions of the performance BER of the channel. The evaluation of measured data for channel noise and interference generated by operational microwave ovens is an original contribution presented in this thesis.

The statistics derived from the measured data of this thesis have been presented in conference papers [4] [36] [37], and as part of a book [38]. The obtained statistics have also been used as the input data for channel modelling and simulation exercises [39].

The content of the thesis addresses different aspects in the modelling and analysis of the physical channel as a medium for high speed data transmission. The thesis is organised as follows:

In Chapter 3, we identify the phenomena that affect the BER for data transmissions over the indoor radio channel and their statistical relationship to BER for digital modulation. Mathematical equations are identified that are applicable to the

computation of the statistics related to influence of noise and impulse response on average BER for digital modulation.

Chapter 4 provides a detailed description of how additive channel noise is characterised. We discuss the measurement instrumentation and methodology employed to obtain data on the statistical nature of systematic noise which is noise inherent within our measurement systems and how to quantify this noise. We also describe the measurement of non-systematic noise which is noise that enters the transmission system via the receive antenna. The identification and characterisation of this form of noise is an important objective of this thesis. The results of our measurements are presented and statistically analysed.

Chapter 5 characterises noise emitted from operational microwave ovens. The performance of the magnetron and its influence on electromagnetic radiation emitted from the oven is analysed. The occurrence rate of noise bursts, the affect of load variation in the oven cavity, and magnetron frequency drift statistics are investigated.

In Chapter 6 the characterisation of channel fading is introduced. We identify the best statistical model for the most common form of indoor channel fading where the motion of people about the portable unit produces the fading phenomena. Data obtained from a series of measurements where the controlled motion of people about the receive antenna in an indoor situation are statistically evaluated, and numerical results calculated and compared with known mathematical probability distributions for best fit.

Chapter 7 provides a detailed analysis of predicted BER for digital modulation. These predictions are based on statistics calculated from the measurement data. BER performance curves are presented and discussed.

Finally in Chapter 8 we summarise the work contained in this thesis and present our conclusions.

In Appendix F we analyse the impulse response of the indoor venue where the fading measurements were undertaken. The multipath rms delay spread, σ_τ, is calculated from measurements for various nominated antenna placements. Then the BER

performance for the same antenna placements is predicted from the analysis of the measurements obtained by the cyclic transmission of a high speed data sequence over the indoor channel.

Chapter 2

Literature Review

In this Chapter a review of published literature on the performance of the indoor radio propagation channel is presented, with particular attention given to the frequency band of 2.3-2.5 GHz, the frequency band examined within this thesis. A variety of papers on channel fading and noise are reviewed. The review includes published literature on channel fading at frequencies other than the 2.3-2.5 GHz band as the fading mechanisms and their analysis are applicable to the indoor radio propagation channel at all frequencies. Noise measurement data and analysis however is restricted to the 2.3-2.5 GHz band of interest. This is because of the significant differences that relate to noise sources and the effective power levels of the noise generated by these sources for different spectral bands. The literature of relevance is included as part of this thesis in Chapter 9 references and a summary of the findings taken from this literature is presented here for three broad measurement and analysis areas of "Temporal Fading", "Impulse Response", and "Noise".

2.1 Temporal Fading

Reference [50] provides statistical analysis of measured data for temporal variations of received signal at 1100 MHz for an indoor radio propagation channel. The measurements were carried out in an office environment with four transmitter / receiver separation distances of 5, 10, 20, and 30 metres. The effects of controlled degrees of motion of people moving within the channel were evaluated. The measurement data was gathered for 0, 1, 2, 3, or 4 individuals walking around the "high" antenna only, around the "low" antenna only, and both antennas. A total of

192 one minute readings of CW envelope fading waveforms with both the base station (high located) antenna and portable (low located) antenna stationary, and the effects of controlled degrees of motion by the individuals were investigated.

The analysis shows that temporal variations are more noticeable for motion around the portable antenna, as compared to motion around the base antenna. A study of the temporal fading waveform also indicated that changes in the received signal level and the dynamic range of fluctuations increased when the number of people around the portable antenna increased from one to two, and from two to three. However the changes were less noticeable for an increase from three to four persons (a saturation phenomenon was observed for most cases). Reference [50] does not provide data on the height of the base or portable antennae, or the nature of the controlled motion such as velocity and path of the individuals moving within the channel during the measurements. It is not evident from [50] if the received signal is static when the motion of individuals is reduced to zero within the channel, although the comment is made that measurements were taken at night to "minimise all unplanned motion in the environment". Maximum fade depths of 25-30 dB relative to mean received power were measured.

Reference [10] presents impulse response parameters as well as envelope fading data for two frequencies of 900 MHz and 1.75 GHz. The data for analysis is gathered at two indoor channel locations. The measurements were conducted during daytime on weekdays, with personnel moving throughout the buildings as usual. The primary purpose of the measurements was to compare 900 MHz and 1.75 GHz band propagation conditions and analyse fading distributions. For the 900 MHz measurements [10] concluded from data analysis that "fading distributions were found to be Rician in all cases, even though there was no line of sight between the transmitter and receiver. For mobile channels, Rayleigh fading would be expected under such conditions". For thirty different transmitter locations associated with the 910 MHz measurements, the average fading range was 25 dB, the maximum was 35 dB, and the minimum was 14 dB. Rician theoretical distributions that best fit the experimental distributions corresponded to k values between –1 and –16 dB. For the nine transmit locations used during the 1.75 GHz experiments the maximum range of envelope fading was 42 dB, the average was 35 dB, and the minimum was 22 dB.

Three of the computed envelope fading distributions were Rayleigh, the remainder being Rician with k values between –6 to –8 dB. Reference [10] identifies "plenty of activity" around the transmit location for the portable unit (caused by people in motion) as a fading factor. Reference [10] also found that for transmit locations remote from activity "it was invariably found that at 1.75 GHz, the fading range was greater, and fading occurred at more frequent intervals than fading at 910 MHz".

Reference [41] provides an analysis of a range of measurement and modelling efforts on the indoor radio channel by many researchers. The author of [41] concludes that for a number of measurements channels are temporally stationary, or quasi stationary has either been observed or assumed in advance. Other experiments have shown that the indoor channel is "quasistatic" or "wide-sense stationary", only if data is collected over short intervals of time. Extensive CW measurements around the 1 GHz frequency in five factory environments and also in office buildings have shown that even in the absence of a direct LOS path between transmitter and receiver, the temporal fading data show good fit to the Rician distribution. Another work reporting measurements at 60 GHz, however, indicates that with no LOS path the CW envelope distribution is nearly Rayleigh.

A measurement system for indoors narrow-band radio propagation at 1700 MHz is described in reference [55]. The measurements performed within a corridor and later a room identified the importance people obstructing the LOS path has on the received signal level.

Reference [60] investigates the effects of radio wave polarisation in indoor radio propagation channels. It concludes from measurements using vertical, horizontal, and circular polarisation that "in practical systems where a strategy to reduce fade depth is required, there does not appear to be any advantage to circular polarisation in the narrow-band channel studied herein". Reference [60] further states that "measurements were halted when people were moving around. This was found to be important, as movement in certain areas of reflection, even removed from the test location, could change the null's significantly".

Reference [74] reports the results of measurements and analysis of the indoor radio propagation channel at 20 GHz. It found that the effect of "people moving in the vicinity of the receiver had very different effect on the signal than at the transmitter in terms of fade duration and severity". A person moving close to the transmitter is capable of causing fades of up to 16 dB for the duration of the time that they heavily obstruct the receiving antenna aperture. Reference [74] found that when the person is at some point between the two antennas, the fades are typically much less severe (typically 6-10 dB), however more frequent.

Reference [72] found "the effects of people on path loss, when compared to results for an empty room, is small. For LOS situations the effect is negligible". Reference [72] also with respect to the presence of people determines "no clear difference in behaviour was found for the three frequencies 2.4, 4.75, and 11.5 GHz".

2.2 Conclusions from Temporal Fading Literature Review

From the literature review it is evident that the presence of people within the indoor radio propagation channel significantly influence the signal level obtained at the receiver. The motion and number of people within the channel has been determined as a factor worthy of considerable study, with some contradiction on the severity of temporal fading as caused by people within the indoor channel evident between reference [72] and [60], [74], and [50]. It can be concluded that further analysis is needed to advance knowledge on the fading influence the presence of people have on indoor radio propagation for the 2.3-2.5 GHz band.

The influence of people within the channel can only be determined by the evaluation of data gathered from a controlled set of measurements. Care must be taken in the selection of measurement venue to ensure that only the presence and motion of people within the channel affect results. Also there is a requirement to determine if the results are venue specific, that is, only applicable for indoor propagation fading predictions at one venue and of little relevancy at others. It has been generally accepted that for characterisation of indoor channel impulse response large data gathering exercises

across a variety of venues is required to develop statistical models of indoor channel delay-spread for a range of venue sizes and types. This is intuitively supported as the distance traversed by multipath reflections within the indoor channel varies with the physical room dimensions of the various sized venues. There is however no research data evident within this literature review that identifies clear statistical variation between temporal fading data gathered in varying sized and types of indoor channel venues with people present, and or in motion. In particular of considerable interest is the influence of people moving about the portable or mobile terminal with its antenna generally located at desk height or generally not exceeding the height of a person. Whereas the base station antenna for the indoor radio link is in most cases mounted clear of obstructions at a height exceeding the tallest person. This being typically the case for wireless LANs as used in conference rooms, lecture theatres, classrooms and other commercial enterprise locations. It is therefore possible that the temporal fading may be primarily attributed to motion or activity in the vicinity of the mobile or portable terminal antenna, and therefore a portable terminal proximity phenomenon. This fading mechanism may, unlike delay-spread, be relatively independent of indoor channel venue size and type.

In this thesis these possibilities will be evaluated and measurement data statistically analysed with the objective of advancing the understanding of indoor channel temporal fading performance under conditions of motion by people within the channel.

2.3 Impulse Response

Many researchers have published literature detailing measured impulse response profiles and their associated statistical parameters such as rms delay spread. Reference [10] provides impulse response profiles for indoor propagation channels at 910 MHz and 1.75 GHz within two buildings. Impulse responses, as expected, differed for both buildings with rms delay spreads being "slightly greater at 1.75 GHz for over 90 percent of the transmit locations. The median rms delay spread being 28 ns for the 1.7 GHz band, as compared to a median of 26 ns for the 900 MHz band. In the other

building delay spreads in the 900 MHz band were marginally greater for 70 percent of the transmit locations".

Reference [74] provides results of impulse response measurements for two different rooms and a corridor at 20 GHz frequency with transmit and receive antennae being directional horn type separated by distances of 4, 6, or 7 metres. A table presented in reference [74] gives experimental rms delay spread averaged for each combination of distance and location. The mean value of rms delay spread varied very little between all locations with a range of values between 15.8 and 17.1 ns.

In reference [16] the results of extensive multipath propagation measurements at two office buildings are reported, a database of 12,000 impulse profiles was established for analysis, and results for rms delay spread are determined. The range of rms delay spread is between 10 and 20 ns, and the average delay spread consistently increases when the transmit receive antenna separation is increased.

Reference [15] analyses measurements of signal level and rms delay spread performed in a "large commercial metropolitan building" at 850 MHz, 1.9 GHz, 4.0 GHz, and 5.8 GHz. Transmit and receive antennae were wide-band omnidirectional azimuthal units. Measurement results for this large building showed the rms delay spread to be always less than 120 ns, and to be statistically equal at the four frequencies.

Measurement analysis of rms delay spread in two modern office buildings is presented in reference [22]. Wide-band discone antennae are employed and results indicated that the rms delay spread is typically between 18 and 35 ns. The data for this analysis contained 12,000 measurements, 6,000 measurements for each building.

Delay spread measurements within a single floor of a building for both LOS and paths between transmit and receive antennae obstructed by internal partitioning are presented in reference [20]. Results show lowest rms delay spread for LOS measurements being typically less than 22 ns for 95 % of location measurements. Obstructed paths (with at least one wall between transmit and receive antennae) exhibited higher values of rms delay spread, typically less than 42 ns for 95 % of location measurements.

Reference [64] presents a graphical user interface program that uses a ray-tracing algorithm to predict the radio propagation in the indoor radio channel from the layout of the floor plan. The program allows the user to interactively specify the location of the walls in the floor plan, the type of material in the construction, and the location of transmit and receive antennae. Eight rooms on the second floor of a building were used in the computer program modelling, and the results compared with measurement data gathered for each room in the 0.9 GHz to 1.1 GHz range. Results from modelling were found to be relatively close to measurement results for each room. The rms delay spread values from measurements ranging from 15.7 ns to 29.2 ns for the eight rooms. Reference [19] further models the impulse response from measurements for this same indoor radio propagation channel as modelled by [64] using different antennae locations. The experimental values obtained for rms delay spread in [19] ranging between 19.11 ns to 46.92 ns.

Reference [29] summarises in table form (from measured results) the median and maximum delay spreads for a variety of buildings. These include office buildings of brick and concrete construction, and factories with LOS and obstructed propagation paths. Median rms delay spreads are in the range 26 ns to 30 ns for office buildings, and 96 ns to 105 ns for factories.

A large data gathering and statistical modelling exercise of rms delay spread is presented in reference [77]. The extensive multipath propagation measurements were carried out at two office buildings. The database included 12,000 estimates of the channels impulse response. Transmit to receive antenna separations of 5, 10, 20, and 30 metres were evaluated in the two buildings, with the 12,000 estimates being used to determine the statistical properties of rms delay spread. Values for rms delay spread were found to be typically between 10 and 50 ns, with the mean value in the 20 to 30 ns range. The rms delay spread also showed a clear dependence on transmit receive antennae separation. For a threshold level of 30 dB the mean rms delay spread increased from 16.9 to 35.1 ns for the first building, and from 17.5 to 26.6 ns for the second building as antennae spacings increased from 5 to 30 metres.

Results from propagation measurements conducted in an indoor office environment at 2.4, 4.75, and 11.5 GHz is presented in reference [72]. The data were obtained in

small clusters of six measurements using a coherent wide-band measurement system. The receive antenna height was maintained at 1.5 metres for all measurements, the transmit antenna was set firstly at 1.5 metres then 3 metres to compare the effect on data of elevation at one end of the test link. Measurement results for three office rooms of equal size, a conference room of larger dimensions, a laboratory room, and a hallway are analysed. Results showed that in LOS channels the height of the transmit antenna "only slightly affects mean rms delay spread". However for obstructed direct path situations the lowering of transmit antenna height "yields an increase of both mean rms delay spread and the standard deviation of rms delay spread". Results for the conference room for LOS measurements with transmit antenna set at 3 metres and receive antenna at 1.5 metres show a rms delay spread value of 14.9 ns, which increased to 21.1 ns when the path between the transmit and receive antennae was obstructed by furniture. From analysis of all measurement data presented in [72] the rms delay spread was in the range 5.4 to 21.6 ns, and predicably related to room dimensions.

Reference [52] provides a review on radio propagation into and within buildings. The review looks at eight classifications of buildings:

Class 1: Residential houses in suburban areas.

Class 2: Residential houses in urban areas.

Class 3: Office buildings in suburban areas.

Class 4: Office buildings in urban areas.

Class 5: Factory buildings with heavy machinery.

Class 6: Other factory buildings, sports halls, exhibition centres.

Class 7: Open environment, e.g. railway stations, airports, etc.

Class 8: Underground, e.g. subways, underground streets, etc.

For classifications 1, 3, 4, 5, and 6 typical and worst case values of rms delay spread derived from measurement data is presented as follows:

Class 1: Typical rms delay spread (150 ns). Worst case rms delay spread (420 ns).

Class 3: Typical rms delay spread (25-125 ns). Worst case rms delay spread (40-320 ns).

Class 4: Typical rms delay spread (25-50 ns). Worst case rms delay spread (100 ns).

Class 5: Typical rms delay spread (19-105 ns). Worst case rms delay spread (40-300 ns).

Class 6: Typical rms delay spread (15-20 ns). Worst case rms delay spread (40-146 ns).

Reference [52] found no published measured data for classifications 2, 7, and 8 for typical and worst case rms delay spread.

2.4 Conclusions from Impulse Response Literature Review

The measurement of impulse response for the indoor radio propagation channel by many researchers has provided data on rms delay spread for a variety of venues. Results are consistent and predictable in most cases when the dimensions of the measurement venue and the nature of the presence or absence of a LOS path between transmit and receive antennae is considered. Based on the rms delay spread value obtained for the venues several researchers have used this value as the prime input variable in the mathematical modelling of the BER probability for data transmitted over the link at various bit rates in the presence of delay spread. Reference [5] provides a treatise on the effects of time delay spread on BER for portable radio communication channels with digital modulation, and concludes that significant error rate only occurs when the time value of the rms delay spread becomes an appreciable fraction of the data symbol duration. The resulting ISI caused by the delay spread causes an irreducible error floor, where irreducible errors are defined by [5] as being errors that occur at very high receive signal to noise ratio. The relationship between BER and rms delay spread is further addressed in [2] [31-35]. An evaluation of the

rms delay spread (at the venue selected for fading measurements in the presence of people in motion about the receive antenna) is included as Appendix F in this thesis to identify its value for completeness of BER evaluation in a fading channel. The area of delay spread has been adequately researched in other references, and is therefore not covered in detail within the main body of the this research.

2.5 Noise

For the detection of signals in additive noise in most applications of statistical decision theory Gaussian noise is often assumed since other distributional assumptions usually lead to mathematical difficulties. However in many practical instances the measured probability density function (pdf) of the additive disturbance exhibit much heavier tails than the Gaussian distribution. Noise of short time duration fits this category and is often categorised as impulsive. Although an impulse does not exist physically as it must have zero width, there are mathematical functions that have all the properties of an impulse as the pulse width tends to zero, one being the sinc function. The amplitude envelope can be represented by a sinc function in the frequency domain, and as such the amplitude level of harmonics related to impulsive noise quickly reduces at higher frequency values. Impulsive noise spikes of relatively short time duration are often caused by short duration bursts of electromagnetic radiation emanating from such sources as lightning discharges, power line insulator surface arcing, motor vehicle ignition systems contacts, relay contacts making and breaking electric current flow to circuits, and many others. Due to their impulsive nature the harmonics produced are therefore of greater intensity at lower frequencies in the radio bands employed for communications. However, as the sinc function theoretically extends infinitely, then some noise of an impulsive nature is generally present in all bands, be it at extremely low levels at higher frequencies. The amplitude level, duration, and repetition rate of the impulsive noise affects the BER performance over the channel. Noise both of an impulsive nature and of other non-impulsive forms is ever present in all radio frequency bands (even galactic noise from the "Big Bang" can be measured if the measurement system has sufficient sensitivity). By allowing for receiver sensitivity and performance and designing the indoor radio system to operate with a minimum receive carrier wave power level that is significantly higher

than any identified impulsive noise or other noise level received then the impact of the noise on BER performance is negligible. To this objective an acceptable level for measurement system sensitivity that is related to the measurement band of interest, its proposed uses, and receiver sensitivity has been selected by researchers seeking to identify noise in the band and its statistical nature. The selection of measurement system sensitivity therefore precludes the identification of all sources of noise below this threshold.

Noise in the 2.3-2.5 GHz band of interest has been identified by measurement by several researchers. Impulsive noise being of short time duration and generally low in level was identified by reference [78] as being radiated from three sources:

1. A photocopier.

2. An elevator switch.

3. A microwave oven.

Impulsive noise can appear across a wide frequency band as the time width of the pulse tends to zero, and the measurement results in [78] show impulsive noise from the photocopier and elevator switch at frequencies around 918 MHz, 2.44 GHz, and 4.0 GHz. The microwave oven noise was only detected around 2.44 GHz and not at 918 MHz or 4.0 GHz. The distances from the noise sources respectively were 6.1 metres for the photocopier, 2.4 metres for the elevator switch, and 8.2 metres for the microwave oven. Typical peak amplitude probability distributions for impulsive noise are plotted from measurement data analysis in [78], and show an approximate 0.1 % probability that for the 2.44 GHz and 4.0 GHz bands the amplitude of the impulsive noise exceeds the thermal noise ($P_{min} = k\,T_0\,B$) value by typically 32 dB. For the 918 MHz lower frequency band impulsive noise exceeded the ($P_{min} = k\,T_0\,B$) value by typically 50 dB at the 0.1 % probability value. Reference [78] also notes that "impulsive noise produced by the microwave oven, at a distance of 8.2 metres from the receiver at site E, exceeded $k\,T_0\,B$ by 77 dB". Noise produced by an operating microwave oven (measured in the time domain) for the 2.44 GHz band is depicted in [78]. At 15 metres from the oven with a dry wall partition between oven and receive antenna the peak received power level at the antenna was typically –55 dBm.

Reference [75] analyses the emissions from operational microwave ovens and concludes that ovens emit "broadband noise that might interfere with digital mobile communications systems operated at frequencies within 1 to 3 GHz bands". Low level noise was also identified at 1.9 GHz when the microwave oven was operational. The level of this 1.9 GHz noise being approximately 60 dB below the peak noise values measured at the 2.47 GHz frequency. The 1.9 GHz noise is said to be related to the fast switching (≅ 30 kHz) of the power supply for ovens with switch mode supplies. The 1.9 GHz noise is not in the frequency band being evaluated within this thesis. The noise levels expressed as effective radiated power (ERP) with the microwave oven acting as an antenna, were for the 2.4 to 2.47 GHz band, estimated from measurements to be in the range 60 to 110 dBpW. Reference [75] states that the maximum emission occurs at a frequency within the 2.45 GHz band, but that ovens radiate out-of-band emission across a wide range of frequencies. Furthermore, both the frequency and the level of this emission vary with the changes in the magnetron output characteristics, load characteristics, load variation caused by the turntable rotation, and the position on the turntable of the substances being heated within the oven cavity. It also states that a clear dependency on electromagnetic polarisation was not found for the microwave oven noise radiated.

Reference [76] provides an evaluation of interference from domestic microwave ovens to 1.9 GHz digital radio transmission. BER curves are presented for a transmitted data sequence representing a pseudo-noise code at 384 kilobits/second rate. The modulation used being $\pi/4$ shift QPSK, with carrier wave frequency set to 1.90115 GHz. The receiver sensitivity was such that at a receiver input of 10.5 dBμV a BER error rate after demodulation (attributed to thermal systematic noise only) of 1×10^{-2} was measured. Two sets of BER results are presented, one set showing data for degradation to error rate when microwave ovens employing switched mode power supplies are operating, the other when ovens with conventional transformer type power supplies are operating. The electromagnetic noise from the operational ovens was electromagnetically coupled by means of a half wave dipole antenna located 1.26 metre from the operational ovens under test. The output of the antenna was then connected into the receiver front end via an attenuator and RF hybrid. The other port of the hybrid was fed with the modulated carrier wave directly coupled from the

transmitter, also via an attenuator. Three microwave ovens employing switched mode power supplies were evaluated and also three ovens with the conventional transformer power supply. Results indicated that two of the switched mode type ovens significantly increased BER while operational, and also one of the conventional transformer type, but by a lesser amount. One of the switched mode type ovens and two of the transformer type ovens had little influence on BER while operational.

2.6 Conclusions from Noise Literature Review:

Noise generated from operational microwave ovens is clearly a potential problem for radio transmission links operating in the 2.3–2.5 GHz frequency band, the band being examined within this thesis. Although some research has been completed there is little explanation as to the nature and severity the noise has on BER performance at particular carrier frequencies of operation. The noise in the 2.3–2.5 GHz frequency band has not been quantified clearly with respect to how it occurs, or how its intensity varies with time over the operational cycle of a microwave oven in proximity to a communications receiving antenna. A detailed analysis of this form of noise source and its influence on BER for received data is warranted, and this detailed analysis will be an original contribution to new research competed within this thesis.

Other forms of noise within the 2.3–2.5 GHz band have been identified by researchers [78], in particular the impulsive type. To further investigate and identify noise sources in this band a measurement campaign will be completed and the results included in this thesis. The measurement system sensitivity is selected to enable the identification of noise signals that intercept the receive antenna at a peak power level of -123.8 dBm (Appendix A). This value is 33.8 dB lower than the typical minimum receive level sensitivity of -90 dBm (7.071 μV) in 50 ohms specified by most communications systems employed in this frequency band. At the –90 dBm (7.071 μV) receive level a BER due to systematic noise floor characteristics of 1×10^{-5} is typical. The selection of a measurement system sensitivity 33.8 dB lower than the systematic noise for minimum receive level provides a significant margin to allow identification of noise power levels that affect BER performance. Noise present at lower levels than the selected measurement sensitivity has minimal affect on average BER performance.

Chapter 3

The Indoor Radio Propagation Channel

In this chapter we introduce the characteristics of an indoor radio propagation channel and associated phenomenon that need to be identified and modelled in order to predict the performance of the channel for high speed data transmission. The statistics derived from measurement of the indoor channel phenomena are identified, and their relationship to the error performance of data transmitted over the channel is analysed for digital modulation.

3.1 Models of the Indoor Radio Propagation Channel

Models of the indoor radio propagation channel can be based on analytical and empirical studies. These models can be classified as either deterministic or statistical. Deterministic models such as those based on Maxwell's equation and ray tracing techniques require detailed knowledge of the physical indoor channel environment. Knowledge of the indoor environment geometric dimensions and the type of construction materials used for walls, roof, floor, furniture, and other objects within the channel is essential for deterministic models. Statistical models are based on measurements, and as such the phenomena associated with the indoor radio propagation channel are not theoretically derived but calculated from measured empirical data. Statistical models are developed from the practical approach of choosing sites where indoor radio data transmissions are likely to be used, and modelling the physical attributes of the propagation medium associated with these

sites as processes with certain distributions generally derived from measurements. Statistical models therefore provide qualitative information about the indoor channel such as received signal fluctuations, and rates and duration of signal impairments. In this thesis a hybrid mix of both the deterministic approach to modelling the indoor radio propagation channel and statistical modelling of measurement data are used to characterise the indoor radio channels performance for data transmission.

3.1.1 Noise

The receiving system of the indoor propagation channel has a receive antenna which is being illuminated by electromagnetic radiation from various sources. Radiations intercepting the receive antenna which are not part of the wanted transmitted signal can result in noise and interference. The amount of unwanted additive channel noise entering the receiver via the receiving antenna is dependent on frequency range, receive antenna gain, and bandwidth. The identification and characterisation of additive channel noise generated from noise sources in the 2.3-2.5 GHz frequency range form an essential part of our measurement data gathered.

3.1.1.1 Noise Sources

When considering the indoor radio channel as a medium for high speed data transmission, the sources of noise that specifically affect the bit error rate performance of data transmitted over the channel must be identified and quantified. These noise sources are broadly divided into two groups as follows:

(1) Transmission System Noise - This is defined as noise generated from within the data transmission or measurement system itself. This type of noise is an inherent part of all transmission systems and includes thermal and shot noise generated within the system hardware.

(2) Propagation Noise - This is noise introduced to the data transmission or measurement system via the receive antenna which is not transmission system noise. The receiving antenna collects noise emissions from galactic, solar, and

terrestrial sources. Terrestrial sources include the sub-category termed man-made noise generated from the operation of equipment such as microwave ovens, car ignition systems, electric trains, and other equipment that emits electromagnetic radiation during operation.

3.1.1.2 Additive Channel Noise and BER for Digital Modulation

In most digital radio systems modulation is achieved by modifying the transmitted radio carrier waves amplitude and/or phase as a function of the digital data information stream being transmitted. The received signals amplitude and phase can then be represented as a discrete point in a two dimensional plane termed the I-Q plane where I represents in-phase and Q represents quadrature which is 90^0 out of phase. By forcing the carrier to any of several predetermined positions in the I-Q plane, each of which represents a mapping for one or more bits of data, a data stream can be transmitted and consequently decoded at the receiver. The mapping of states at the receiver at each symbol timing instant onto the I-Q plane produces what is referred to as a constellation diagram. In theory the constellation should be single points for any sequential data transmission, but in practical systems a dispersal or spread of the dots around each state occurs. This spreading is the result of transmission system impairments and noise.

For digital modulation using coherent phase shift keying, noise is added to the modulated signal x(t) as it passes through the channel. This noise is sourced by the transmission system itself, or propagation derived as defined in Section 3.1.1.1. In modelling the channel, the transmit filter, transmission channel, and receive filter are linear and time invariant. Therefore the complex signal envelope, y(t), at the output of the receive filter may be written as [32]:

$$y(t) = x(t) * h(t) \tag{3.1}$$

with $$h(t) = h_T(t) * h_C(t) * h_R(t) \tag{3.2}$$

where $h_T(t)$, $h_C(t)$, and $h_R(t)$ are the impulse responses of the transmit filter, the channel, and the receive filter respectively, and the symbol * denotes convolution. For the constellation diagram considering the I-Q plane, $n_i(t)$ and $n_q(t)$ are the in phase and quadrature components of the additive noise at the receive filter output. For symmetrical filters, $n_i(t)$ and $n_q(t)$ are independently and identically distributed Gaussian random variables with zero means. For constant noise amplitude and random phase, the loci of the noise power distribution function is a circle of radius n_0 centred on the tip of the ideal reference vector of Figure 1, where

$$n_0 = \sqrt{n_i^2 + n_q^2} \tag{3.3}$$

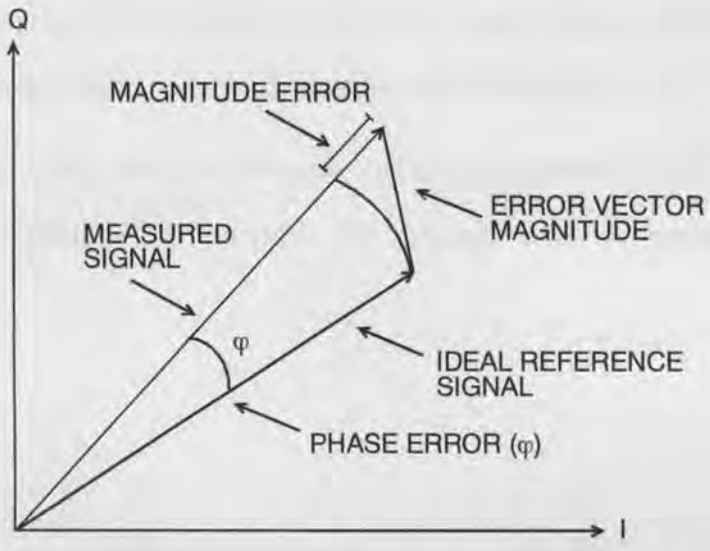

Figure 1: Error Vector Values.

The EVM shown in Figure 1 is directly proportional to additive channel noise. In the absence of any other signal corruption the EVM is an indicator of the magnitude of total additive channel noise n_0. The loci of n_0 can be statistically modelled with the measurement system connected back to back to allow quantification of transmission system noise, and then with the propagation path inserted. For additive white Guassian noise (AWGN) the subtraction of transmission system noise from the noise measured with the propagation path included results in a statistical remainder representing the channel propagation noise. The upper bound for the probability of symbol error in an AWGN channel which has a noise spectral density equal to n_0 can be obtained for any arbitrary constellation using the union bound. The union bound

[40] provides a representative estimate of the average probability of error for a particular modulation signal, $p_S(\varepsilon/S_i)$:

$$p_S(\varepsilon/s_i) \leq \sum_{j=1} Q\left(\frac{d_{ij}}{\sqrt{2n_0}}\right) \quad (j \neq i) \tag{3.4}$$

where d_{ij} is the Euclidean distance between the i and j signal points within the constellation, and Q(x) is the Q-function. When the constellation is symmetric the distance between all points is equal and $p_S(\varepsilon/S_i)$ is the same for all i. Equation (3.4) therefore provides the average symbol error probability for symmetric constellations. For binary phase shift keyed (BPSK) modulation, equal energy antipodal signalling is used. For antipodal signal vectors S_1 and S_2, with amplitudes $\pm\sqrt{E_b}$, as shown in Figure 2, the Euclidean distance between constellation points is $2\sqrt{E_b}$. Substitution of this into Equation (3.4) provides the average error probability for BPSK modulation as:

$$P_{e,BPSK} = Q\sqrt{\frac{2E_b}{n_0}} \tag{3.5}$$

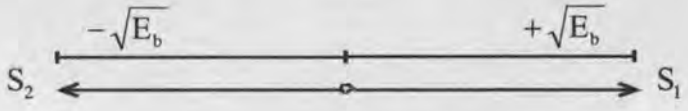

Figure 2: BPSK Modulation.

The average error probability is therefore directly related to the EVM, and in Chapter 4 we detail the measurement system and technique used to accurately quantify EVM.

3.1.2 Impulse Response

Radio waves propagating within buildings between transmit and receive antennas travel via many paths other than the direct or line of sight (LOS) path if it exists. The waves encounter surfaces such as walls, floor, ceiling and other objects such as

furniture and people. At these surfaces the amount of energy reflected from and transmitted through the material is a function of the materials physical constants (i.e. conductivity σ, permittivity ε, and permeability μ), as well as frequency and the angle of incidence between the direction of wave propagation and the material surface. This multipath nature of the indoor channel can be fully described by its time and space varying impulse response [41].

For the indoor radio channel, radio waves can be modelled as discrete paths resulting in a multipath model. The impulse response $h(\tau,r)$ of such a channel at range r between transmit and receive antennas is modelled as [7]:

$$h(\tau, r) = \sum_{i=0}^{n} E_i(r) e^{-j2\pi f_c \tau_i} R_i \delta(t - \tau_i) \qquad (3.6)$$

where:

τ_i - propagation delay of i^{th} path,

E_i - received electric field intensity of i^{th} path,

R_i - reflection coefficient of i^{th} path,

f_c - radio wave carrier frequency,

$\delta(t)$ - dirac delta function,

and the shortest path (generally LOS) between transmit and receive antennas is for $i = 0$.

The computation of the impulse response for any particular range requires a known value for E_i and R_i, the electric field intensity and reflection coefficient, respectively, for the i^{th} multipath radio signal. For each path i, R_i may be representative of one or more reflections from one or more different surfaces, thus forming a final composite value for the reflection coefficient over the total path. Also, the total propagation delay of the i^{th} multipath ray is directly related to the distance the signal travels, and this may similarly involve one or more reflections before it intercepts the receive antenna.

In order to calculate E_i and R_i, the relationship between transmitted radio power P_T and electric field intensity E_T needs to be known, as well as the physical constants and

incident angle of the radio wave for R_i computation at the point or points of reflection. The following provides the background theory necessary for calculation of E_i and R_i for substitution into the indoor radio channel's impulse response Equation (3.6).

The electromagnetic radio wave has a wave front that is approximately planar at distances greater than the Far-Field distance [42] associated with the radiating antenna. Polarisation of electromagnetic plane waves is by adopted standard described by time variations of the electric field.

For a plane wave travelling in the +Z direction, the electric field intensity variation in time and space is described by:

$$\vec{E}(t,z) = \hat{x}E_0\cos(\omega t - \beta z) \qquad [V/m] \tag{3.7}$$

The associated magnetic field intensity is given by:

$$\vec{H}(t,z) = \hat{y}\frac{E_0}{\eta}\cos(\omega t - \beta z) \qquad [A/m] \tag{3.8}$$

where:

$\omega = 2\pi f$ - angular frequency [rad/s],

f - frequency [Hz],

β - phase constant [rad/m],

λ - wavelength [m],

$\eta = \sqrt{\frac{\mu}{\varepsilon}}$ - intrinsic impedance of the medium [ohms],

$\varepsilon = \varepsilon_0\varepsilon_r$ - medium permittivity [F/m],

$\mu = \mu_0\mu_r$ - medium permeability [H/m].

Equation (3.8) for $\vec{H}(t,z)$ the magnetic field mirrors that for $\vec{E}(t,z)$ in Equation (3.7) the electric field with the exception that it is in the y direction and scaled by the value of the intrinsic impedance η.

Therefore, it can be expressed by:

$$H_y(t,z) = \frac{E_x(t,z)}{\eta} \tag{3.9}$$

or generalised as co-ordinate independent in the following form:

$$H(t,z) = \frac{1}{\eta}\vec{n} \times E(t,z) \tag{3.10}$$

where $\vec{n}$ is the unit vector in the radio waves propagation direction.

For the free space, the intrinsic impedance η_o is given by:

$$\eta_o = \sqrt{\frac{\mu_o}{\varepsilon_o}} = \sqrt{\frac{4\pi \times 10^{-7}}{10^{-9}/36\pi}} = 120\pi \approx 377 \text{ohms} \tag{3.11}$$

From Poynting's theorem the vector cross product of $\vec{E}$ and $\vec{H}$ at any point is a measure of the rate of energy flow per unit area at that point, or power $\vec{P}(t,z)$, expressed as:

$$\vec{P}(t,z) = \vec{E}(t,z) \times \vec{H}(t,z) \quad [W/m^2] \tag{3.12}$$

Substituting (3.7) and (3.8) for $\vec{E}(t,z)$ and $\vec{H}(t,z)$, respectively, yields

$$P(t,z) = \hat{z}\frac{E_o^2}{\eta}\cos^2(\omega t - \beta z) \quad [W/m^2] \tag{3.13}$$

The time average power density is given by the integral of $\vec{P}(t,z)$ divided by the period $T = \frac{1}{f}$, thus:

$$P_{AV} = f\int_0^{1/f} \frac{E_o^2}{\eta}\cos^2(\omega t - \beta z)dt$$

$$P_{AV} = \frac{1}{2}\frac{E_o^2}{\eta} \tag{3.14}$$

If the rms values instead of peak amplitudes are used, the factor of ½ is not present.

Hence, the rms power flow through any area S normal to the Z axis is expressed as:

$$P_{rms} = \frac{E_0^2}{\eta} S \quad [W] \tag{3.15}$$

The transmitted electric field intensity is therefore directly proportional to the square root of the transmitted rms power flow through any area S normal to the Z axis, that is:

$$E_T = K_1 \sqrt{P_T} \tag{3.16}$$

where K_1 is a constant, P_T is the transmitted power and:

$$K_1 = \sqrt{\frac{\eta}{S}}$$

with S being the area normal to the Z axis. Similarly, the received electric field intensity is also directly proportional to the square root of the received power, therefore:

$$E_R = K_1 \sqrt{P_R} \tag{3.17}$$

In the ideal case of free space transmission from an isotropic transmit antenna, the received power at range (r) is given by [2] as:

$$P_R = \frac{P_T}{4\pi r^2} \tag{3.18}$$

where:

P_T, P_R - transmit and receive power levels,

r - range or distance between transmit and receive antennas.

From Equations (3.17) and (3.18), the received electric field intensity as a function of transmitted power and range is related by:

$$E_R = \frac{K_1 \sqrt{P_T}}{2\sqrt{\pi}\, r} \tag{3.19}$$

Therefore, the received electric field intensity E_i for the i^{th} signal path for an isotropic antenna as a function of range is expressed as:

$$E_i(r) = \frac{K_1 \sqrt{P_T}}{2\sqrt{\pi}\,(r + \Delta\tau_i c)} \tag{3.20}$$

where $\Delta\tau_i$ is the delay for the discrete paths i = 1.....n with respect to the direct or the shortest path length i = 0, which has a time delay equal to r/c seconds, and c is the speed of light. Equation (3.20) can be used to calculate $E_i(r)$ for substitution into the impulse response Equation (3.6).

The reflection coefficient for dielectric walls, floor, and roof is real at high frequencies [43]. For real R_i, where the E field of the wall incident radio wave is perpendicular to the plane of incidence (the plane of incidence being defined as the plane containing the incident ray and the normal to the surface) the reflection coefficient [43] is given by:

$$R_{walls} = \frac{\cos\theta_{inc} - \sqrt{(\varepsilon_2/\varepsilon_1) - \sin^2\theta_{inc}}}{\cos\theta_{inc} + \sqrt{(\varepsilon_2/\varepsilon_1) - \sin^2\theta_{inc}}} \tag{3.21}$$

and for floor and ceiling with the same E field polarisation [43] is given by:

$$R_{floor/ceiling} = \frac{(\varepsilon_2/\varepsilon_1)\cos\theta_{inc} - \sqrt{(\varepsilon_2/\varepsilon_1) - \sin^2\theta_{inc}}}{(\varepsilon_2/\varepsilon_1)\cos\theta_{inc} + \sqrt{(\varepsilon_2/\varepsilon_1) - \sin^2\theta_{inc}}} \tag{3.22}$$

where:

R - reflection coefficient,

θ_{inc} - angle between the incident radio wave and the normal to the surface,

ε_1 - permittivity constant of the first medium which is generally air,

ε_2 - permittivity constant of the second medium which is generally walls, ceiling, or floor.

Dependent on which discrete path i is being computed, and on the polarisation of the E field (either perpendicular or parallel to the plane of incidence), either Equation (3.21) or Equation (3.22) can be used to calculate R_i for substitution into the impulse response Equation (3.6).

The impulse response $h(\tau, t)$ for the indoor radio channel gives a measure of the severity of multipath propagation within the channel. The total time in which the channel impulse response is not equivalent to zero and the relative power distribution over this time has resulted in a numeric parameter termed the rms delay spread σ_τ being defined as the power weighted rms width of the channel average impulse response [44]. This frequently measured parameter has been also linked with the channel BER performance [5]. The rms delay spread σ_τ is calculated from Equation (3.23) as follows:

$$\sigma_\tau = \left\{ \left[\sum_{i=0}^{n} (t_i - \tau_m - t_0)^2 E_i^2 \right] / \sum_{i=0}^{n} E_i^2 \right\}^{\frac{1}{2}} \tag{3.23}$$

where t_0 is the arrival time of the first path (generally the LOS in a profile), and τ_m is the mean excess delay calculated from Equation (3.24):

$$\tau_m = \left[\sum_{i=0}^{n} (t_i - t_0) E_i^2 \right] / \left[\sum_{i=0}^{n} E_i^2 \right] \tag{3.24}$$

The error rates for data transmission over a channel with delay spread are dependent on the normalised value of σ_τ [44]. Normalised σ_τ is defined as:

$$d = \frac{\sigma_\tau}{T} \tag{3.25}$$

where T is the transmitted data symbol period.

3.1.2.1 Impulse Response and BER for Digital Modulation

At gigahertz frequencies the wavelength of the radio frequency signal is relatively small and the phase of the received signal can change significantly when motion is introduced into the channel. This motion can be caused by people moving about the indoor environment, the movement of the transmit or receive antenna, or inanimate objects such as machinery. The result of this motion is a change to one or more of the discrete paths τ_i of the multipath Equation (3.6). Digital transmission over a wideband indoor channel suffers intersymbol interference (ISI) caused by the time delay spread of these discrete paths τ_i which results in frequency selective fading. If the rms delay spread σ_τ, computed in Equation (3.23), becomes an appreciable fraction of the symbol period then ISI results in the generation of an irreducible error floor [35]. As a general rule for values of rms delay spread less than 0.1 the system can be considered as narrowband, and for values above 0.1 wideband characteristics begin to influence error performance.

The normalisation of σ_τ to symbol period T as shown in Equation (3.25) results in the dimensionless parameter d. A relationship between d and the average irreducible BER has been calculated for unfiltered digital modulation using computer simulation methods [5]. Figure 3 (from [5]) depicts the relationship between d and the average irreducible BER for a multipath channel simulation using a Gaussian delay profile. The resultant performance ranking of the unfiltered modulation for d normalised to the same symbol period is shown in Figure 3 as BPSK, QPSK, OQPSK and MSK.

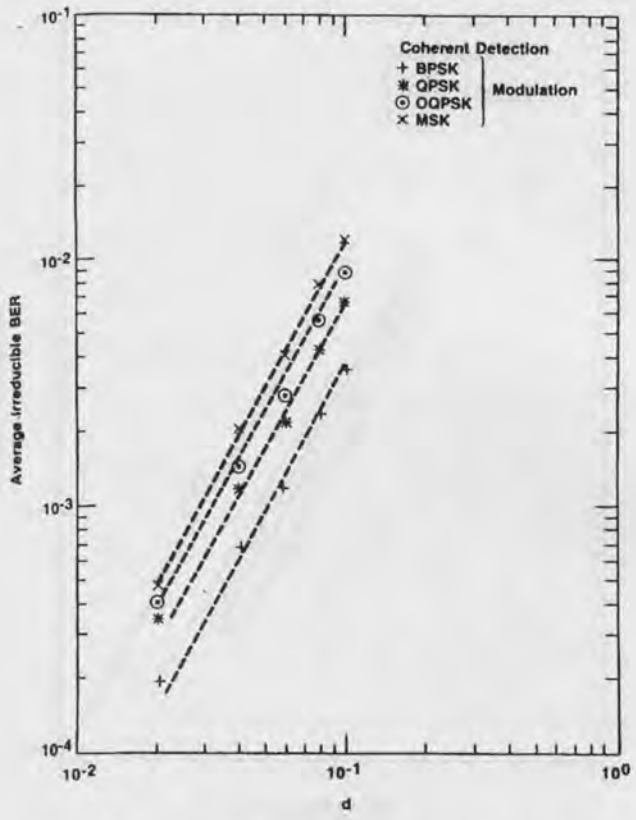

Figure 3: The Influence of d on BER for Unfiltered Modulation.

A fairer comparison of modulation performance in the presence of delay spread is given by Figure 4 (from [5]), where d' is defined as follows:

$$d' = \frac{\sigma_\tau}{T_b} \tag{3.26}$$

with σ_τ normalised to bit period T_b.

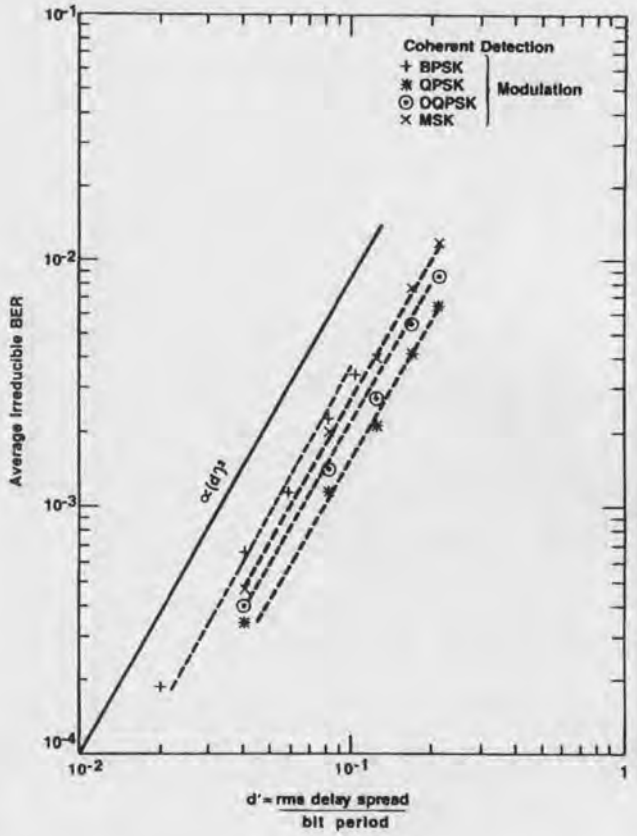

Figure 4: The Influence of d' on BER for Unfiltered Modulation.

The application of bit period instead of symbol period normalisation shows that MSK and "4-level modulation (QPSK, OQPSK) are more resistant to delay spread than BPSK modulation for constant information throughput" [5].

Simulations for higher level modulation such as 8-PSK (which has 3 bits/symbol) were performed at signal to noise ratio (SNR) approaching infinity, and the results indicated that its performance was not superior to that of QPSK.

The results of the 8-PSK simulation (from [5]) are given in Figure 5.

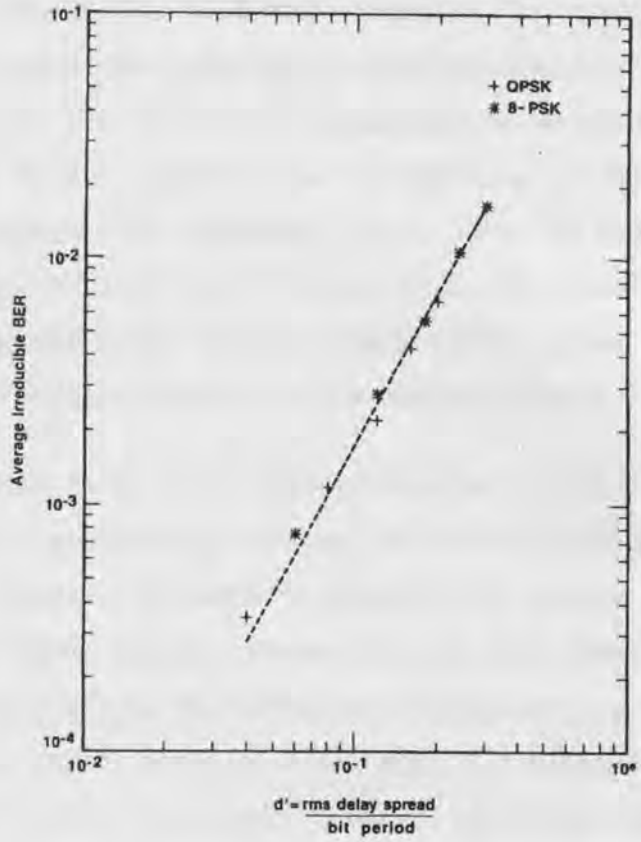

Figure 5: The Influence of d' on 8-PSK for Unfiltered Modulation.

3.2 Summary

In this chapter we have identified additive channel noise, channel fading, and channel impulse response as three phenomena that each exhibit a major influence on the BER performance of the indoor radio propagation channel. To allow us to identify total additive channel noise by measurements, and then statistically characterise the measured noise, the noise can be separated into the two specific groups of transmission system noise and propagation noise. The separation of the total additive channel noise into two groups allows us to identify and determine the impact of propagation noise introduced to our indoor radio data transmission system via the receiving antenna, which by definition is not transmission system noise that is generated from within the system itself. To obtain the noise measurement data necessary for the development of BER models of the indoor radio propagation channel we have introduced the concept of error vector values and EVM. EVM is a

measurement parameter that is directly related to the received average BER probability of data transmitted using digital modulation methods over the indoor radio propagation channel. The use of EVM measurement techniques to characterise the sources of total additive channel noise by separating it into its two distinct contributive components of transmission system noise and propagation noise is described in Section 3.1.1.1, and Section 3.1.1.2. The described methodology provides the foundation on which a measurement system capable of the characterisation of additive channel noise is developed in Chapter 4.

The multipath nature of the indoor radio propagation channel is also discussed in Section 3.1.2, and a mathematical multipath model is described where the impulse response of the channel is described by Equation (3.6). A single important statistic derived from the channel impulse response is the rms delay spread that has the units of time. The normalisation of the channel rms delay spread to the time duration of a data transmission symbol period T, or bit period T_b, defines two dimensionless statistics termed d and d' respectively. Computer simulation methods are used to predict the effect d and d' have on average BER and examples of the results of simulations taken from [5] are shown in Figures 3, 4, and 5. All curves depicted in these figures show an increasing probability of the average irreducible BER as either d or d' increases in absolute magnitude. An estimate of the impulse response of an indoor radio propagation channel can be obtained from a measurement system capable of gathering empirical measurement data for specific placements of transmit and receive antennae within the channel. From the data obtained from measurements statistical values for d and d' can be computed, and these values can then be used to estimate average irreducible BER from the computer simulation curves such as those presented in Figure 3, Figure 4, and Figure 5. The methodology applied to gather this data is described in Appendix F.

Chapter 4

Characterisation of Additive Channel Noise

In Section 3.1.1.1 the noise sources that influence the BER performance for high speed data transmission over the indoor radio channel were divided into two groups, namely transmission system noise and propagation noise. Transmission system noise is generated within the transmission or measurement system itself and is related to the thermal agitation of electrons in amplifiers and other components. For any system the noise spectral density at a specified temperature is determined by the level of noise generated from the system hardware. The average level of this noise remains constant for any particular temperature and can be termed "systematic noise". In order to quantify the systematic noise present in our measurement system used to transmit high speed data over the indoor radio propagation channel, a series of back-to-back calibration tests were performed both before and after the completion of any data gathering measurement. Although our data transmission system is capable of the measurement of non-systematic propagation noise (Section 3.1.1.1), its lack of portability necessitated the use of a separate noise measurement system. The two systems are described in sections 4.1 and 4.2.

4.1 Systematic Noise Measurements and the Data Transmission System

Figure 6 depicts the measurement instrumentation used for high speed data transmission and fading measurements over the indoor radio channel. The measurement and analysis of fading is separately addressed in Chapter 6, however the additional instrumentation necessary to gather our fading data also contributes in part to the overall systematic noise and as such must be included in system noise calibration measurements. All measurement equipment was accommodated on a movable steel trolley as shown in Figure 7.

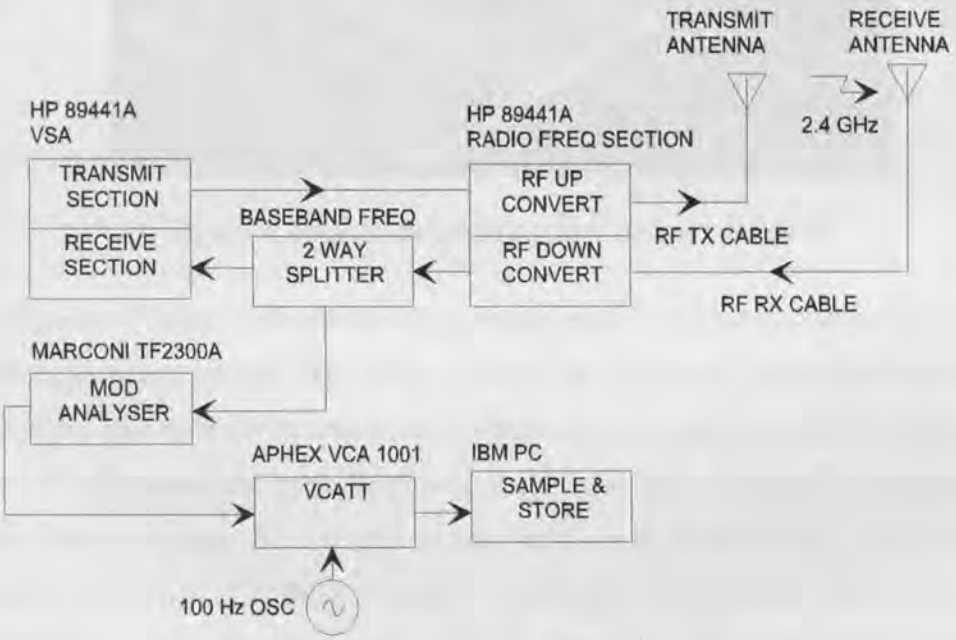

Figure 6: Measurement instrumentation.

Figure 7: Measurement Equipment Accommodation.

The Hewlett Packard HP89441A vector signal analyser (VSA) is the primary part of the measurement system. The VSA provides the necessary continuous wave (CW) transmitter and receiver functions for calibration of the measurement system and the series of measurements performed over the indoor radio propagation channel. The carrier frequency can be selected in the range from 0-2.65 GHz. The modulation analyser Marconi TF2300A, voltage controlled attenuator (VCATT) Aphex VCA1001, and the IBM PC with a sampler card record fading data for the indoor channel. Envelope detection of the baseband signal by the modulation analyser results in a control voltage that amplitude modulates a 100 Hz sinusoidal carrier. The amplitude modulation is achieved by the direct application of a dc control voltage output from the modulation analyser to the input of the VCATT. This amplitude modulated 100 Hz carrier replicates the temporal variations (fading) of the 2.4 GHz CW between the transmit and receive antenna. It is then over-sampled at 11.025 kHz rate and stored on the PC hard disk for subsequent analysis.

The VSA is used to transmit, receive, display, and store data gathered for statistical modelling of the indoor radio propagation channel. The VSA can transmit and receive

random data sequences over a propagation channel using a variety of modulation formats and filtering options. These options include BPSK, QPSK, and 8-PSK modulation; and raised cosine (Nyquist), square root raised cosine, Gaussian, rectangular, low pass, or user selectable filtering. Data symbol rates up to 4 megasymbols/second can be analysed by the VSA. Because the transmit section and receive section of the VSA are co-located, the need for carrier recovery from the transmitted signal is eliminated. This ensures a non-noisy phase estimate which is free from carrier fluctuations, and full coherent reception. The use of the spectrum analysis mode option of the VSA allows the received power spectrum of both noise and other signals including the frequency selective fading characteristics of wideband transmissions, to be viewed and stored to disk for further analysis.

Three antenna models form part of the measurement instrumentation selected to gather the empirical data, and the technical specifications for these antennae are given in Appendix B. The antennas are mounted on non-metallic height adjustable stands, providing antenna height settings from 1-2.5 metres as depicted in Figure 7. For all measurements vertical polarisation is used for the antennas as it is the most common polarisation used by mobile portable communications systems that operate over indoor radio propagation channels.

4.1.1 Quantification of Systematic Noise and Error Vector Magnitude for the Data Transmission System

In order to quantify systematic noise and the associated EVM within the data transmission system (Figure 6), a series of back-to-back measurements are performed. The antennas shown in Figure 7 are removed and the two antenna feeder cables directly connected together. Then the cyclic transmission of a random data sequence of length 600 symbols at the 4 megasymbol/second rate for a range of receiver average modulation power levels allow us to determine the value of both systematic noise and the EVM. This calibration procedure is completed for both BPSK and QPSK modulation, with raised cosine filtering that has a roll-off factor of 0.5.

Figure 8 (top) typifies the measured statistics available pertaining to our system, and is for BPSK modulation in this case. The available data includes the received eye diagram (top right quadrant), an ideal reference constellation (top left quadrant), the measured constellation (bottom left quadrant), and EVM with its associated values (bottom right quadrant). Also shown in the bottom right quadrant is the first 80 symbols transmitted in our cyclic sequence, with the first symbol (symbol number 0 which is shown highlighted) being a 0 bit. This particular symbol is also the symbol centred on the diamond marker of the measured constellation. Figure 8 also depicts the associated received power spectrum for the transmitted BPSK sequence, and from measurement of its average modulated power we can produce the necessary system calibration curve that identifies the effect of hardware generated noise on EVM. Also, as part of our calibration process, the radio frequency CW is turned off and a noise spectrum that occupies the same spectral bandwidth as that of the BPSK or QPSK modulation is recorded. This value of averaged noise power is the systematic noise which can be normalised to a 1 Hz bandwidth. The additional noise introduced by the inclusion of the propagation path is the non-systematic noise. The statistical subtraction of the systematic noise from the overall measured noise, when the propagation path is included, provides a statistical remainder that is the non-systematic noise. The application of this measurement methodology allows us to separate and quantify the noise introduced into the data transmission system by external sources of electromagnetic radiation. These external sources are identified in the first instance by a separate noise measurement system, which is discussed in Section 4.2.

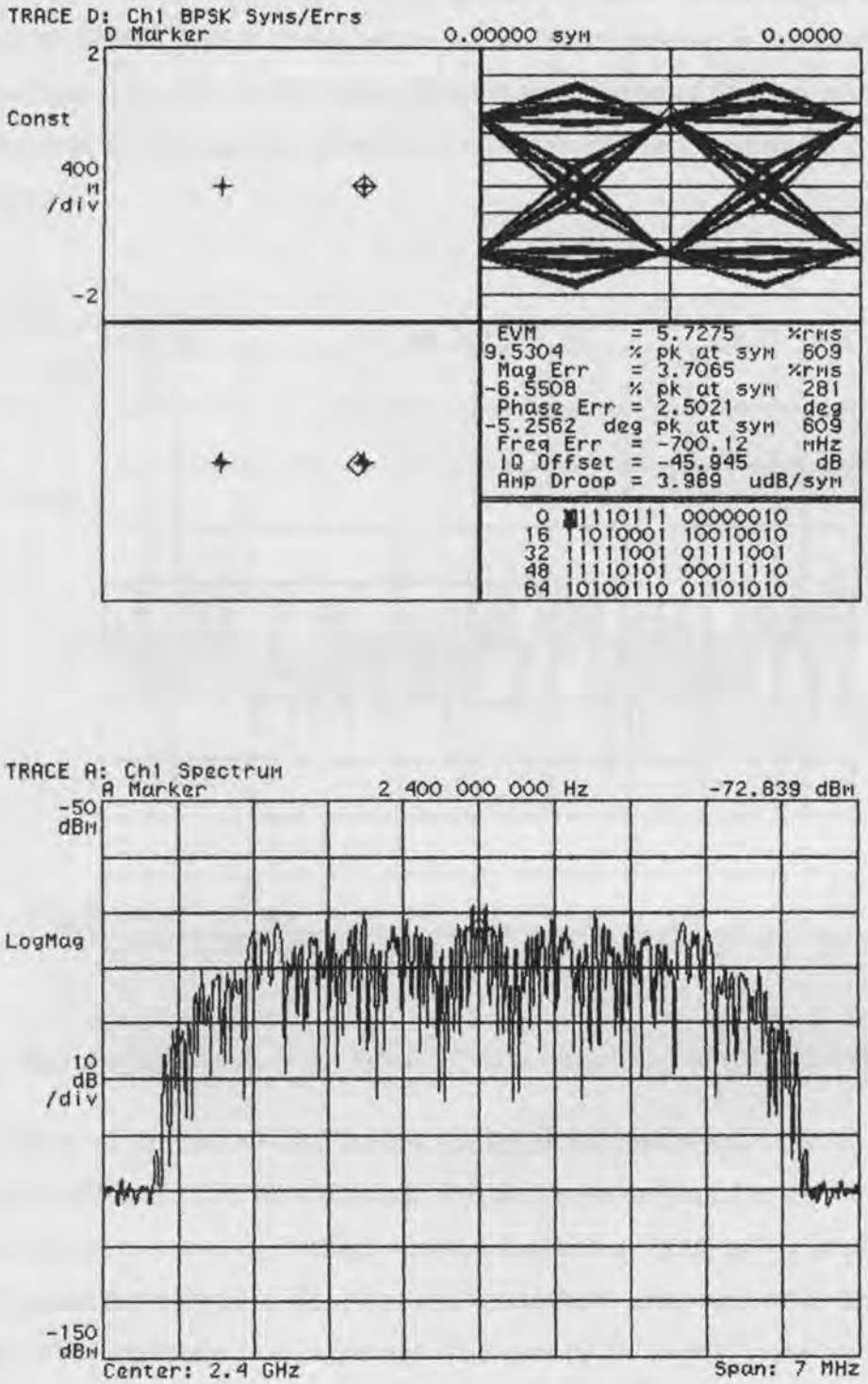

Figure 8: BPSK Data Rate 4 Megasymbols/second (Raised Cosine Filtering $\alpha = 0.5$).

An example of the measurement of systematic noise for a 7 MHz bandwidth is given in Figure 9. This noise spectrum represents a statistical average taken over

100 samples, and as can be seen in the bottom left corner of this figure an average power of -96.003 dBm is computed for the 7 MHz measurement bandwidth centred on 2.4 GHz. The -119.15 dBm value shown at the top right of Figure 9 is the average noise power for 100 samples at the centre of the measurement bandwidth, 2.4 GHz for this example.

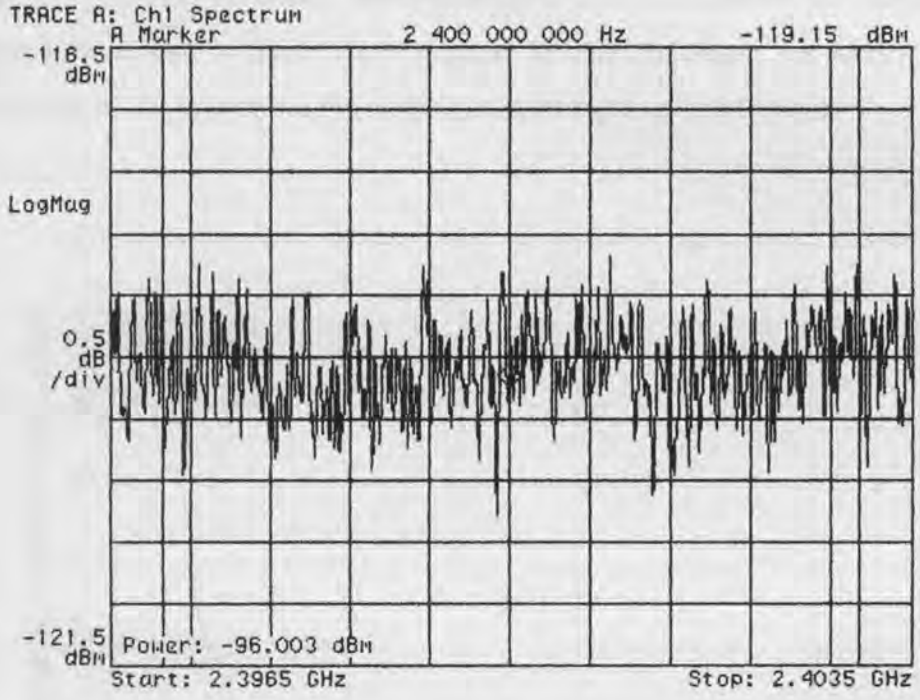

Figure 9: Systematic Noise Power (7 MHz bandwidth centred on 2.4 GHz).

The results of our back-to-back system measurements enable two curves to be plotted for both BPSK and QPSK modulation. The curves are presented as Figure 10, where the ordinate represents the average received modulating signal power in dBm for the 50 ohm real input impedance of the receiver, and the abscissa represents the rms value of the EVM expressed as a percentage. In Figure 10 the "solid" curve for BPSK and the "x-marks" for QPSK modulation have little variance, and represent the calibration datum for the systematic noise and the associated EVM attributed to the measurement system. The calibration datum provides a known system noise level base to permit the identification of non-systematic noise sources that enter the system via the receive antenna. If the received non-systematic noise is of sufficient power then an overall increase in EVM value above that caused by the inherent systematic noise level for a

specific value of received average modulating signal power (dBm) occurs. The use of this calibration datum is important as it allows the detection of noise that may be not detected by other noise measurement techniques due to its low level and random nature. EVM measurement methods allow the detection of subtle increases in noise levels to be identified because of the use of constellation diagrams with known statistics that form the base statistics before the deliberate introduction of the potential noise sources under evaluation into the shielded anechoic chamber or stable test room. Measurement data analysis lends support to this technique for identifying noise introduced to the system via the receive antenna from external origin.

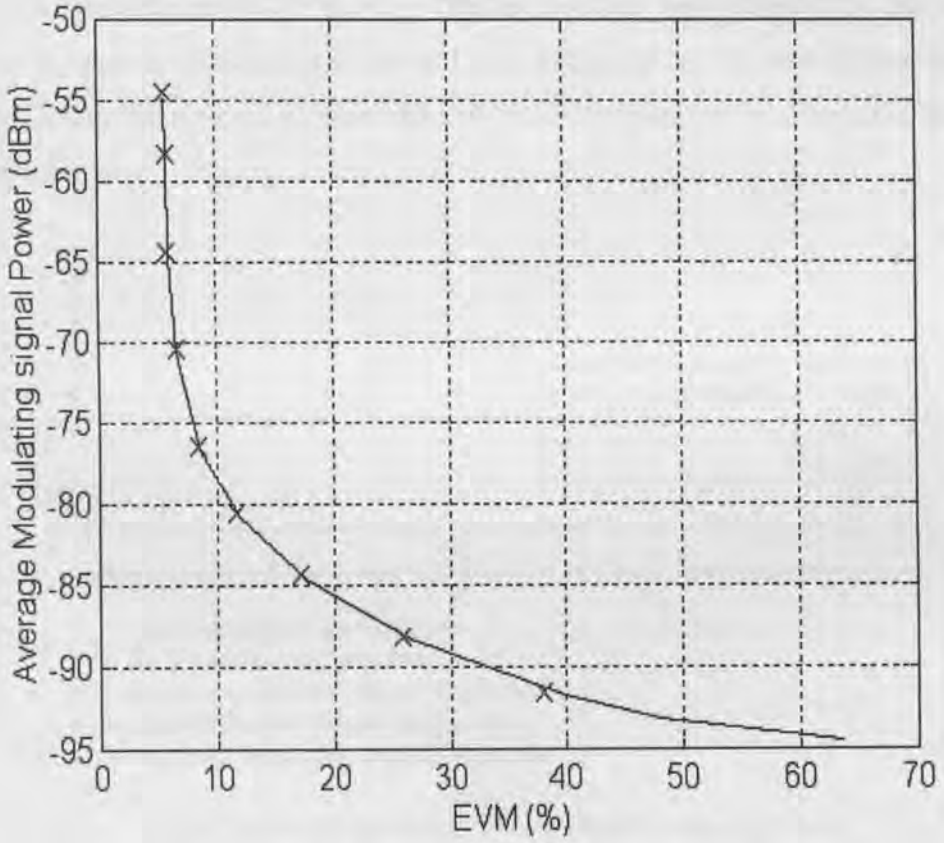

Figure 10: EVM and Average Modulating Signal Power (Solid : BPSK, × : QPSK) Symbol rate 4 Megasymbols/Second (Raised Cosine Filtering $\alpha = 0.5$).

4.2 Non-Systematic Noise Measurements

Although the measurement instrumentation as shown in Figure 6 can acquire the necessary empirical data relevant to non-systematic (propagation) noise, it is not portable enough for use at many of the measurement venues investigated for possible noise sources. A portable spectrum analyser model HP8596E, RF feeder cable, and a selection of one of the three antennas mounted on one of the non-metallic stands, shown in Figure 7, is best suited for propagation noise measurements. This system is shown in Figure 11. The measured available noise power spectral density can be expressed as an effective noise temperature, and noise figure (NF) is defined for a reference temperature of 290 K [45]. This method has been adopted by the IEEE as part of its standard definition of noise figure [46], and the characterisation of noise sources using the concept of their effective noise temperature is adopted in our noise measurements.

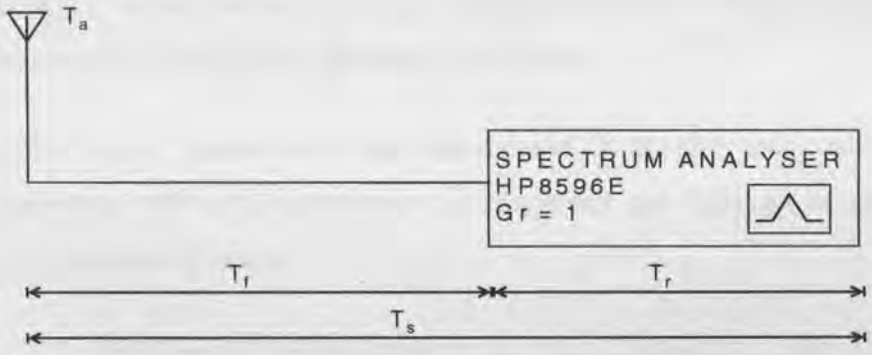

T_a = Antenna Noise Temperature
T_f = RF feeder Noise Temperature
T_r = Spectrum Analyser Noise Temperature
T_s = Overall System Noise Temperature
G_r = Receiver Gain of Spectrum Analyser

Figure 11: Non-Systematic Noise Measurement System.

A measurement system sensitivity of -123.8 dBm is calculated in Appendix A for the non-systematic noise measurement system fitted with a corner reflector antenna of 15 dBi gain. This sensitivity is adequate for identifying noise sources that can significantly influence the BER performance of data transmissions over the indoor radio channel using digital modulation [38].

4.2 Non-Systematic Noise Measurements

Although the measurement instrumentation as shown in Figure 6 can acquire the necessary empirical data relevant to non-systematic (propagation) noise, it is not portable enough for use at many of the measurement venues investigated for possible noise sources. A portable spectrum analyser model HP8596E, RF feeder cable, and a selection of one of the three antennas mounted on one of the non-metallic stands, shown in Figure 7, is best suited for propagation noise measurements. This system is shown in Figure 11. The measured available noise power spectral density can be expressed as an effective noise temperature, and noise figure (NF) is defined for a reference temperature of 290 K [45]. This method has been adopted by the IEEE as part of its standard definition of noise figure [46], and the characterisation of noise sources using the concept of their effective noise temperature is adopted in our noise measurements.

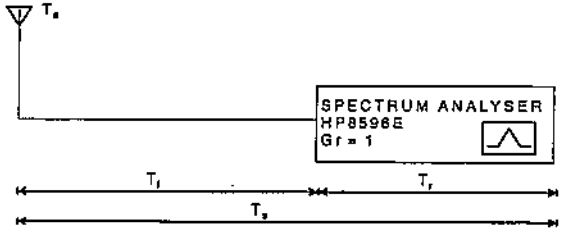

Figure 11: Non-Systematic Noise Measurement System.

A measurement system sensitivity of -123.8 dBm is calculated in Appendix A for the non-systematic noise measurement system fitted with a corner reflector antenna of 15 dBi gain. This sensitivity is adequate for identifying noise sources that can significantly influence the BER performance of data transmissions over the indoor radio channel using digital modulation [38].

4.2.1 Measurement Method of Non-Systematic Noise

There are many variables that can affect the measurement value obtained for any data gathering exercise of non-systematic noise. Some of these variables include the measurement dependence on antenna polarisation, direction, directivity, and height, and long-term variations with time and location [2]. It therefore becomes necessary to completely specify the conditions under which measurements are made. Noise that is non-systematic can attributed to four main categories:

1. Galactic noise: includes cosmic and solar noise.

2. Noise due to absorptive losses: includes attenuation and thermal noise generated as a result of atmospheric constituents.

3. Atmospheric noise: includes electrical disturbances such as lightning and other natural electrical discharges within the atmosphere.

4. Man-made noise: includes unwanted interference from other radio transmissions and incidental radiation from devices or equipment not designed or intended to emit electromagnetic energy.

Galactic noise measurements are not possible due to the sensitivity restriction of our measurement system (-123.8 dBm), and indeed this form of noise which is observable in the approximate range of frequencies from 8 MHz to above one gigahertz virtually disappears at frequencies in excess of 1.5 GHz [47]. Because of its extremely low power level in our frequency band of study (2.3-2.5 GHz), there is no need to measure it.

Noise due to absorptive losses is caused by the attenuation of the transmitted radio wave as it passes through atmospheric constituents such as gases and water vapour, with rain and cloud being the most significant contributors to this form of noise. The indoor radio channel because of the inherently short radio paths (with zero rain or cloud influence) is minimally affected by noise due to absorptive losses, and the

power level attributed to this form of noise is proven to be below the sensitivity of our measurement system. It therefore is not considered as a significant factor in this study as it has been shown that noise power levels that are equal to or below the sensitivity level of the measurement system have negligible affect on BER for data transmissions over the indoor channel [4].

Atmospheric noise is collectively termed static noise. This static noise "consists of impulses, and these non-sinusoidal waves have harmonics whose amplitude falls off with subsequent increase in the harmonic order" [47]. The intensity of atmospheric noise at ground level and for frequencies above 1 GHz is like galactic noise extremely low, and as such has no significant effect on this study.

Man-made noise, in general, far outstrips the noise created by any other source. Due to the very nature of the contributing sources including their location, numbers, frequency of emissions, power intensities etc, the variability of man-made noise makes the characterisation and analysis of this form of noise difficult. Models of man-made noise are still embryonic [2], and the measurement methodology employed to gather data for statistical modelling almost always involves the measurement of noise power in a particular bandwidth over a fixed time period. The noise power can be averaged over the measurement bandwidth, and also peak values can be identified to determine the worst case noise values for the fixed measurement time period. Our non-systematic noise measurement system was capable of both peak and average peak power measurement, and data is presented in both forms in this thesis.

4.2.2 Non-Systematic Noise Measurement Plan

The measurement plan was based upon the collection and collation of non-systematic noise measurement data from various venues. The venues chosen are representative locations where portable radio communications systems may be used, and include the following:

1. University and school lecture rooms and halls.

2. Offices of business.

3. Public use areas such as shopping malls and centres, bus and train stations, hotels, restaurants, food halls, sporting complexes, libraries, municipal buildings, parks, and roadways.

4. Industrial units, factories, and manufacturing plants.

Appendix C lists the specific venues where the measurement of non-systematic noise was undertaken.

The aim of performing measurements at these locations was to not only to identify the contributing sources of non-systematic noise for the 2.3-2.5 GHz band under evaluation by way of classification according to location, but also to characterise the noise power levels present at the selected measurement sites. In order to ensure statistical validity of the measurement results a mathematical specification of the measurement parameters associated with the gathering of non-systematic noise data is required, and this specification is addressed in Section 4.2.3. Noise emission levels and the temporal variance of these emissions have been shown to be directly related to the portion of frequency spectrum being evaluated. Various sources of man-made radio noise have been identified by measurement, and particular interest is taken in ensuring that our measurements included the effects of any equipment present and operating at the measurement venues. Table 1 provides a useful guide of unintentional man-made radio noise sources, which were evaluated as part of this non-systematic noise measurement plan.

Table 1: Man-made radio noise sources

Man-Made Noise Sources-General Category	**Sub-Categories**
Automotive Sources	Ignition circuitry, alternators, generators and electric motors, buzzers, switches, regulators and horns
Power Transport and	Distribution lines, transmission lines, AC

Generating Facilities	transformer substations, DC rectifier stations, generator stations
Industrial Equipment	RF stabilised arc welders, electric discharge machines, induction heating equipment, RF soldering machines, dielectric welder and cutting machines, silicon controlled rectifiers, circuit breakers/switches, microwave heaters, general electronic office machines, elevators
Consumer Products	Appliance motors, microwave ovens, fluorescent, sodium vapour, and mercury vapour lights, spurious emissions from citizen band am transmitters, electronic door openers, television receiver local oscillator radiation, personal computers
Lighting Systems	Neon, mercury, argon, and sodium vapour lights, fluorescent light fixtures
Medical Equipment	Diathermy
Electric Trains and Buses	Overhead power transmission lines and equipment, electric motors

There are three categories of man-made equipment that are specifically designed to emit radio waves as a standard part of their operation:

1. Radio transmitters.
2. Restricted radiation devices.
3. Industrial, Scientific and Medical equipment.

Interference arising from out-of-band emissions from operational radio transmitters is one of the major wireless communication problems affecting the reception quality of

other services using the electromagnetic spectrum. According to [67], the noise class of greatest intensity consists of radio transmitters used in the broadcast services, in the aerospace, land, and maritime mobile-radio services, in fixed point communication services, for radio navigation and position determination, for the transmission of standard time, standard frequencies, radio telemetry, and control signals, and in meteorological monitoring and observation. Spurious emissions from such transmissions is by deduction dependent on the number and types of transmitters that are operating and the frequency, intensity, and duration of the emissions. Consequently the nature of the noise resulting from out-of-band emissions from radio transmitters is most often unique to the site where noise measurement is undertaken, and varies widely between measurement venues.

Restricted radiation devices are transmitters that radiate only moderate electromagnetic fields and are permitted to function without licensing requirement by the spectrum management authorities. The coverage area for these types of transmission is limited to small geographic locales, and some typical equipment in this radiation category include short range radio control transmitters, proximity-radio signposts, and motor vehicle location and auto-locking systems. Out-of-band emissions from restricted radiation devices are generally of lower intensity than those from operational radio transmitters, and like radio transmitters are typically unique to the venue where the noise measurements are taken. Transmitter devices in this group are prohibited from operating if they generate harmful interference to any licensed radio service.

Industrial, scientific and medical equipment that depends on the radiation of electromagnetic waves has been allocated several portions of the radio spectrum termed the ISM bands. One of such bands is the allocated frequency range 2.4-2.4835 GHz, which is part of the spectrum characterised for additive channel noise in this thesis. ISM equipment when operational is prohibited by law from adversely affecting the operation of other authorised users of the radio spectrum, and any out-of-band interference is therefore of concern. Our measurements at selected venues identified microwave ovens as noise sources of sufficient intensity as to warrant in depth analysis of their characteristics and effect on BER for data transmissions employing digital modulation within the 2.3-2.5 GHz frequency range

characterised in this thesis. The result of this analysis is provided in Chapter 5 and Chapter 7.

4.2.3 Mathematical Specification of the Non-Systematic Noise Measurement System Parameters

In order to validate the data gathered during the measurement of non-systematic noise the following measurement parameters require specification:

1 The desired measurement error limit (ξ),

2. The measurement spectral "bin" bandwidth, and the associated start and stop frequencies for each bin (Hz),

3. The bandwidth of the measurement filter (B_f),

4. The time duration of the measurement, termed the minimum sample record length (T_m).

The relationship between ξ, B_f, and T_m is derived from the measurement estimate of the noise power spectral density function $\hat{G}_x(f)$ taken over a minimum sample record length T_m.

The power spectral density function describes the frequency composition in terms of the records mean square value. By filtering the noise time sample record with a sharp cut-off bandpass filter of bandwidth (B_f), and then calculating the average value of the squared filter output ($\overline{V_x^2}$), an estimate value of the mean square value $E[\overline{V_x^2}(f,B_f)]$ is obtained. This value will be an unbiased and consistent estimate of the true value as the averaging time (T) approaches infinity, therefore:

$$E[\overline{V_x^2}(f,B_f)] = \lim_{T\to\infty}\frac{1}{T}\int_0^T x^2(t,f,B_f)dt \qquad (4.1)$$

where $x(t,f,B_f)$ represents the filter output, and $\overline{V_x^2}(f,B_f)$ is the mean square value of x(t) associated with a filter bandwidth B_f centred on frequency (f).

The power spectral density $G_x(f)$ can be defined as [65]:

$$G_x(f) = \lim_{B_f \to 0} \frac{\overline{V}_x^2(f,B_f)}{B_f} = \lim_{\substack{T \to \infty \\ B_f \to 0}} \frac{1}{BT} \int_0^T x^2(t,f,B_f)dt \qquad (4.2)$$

where B is the total bandwidth of the frequency range of interest, and the measurement is performed by sliding the narrowband filter of bandwidth B_f over B.

In terms of $G_x(f)$ the mean square value of x(t) between any two frequency limits f_1 and f_2 is given by:

$$\overline{V}_x^2(f_1,f_2) = \int_{f_1}^{f_2} G_x(f)df \qquad (4.3)$$

$G_x(f)$ is always a real valued non-negative function and its estimated value is determined for twenty spectral bins each being 10 MHz wide to cover the frequency band from 2.3-2.5 GHz. The filter used in the measurements was set at $B_f = 10$ kHz bandwidth which is sufficiently small when compared to the bin size of 10 MHz. The minimum sample record length T_m to achieve a desired error limit ξ for a chosen resolution bandwidth B_f is found from [65]:

$$\xi = \frac{S_{dev}[\hat{G}_x(f)]}{G_x(f)} \approx \frac{1}{\sqrt{B_f T_m}} \qquad (4.4)$$

where:

S_{dev} - standard deviation.

Therefore:

$$T_m \approx \frac{1}{B_f \xi^2} \qquad (4.5)$$

In measurements of non-systematic noise a desired error limit of 0.1 % was set, then from Equation (4.5) a minimum real time sample record length, T_m, of 100 seconds is

required. The record length chosen for all noise measurements was therefore selected as 2 minutes, this being the closest acceptable whole minute.

4.3 Calibration of the Monopole Antenna for plane-wave noise measurements

When a receiving antenna is illuminated by an electromagnetic incident wave, the component of the electric field parallel to the monopole antenna has an amplitude (E_R) as defined in Equation (3.19). A relationship can now be derived between the value of E_R and the voltage (V_L) delivered to a load impedance (Z_L) connected to the antenna terminals. This relationship is achieved by the determination of a frequency dependent factor appropriately termed the "antenna factor" (AF) which, as defined by the IEEE standard dictionary, "when properly applied to the voltage at the input terminals of the measuring instrument, yields the electric field strength in volts per metre and the magnetic field strength in amperes per metre". The antenna can be modelled as an equivalent Thevenin voltage source to calculate the voltage magnitude V_L across the actual load impedance Z_L. The theoretical expression for the antenna factor of a general receiving antenna is then:

$$AF = \frac{1}{\lambda}\sqrt{\frac{\eta\pi}{G_T R_S}}\left|1+\frac{Z_S}{Z_L}\right| \tag{4.6}$$

where G_t is the gain of the receiving antenna relative to an isotropic antenna, and R_s is its radiation resistance. For all our calibrated noise measurements a monopole antenna of one quarter wavelength at the measurement frequency was used. Because the monopole is resonant at only one frequency, a range of vertical radiators was required to cover the 2.3-2.5 GHz frequency band under evaluation. By ensuring that the antenna is resonant then Equation (4.6) can be applied to compute the theoretical value of AF at any selected frequency. G_t the maximum directive gain of the monopole receiving antenna relative to an isotropic antenna has been shown [43] to be 1.6438 (2.1586 dB), with $Z_s = R_s = 36.5$ ohms at resonance. For all our measurement systems Z_L, the impedance as seen by the antenna, consisted of the characteristic impedance of the antenna coupling cable and the input impedance of the

measurement instrumentation connected as a termination on the end of this cable. Specifications and measurement has shown this combined termination to be 50 ohms resistive, Z_L is therefore 50 ohms. The substitution of $G_r = 1.6438$, $Z_s = R_s = 36.5$, $Z_L = 50$, $\eta = 120\pi$ and $\lambda = 0.3$ / frequency (GHz) into Equation (4.6) and taking logarithms yields:

$$AF = 20\log_{10}(\text{frequency(GHz)}) + 28.18194 \quad [\text{dB}] \qquad (4.7)$$

Equation (4.7) results in an antenna factor of 35.78 dB (61.56 numeric) for a frequency of 2.4 GHz which is at the centre of our measurement band of interest, 35.42 dB (58.996 numeric) at 2.3 GHz, and 36.14 dB (64.126 numeric) at 2.5 GHz. This variation in AF must be accounted for when computing received electric field intensities from our noise measurement data.

4.4 Non-Systematic Noise Measurement Procedure

The venues selected for the measurement of non-systematic noise are given in Section 4.2.2. The measurement procedure adopted at each venue was as follows:

1. Set up the non-systematic-noise measurement system as shown in Figure 11, then select and mount the omnidirectional colinear antenna model VO10-2325 on one of the non-metallic stands as depicted in Figure 7.

2. Using the measurement parameters determined in Section 4.2.3 set the spectrum analyser resolution bandwidth (RBW) to 10 kHz, the RBW is equivalent to B_f. Then perform twenty measurements each of 2 minute duration to meet the requirement of T_m, one measurement for each of twenty spectral bins of 10 MHz width to cover the frequency band 2.3-2.5 GHz. Enable the peak hold option of the spectrum analyser for each measurement. This allows the visual detection of noise levels that exceed the systematic noise during the 2 minute measurement period. Save all the measurement results to files within the spectrum analyser memory.

3. If non-systematic noise is observed during the measurements performed in 2, then, by visual inspection of the spectrum analyser screen trace determine if the nature

of the noise is impulsive, continuous, or a combination of both. Repeat the measurements and determine, again by visual inspection of results, if a similar measurement result is obtained.

4. . If the measurement result of non-systematic noise observed in 3 is repeatable, then connect the directional corner reflector antenna model DRT 2415 in place of the omnidirectional colinear antenna model VO10-2325, ensuring that the same vertical polarisation is maintained. Now perform a series of measurements each of 2 minute duration at intervals of 10 degrees azimuth separation. Analyse the results for each measurement and determine if a particular direction provides a higher level of noise power density. If so, then a spatially separated set of readings can also be completed to assist in directional location of the noise source, with consideration also being given to multipath reflections. If the noise source exhibits uniform power directionality, then identifying it can require analysis over a significantly longer time period, such as diurnal measurements, to determine for example the existence of any cyclic pattern which may assist in location of the source should it be man-made.

5. Once the source of non-systematic noise has been identified, a series of measurements are completed with the calibrated quarter wave monopole antenna (replacing the DRT 2415 corner reflector antenna). This antenna has an AF defined by Equation (4.7) in Section 4.3, and the application of the AF to the measurement data provides the received free space electric field intensity at the receive antenna location for the measurement.

The five preceding steps were adopted in the first instance to ascertain the existence or otherwise of non-systematic noise within our frequency band of interest, namely, 2.3-2.5 GHz. The analysis of measured data allowed the identification of noise sources which radiated electromagnetic waves of sufficient power intensity at the receive antenna as to exceed the system measurement sensitivity after propagation path losses (Appendix A). The measurement data represent the peak noise value recorded for all frequencies in our band of interest during the two minute recording period. The spectral display obtained by this measurement method can be termed a "peak signature", and it is representative of the highest amplitude reading obtained for each frequency in the band during the two minute reading period. Figure 12 provides

an example of a spectrum analyser peak signature display obtained from a two minute recording of the random noise bursts emanating from an operational microwave oven. The measurement was performed using the colinear antenna at a distance of two metres from the oven.

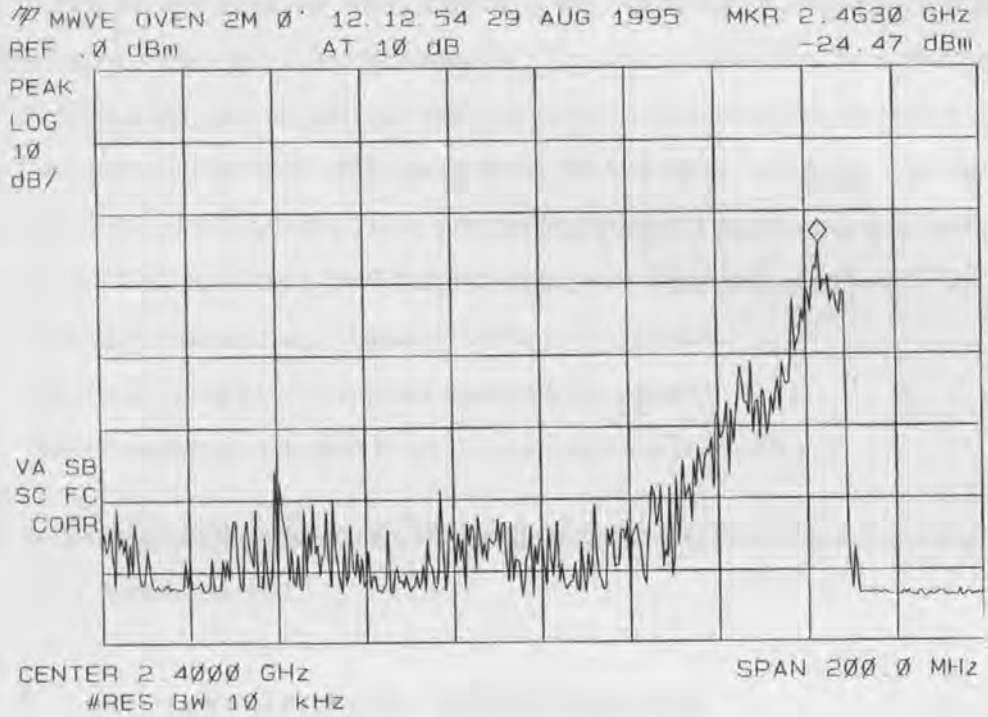

Figure 12: Peak signature spectrum analyser display for a single operational microwave oven at 2 m range using omnidirectional colinear antenna.

In addition to gathering the peak amplitude measured data values, the use of the view function of the spectrum analyser provided sample data representative of any random noise bursts with time. A recording of 50 data samples for each 10 MHz bin (20 bins covering the 2.3-2.5 GHz frequency range) provided an estimate of "average peak noise power".

The estimate values of peak hold noise power and average peak noise power are presented in Sections 4.5 and Chapter 5. These estimate values were obtained from measurement data and they characterise the only identified noise sources in the 2.3-2.5 GHz frequency range identified as above the system measurement sensitivity of –123.8 dBm.

4.5 Non-Systematic Noise Measurement Results

The completion of the measurement plan (outlined in Section 4.2.2), and analysis of collected data resulted in the clear identification of three sources of non-systematic noise worthy of consideration when modelling the indoor radio propagation channel as a medium for high speed data transmission. The sources identified by measurement were all man-made, and as such are categorised in accordance with Section 4.2.2 as radio transmitters, restricted radiation devices, or industrial, scientific and medical equipment. The non-systematic noise sources that generate electromagnetic radiation in the 2.3-2.5 GHz frequency band being evaluated are identified as follows:

1. Building Alarms radio frequency transmission signals.
2. Pay Television radio frequency transmission signals.
3. Electromagnetic radiation from Operational Microwave Ovens.

In the following sections the results obtained from the analysis of measurement data are presented, and analysed.

4.5.1 Non-Systematic Noise Sources

4.5.1.1 Building Alarms

These type of alarms are typically found in buildings, and form part of the building security system. The electromagnetic radiation associated with these building alarms fall in the restricted radiation device category given in Section 4.2.2. The alarms were identified at two measurement venues, the first being Wilson's Engraving works, and the second the Whitford City Shopping Centre (see Appendix C for venues). The physical location of the alarm unit, responsible for the emission of electromagnetic radiation in the measurement band of interest, was determined by the adherence to the measurement methodology oudined in step (4) of Section 4.4. When the location of the alarm unit was determined, then, a calibrated measurement was performed making use of the resonant monopole antenna as detailed in step (5) of Section 4.4. The peak signature spectrum analyser display for the building alarm unit located at Wilson's

Engraving Works is given as Figure 13. The peak signature measurement depicted as Figure 13 was obtained at a range of 1 m from the alarm unit, with the corner reflector antenna used as the measurement antenna.

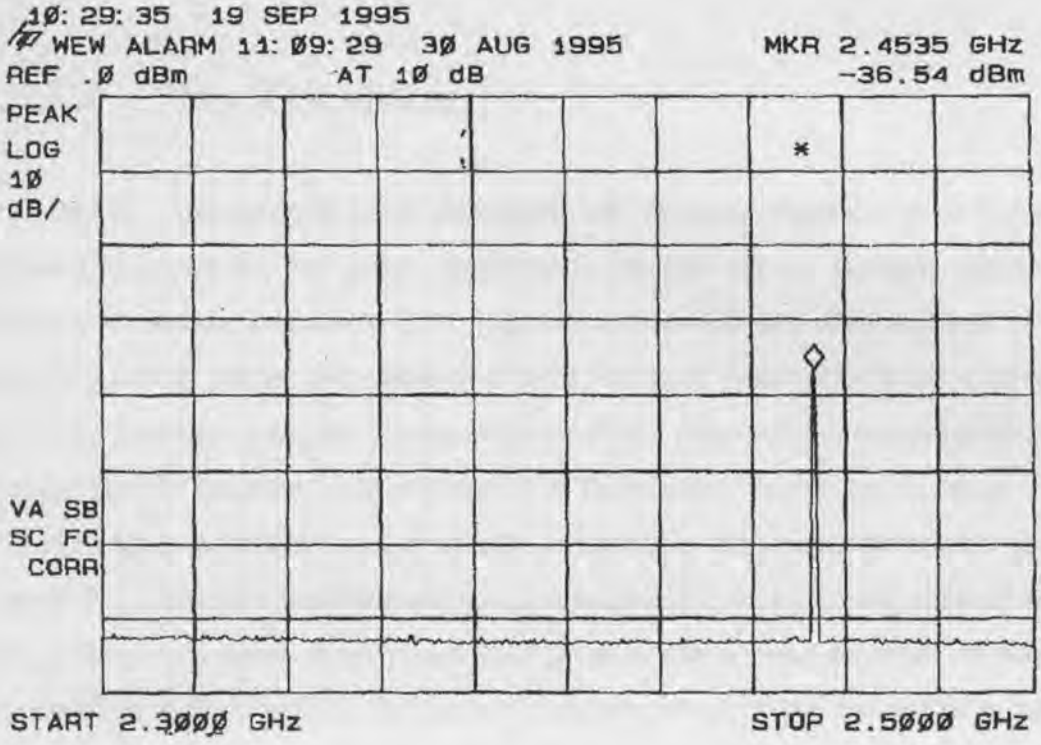

Figure 13: Peak signature spectrum analyser display for a building alarm unit at 1 m range using corner reflector antenna.

The maximum received power level for this measurement is shown in Figure 13 as -36.54 dBm at a frequency of 2.4535 GHz as shown by the marker (MKR) values located at the top of the figure, and positioned to the right hand side. The calibrated measurement using the resonant monopole antenna, as described in Section 4.3, was performed at 5 m range from the building alarm unit. This measurement resulted in a maximum received power level of -61.33 dBm. A similar calibrated measurement performed at Whitford City Shopping Centre at 5 m range provided an estimate of -62.87 dBm maximum receive power level, at a frequency of 2.4505 GHz. Both these signals fall within the 2.4-2.4835 GHz ISM band of interest, and are of sufficient intensity as to be of concern when co-location with other receivers such as WLANs operating within the same ISM band occurs. Due to the unlicensed nature of the 2.4-2.4835 GHz ISM band, a measurement evaluation of any proposed site before

installation of a new system is recommended, as this can identify the existence or otherwise of electromagnetic radiation from building alarms. The operating frequency of any proposed new system can then be selected to minimise interference from the existing alarm/s.

4.5.1.2 Pay Television

Pay television has recently been introduced into Western Australia as a licensed commercial enterprise, its' prime objective is the delivery of multiple television channels to paying customers. The channels are modulated onto separate radio frequency carrier waves, and transmitted over terrestrial radio links to the customer receivers, which are typically located within a 20 km radius of the transmission site. Electromagnetic radiation associated with Pay Television transmissions is categorised in Section 4.2.2 as being sourced from radio transmitters. When consideration is given to these Pay Television transmissions as a source of noise, then their significance is of little consequence unless these transmitters produce out-of-band spurious emissions. As described in Section 4.2.2 this form of spurious emission interference from radio transmitters has been identified as one of the major interfering noise sources that is likely to affect the reception quality of other services using the electromagnetic spectrum [67], and as such warrants due consideration. Figure 14 shows the peak signature measurement of a group of the Pay Television modulated carrier waves. The measurement was obtained at the South Perth River Foreshore venue, and the corner reflector antenna was used for the measurement. The Pay Television transmission site (Perth Centre Point Tower) is a direct line of sight distance of 2.1 km from the measurement venue, and the propagation path is unobstructed, being primarily over water.

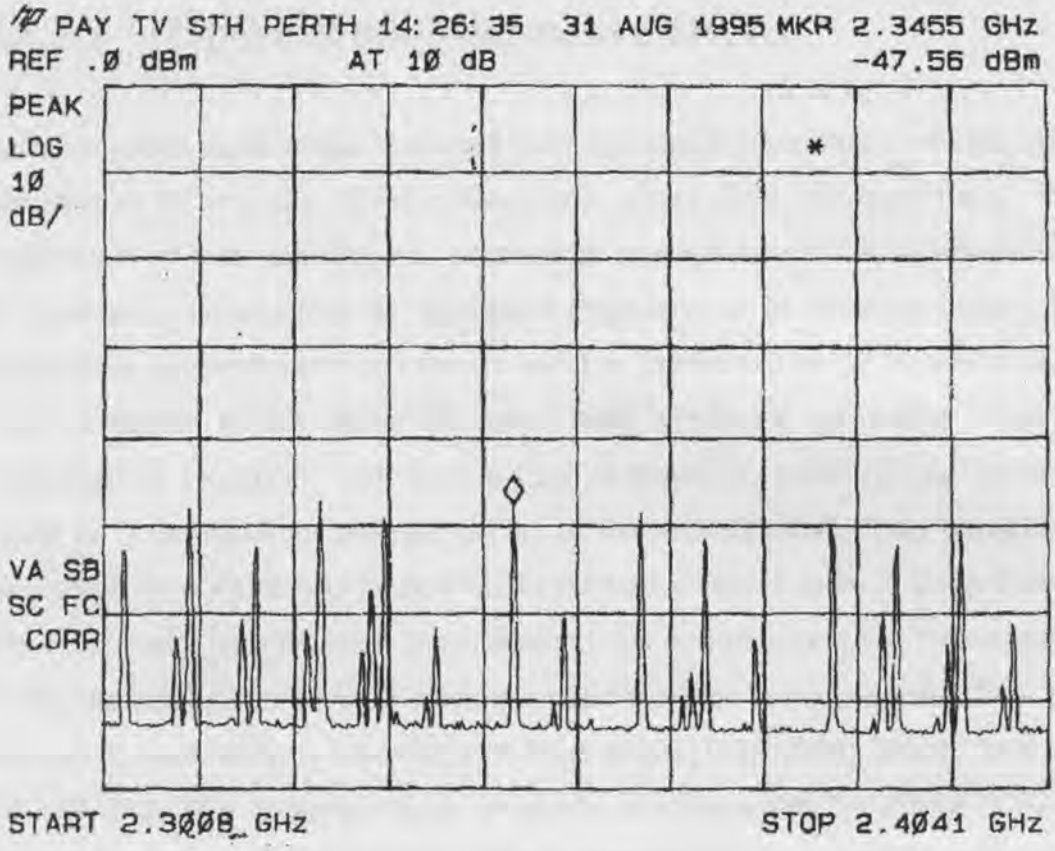

Figure 14: Peak signature spectrum analyser display for Pay Television.

For the Pay Television transmission signal shown "tagged" by the diamond shaped MKR in Figure 14, a maximum received power level of -47.56 dBm at a frequency 2.3455 GHz is measured. A calibrated measurement performed at the same location with the resonant monopole antenna provided an estimate of -61.61 dBm maximum receive power level, at a frequency of 2.3455 GHz. The frequencies identified by this measurement, shown as Figure 14, were verified with the spectrum management authorities as being licensed transmissions, and are not considered as spurious out-of-band interference. However the existence of any spurious electromagnetic transmissions, which emanate from transmitters, can therefore be identified by performing measurements at any site where the installation of any new system operating in the 2.4-2.4835 GHz ISM is proposed, and then validating the spectral signature obtained by measurement against technical license specifications. Where an offending transmitter is identified as a licensed service, then collusion with the appropriate spectrum management authorities generally results in action to remove the interference.

4.5.1.3 Operational Microwave Ovens

Electromagnetic radiation that is sourced from operational microwave ovens has been identified at the majority of the measurement venues listed in Appendix C. The proliferation of both domestic and commercial microwave ovens has introduced a non-systematic noise source of significant magnitude as to seriously impact the transmission performance of any service which is operational in the frequency band under evaluation in this thesis. The noise from operational microwave ovens is categorised in accordance with Section 4.2.2 as Industrial, Scientific and Medical. Figure 12 is the spectrum analyser display of the peak signature of an operational microwave oven which was located within the staff common room at Edith Cowan University measurement venue. The analysis of this measurement trace indicates that the highest peak power level of electromagnetic radiation being generated from the microwave oven which is behaving as a noise source, is spectrally located between 2.4-2.47 GHz. This frequency range is directly coincident with the 2.4-2.4835 GHz ISM band employed for the transmission of data using BPSK and QPSK modulation as an integral part of networks such as WLANs.

4.6 Conclusions

For the indoor radio propagation channel we have investigated and characterised additive channel noise present in the 2.3-2.5 GHz frequency band. The noise data was obtained from measurements performed at venues listed in Appendix C of this thesis. Although time precluded a more extensive measurement program, the adherence to the method and measurement plan given in Sections 4.2.1 and 4.2.2 respectively identified building alarms, pay TV, and operational microwave ovens as three potential non-systematic noise sources. Care was taken to measure the level of noise emitted from devices such as light switches, elevator door switches and associated contacts, photocopier machines, and computers at locations where these existed. Photocopiers and elevator door switches are identified as noise sources in the 2.44 GHz band by [78]. The noise emitted by these devices was found to be below the measurement sensitivity of our system (-123.8 dBm). Operational personal computers

with their associated switched mode power supplies are known to emit electromagnetic radiation in the 2.3-2.5 GHz band, but the noise was also found by measurement to be below the measurement system sensitivity of our system. The sensitivity chosen for our noise investigations of –123.8 dBm is 32.8 dB more sensitive than the RCR standard receiver [76] and therefore allows the identification of noise levels that have sufficient intensity to significantly influence BER performance of data transmissions for equipment operated over indoor radio paths. The measurement campaign identified noise emissions from operational microwave ovens at significant level to degrade the BER performance of indoor radio systems. The level of noise varied across the 2.3-2.5 GHz band when the oven was operational and was variable with time. Noise levels entering the receive antenna at 5 metre oven to antenna separation approached and in some cases exceed that of typical reference receiver levels for indoor transmission systems. Microwave oven generated noise was found to be the only form of noise to warrant in depth evaluation of its influence on BER performance for data transmitted over the indoor radio propagation channel. This form of noise is characterised in detail in Chapter 5 and its influence on BER analysed in Chapter 7.

Chapter 5

Analysis of the Non-Systemic Noise Generated by Operational Microwave Ovens

---

An operational microwave oven can be considered to act as a transmit antenna located at or near the origin of a spherical co-ordinate system as shown in Figure 15.

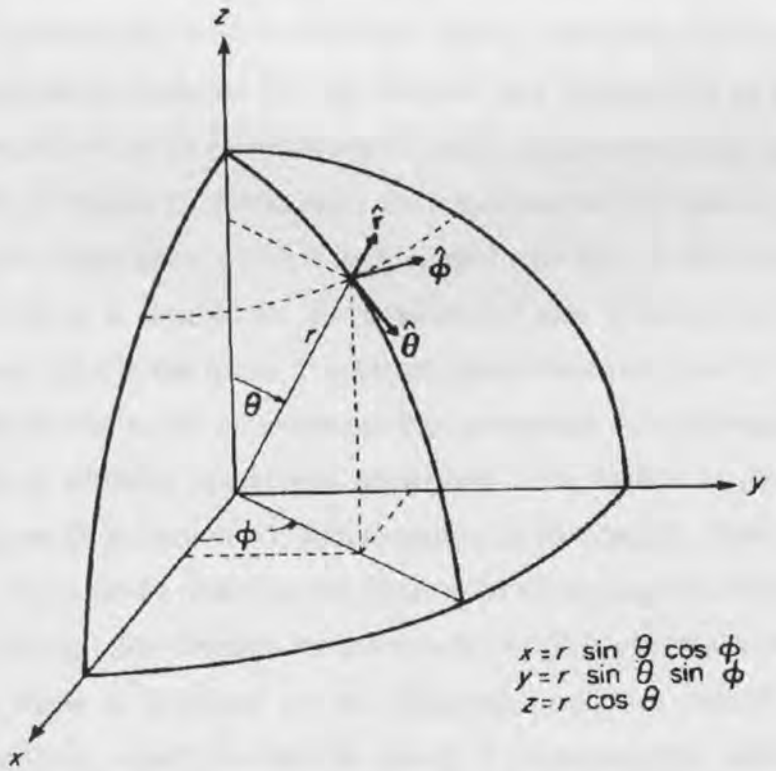

Figure 15: Spherical Co-ordinate System.

The shape of any radiation pattern can be considered to be independent of the measurement range (r) provided that r is chosen sufficiently large relative to the wavelength of the transmitted electromagnetic radiation, and the largest dimension of the antenna system. When this is true the magnitude of the electric field strength received at r is termed a "far field" value [42], and as such E_R can be found from Equation (3.19). Because the value of power being transmitted from an operational microwave oven has been shown to be dependent on frequency, and therefore wavelength, then as determined by the measurement procedure of Section 4.4 a series of measurements were required for the twenty spectral bins each of 10 MHz width to cover the frequency band 2.3-2.5 GHz. The measurements were performed at r = 5 m, and at increments of ϕ = 10 degrees in the x-y plane of the spherical co-ordinate system shown in Figure 15 (θ = 0 for all measurements). The 5 m range is considered sufficient to meet the far field requirement, this range being approximately twenty times the typical maximum dimension of the microwave oven, where the oven is acting as the transmit antenna, and approximately forty times the wavelength of the electromagnetic radiation that was identified to be emanating from operational ovens at or near many of the measurement venues. All measurements were performed using the calibrated resonant one quarter wavelength (1/4 λ) monopole antenna (Appendix B). The measurements indicated that the average peak power level of the random noise bursts is uniform for all values of angle ϕ and θ, at a constant range r, for the co-ordinate system of Figure 15. Additionally the measurement data showed no clear E-field polarisation dependency, which is in agreement with data of other research [75]. Vertical polarisation is selected for all measurement data gathered for analysis of microwave oven noise in this thesis. The average peak measured power of the random noise bursts delivered to the measurement instrumentation load impedance (Z_L) at r = 5 m for three different operational microwave oven models is plotted as the ordinate of Figure 20 in Section 5.1, with frequency as the abscissa. From Figure 12 a characteristic shape can be observed that typifies the electromagnetic radiation levels encountered during other research measurements [4] [76]. An explanation for the characteristic shape is proffered by the following qualitative description of the magnetron oscillator, which provides the source of electromagnetic radiation for all microwave ovens.

5.1 The Microwave Ovens Magnetron

Most operational microwave oven magnetrons produce electromagnetic radiation at a nominal frequency of 2.45 GHz. The electromagnetic radiation is produced by the magnetron and coupled to the cooking cavity by the use of a waveguide. The CW frequency produced by the magnetron has a 50 % duty cycle which for ovens that run off a 60 Hz mains power outlet results in a cadence of 8.33 millisecond on and 8.33 millisecond off. For an oven running off a 50 Hz mains power outlet the cadence is 10 milliseconds on and 10 milliseconds off. For the on period of the duty cycle one would expect the CW frequency to remain relatively stable, but measurements have shown that this is not the case. The variation in frequency is attributed to the behaviour of the magnetron itself when in two specific operational states. The first state can be defined as when the magnetron anode voltage is suddenly varied to bring it into or out of a state of multi-cavity resonance, and the second state can be defined as that when the magnetron is operational in resonance with a constant anode voltage. The SWR as seen by the magnetron oscillator is dependent on the load that is presented by the waveguide feed and material occupying the cooking cavity. In particular the type and volume of material in the cooking cavity and the rotation of that material on the ovens cooking turntable presents a constantly changing SWR to the magnetron oscillator.

The microwave oven magnetron itself consists of a number of identical resonator cavities arranged in a circular pattern around a cylindrical cathode as shown in Figure 16.

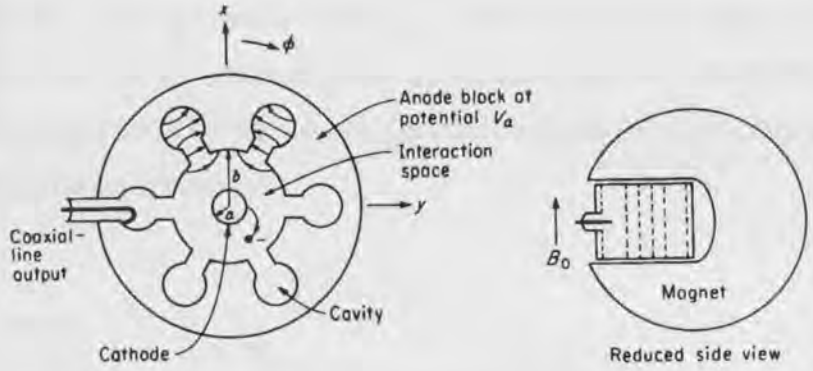

Figure 16: Multi-cavity Magnetron.

Also shown in Figure 16 (the reduced side view of the multi-cavity magnetron) a permanent magnet is employed to provide a strong magnetic field normal to the cross section. The electronics of the microwave oven provide a high positive voltage to the anode (V_A) relative to the cathode during the on period of the oven duty cycle. A heating filament which is typically powered by a 3.3 volt supply heats the cathode to cause it to emit electrons which are accelerated towards the anode block by the presence of the high positive voltage present during the on period. The electron cloud is deflected by the influence of the magnetic field (B_0) produced by the permanent magnet. From electromagnetic fundamentals B_0 produces a force $-ev_r$ in the azimuth direction, which changes the electrons trajectory in the direction of this force. For the cathode radius (a) and anode radius (b) shown in Figure 16 the voltage potential ($V(r)$) at any radius r is given by:

$$V(r) = V_a \left[\ln(r/a)\right]/\left[\ln(b/a)\right] \tag{5.1}$$

At radius r the velocity of an electron is from electromagnetic fundamentals:

$$v(r) = \sqrt{\left[2CV(r)\right]} \tag{5.2}$$

Where C is defined as (e/m) the electron charge (e) to mass (m) ratio $\cong 1.76 \times 10^{11}$ coulombs / kg.

Also electron velocity (v) = $\omega_e r$ where ω_e is defined as the angular velocity of the electron.

Circular motion of the electron will occur at radius r about the cathode if the radial electric field force on the electron given by - $e\,E_r = eV_a \,/\, [r\ ln\ (b\,/\,a)\ ]$ and the outward centrifugal force on the electron $(m\,v^2/r)$ are in equilibrium with the inwardly directed magnetic force such that:

$$\frac{m v^2}{r} + \frac{eV_a}{r \ln\left(\frac{b}{a}\right)} = e\ v\ B_0 \tag{5.3}$$

Substitution for $v = \omega_c r$ into Equation (5.3) and transposing yields:

$$\omega_c^2 + \frac{e\ V_a}{m\ r^2 \ln\ (b/a)} = \frac{e\ \omega_c\ B_0}{m} \tag{5.4}$$

Substitution for $e/m = C$ into Equation (5.4) and transposing to solve for the anode accelerating voltage V_a then:

$$V_a = \left[\omega_c\ r^2 \ln\left(\frac{b}{a}\right)\right]\left[B_0 - \left(\frac{\omega_c}{C}\right)\right] \tag{5.5}$$

An anode voltage of this value allows the electrons to exhibit circular motion at angular frequency equal to ω_c at a radius equal to r.

A multi-cavity magnetron is a structure that is periodic in the azimuth or ϕ direction as shown on Figure 16, if there are N cavities the period in ϕ is $2\pi/N$. The presence of an electromagnetic field that propagates in the ϕ direction with a phase velocity equal to the electron velocity $\omega_c\ r$ is explained by "Floquet's Theorem" on spatial harmonics where each field component can be expanded in the form:

$$\psi(r,\phi) = \sum_{n=-\infty}^{\infty} e^{-j\beta\phi - j2n\pi\ \phi/p}\ \psi_n(r) \tag{5.6}$$

The period $p = 2\pi / N$ therefore:

$$\psi(r,\phi) = \sum_{n=-\infty}^{\infty} \psi_n(r)\, e^{-j\beta\phi - jnN\phi} \tag{5.7}$$

Because the structure closes on itself, $\psi(r, 2\pi) = \psi(r, 0)$, and the only possible values of β that make $\beta 2\pi$ equal a multiple of 2π are:

$$\beta_m = m \qquad m = 0, \pm 1, \pm 2, \ldots\ldots \tag{5.8}$$

With the value of β specified, a corresponding angular frequency ω is also specified for example ω_m for the m^{th} mode. Therefore when $\omega = \omega_m$, we obtain a value m for β_m, and thus a typical field component will have the following form:

$$\psi_m(r,\phi)e^{j\omega_m t} = \sum_{n=-\infty}^{\infty} \psi_n(r)e^{-j(m+nN)\phi + j\omega_m t} \tag{5.9}$$

The phase velocity in the azimuthal direction (ϕ) for the n^{th} spatial harmonic of the m^{th} resonant mode is:

$$v_{p,nm} = \frac{\omega_m r}{\beta_{mn}} = \frac{\omega_m r}{m + n N} \tag{5.10}$$

at radius r ; that is, angular phase velocity is ω_n / β_{mn}

The usual mode employed by magnetron oscillators such as those used in microwave ovens is the π mode, where the phase change between adjacent cavities is 180^0, or π radians. Each of the N cavities of the magnetron with its input gap behaves as a short-circuited transmission line of one-quarter wavelength, and therefore has a maximum electric field across the gap. For the π mode the field is oppositely directed for adjacent cavities as shown in Figure 16. For the π mode , $\beta_m \phi = m \phi$ must equal π for a change in ϕ equal to one period $2\pi / N$. Therefore $m = N / 2$, and the phase velocity for the n^{th} spatial harmonic becomes:

$$v_{p,nN/2} = \frac{2\omega_{N/2}\, r}{N(1+2n)} \tag{5.11}$$

For interaction to occur at a particular radius r between the electron cloud accelerating towards the anode and one of the spatial harmonics the anode voltage V_a must be such that:

$$\omega_c \cdot r = v(r) = v_{p,\pi/2} \tag{5.12}$$

or:

$$\omega_c = \frac{2\,\omega_{\pi/2}}{N(1+2N)} \tag{5.13}$$

The necessary value for V_a to obtain synchronism between the alternating harmonic field and the electron cloud can be found from Equation 5.5. The relationship between Equation 5.5 for the anode voltage V_a and Equation 5.13 for the angular frequency ω_c at radius r determines the magnetron oscillation frequency. For a fixed value of V_a, a magnetron of fixed dimensions a and b as shown in Figure 16 will exhibit at a nominal radius r an oscillation at angular frequency ω_c. Variation of value V_a for the magnetrons in microwave ovens occurs at the beginning and end of the 10 millisecond "on" period for 50 Hz mains powered ovens and the 8.33 millisecond "on" period for 60 Hz mains powered ovens. The derivation of the "on" "off" cadence is directly attributed to the method employed in the microwave oven to produce the magnetron anode voltage V_a relative to its cathode. In most microwave ovens use is made of a high voltage step up transformer to step the mains voltage (240V AC or 115V AC) to approximately 2400V AC at the secondary output. A voltage doubler half wave rectifier circuit is connected at the output of the high voltage step up transformer secondary winding to supply the "on" anode voltage V_a pulses to the magnetron anode at a voltage value that rapidly rises from 0 volts to approximately positive 4000 volts on application. 4000 volts is the average, the actual voltage varies slightly between the three ovens evaluated. The resultant variation in angular frequency ω_c and the associated measured frequency f_c, where $f_c = \omega_c / 2\pi$, is plotted against the anode voltage range V_a applied during the "on" pulse for three sample ovens tested on a magnetron performance diagram shown as Figure 17.

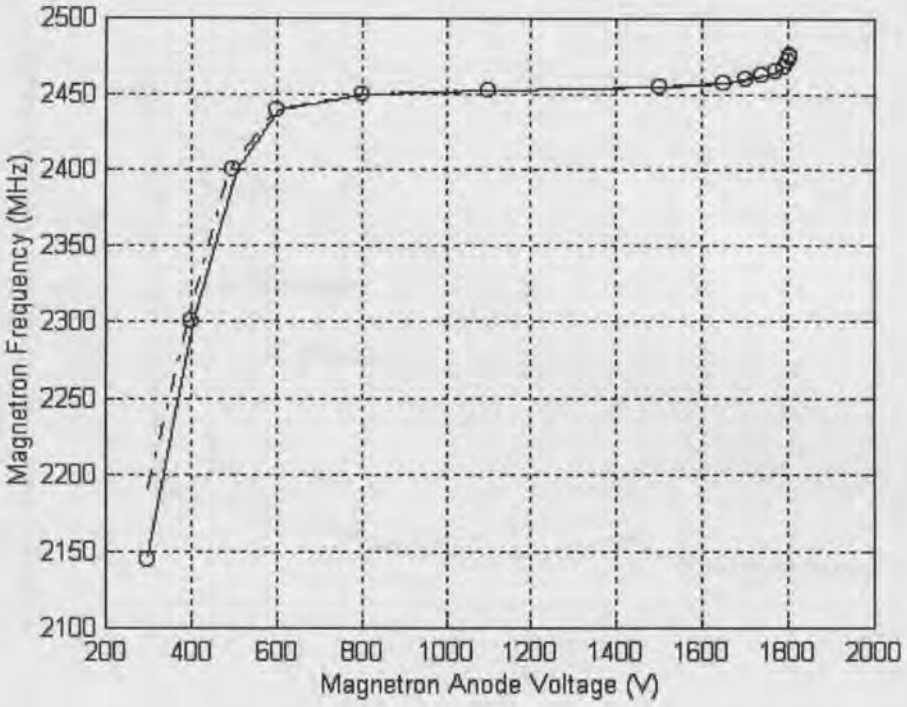

Figure 17: Magnetron Performance Diagram

O	Whirlpool Magnetron
Solid	Mitsubishi Magnetron
-.	Toshiba Magnetron

As shown by Figure 17 the three microwave oven magnetrons exhibit near identical change in frequency for changes to the magnetron anode voltage. At an anode voltage of approximately 800 volts the rate of frequency change significantly reduces and the magnetrons operating frequency of typically 2450 MHz is obtained, increasing the anode voltage above 800 volts to 1800 volts results in only 15-25 MHz increase in frequency to 2465-2475 MHz. This upper cut-off frequency is exhibited in all field measurement evaluations of emissions from operational microwave ovens, and has been verified by the measurement plot of three magnetrons as a real upper limit to the frequency of operation. The upper cut-off frequency for the three microwave ovens is plotted from field measurements as Figure 18.

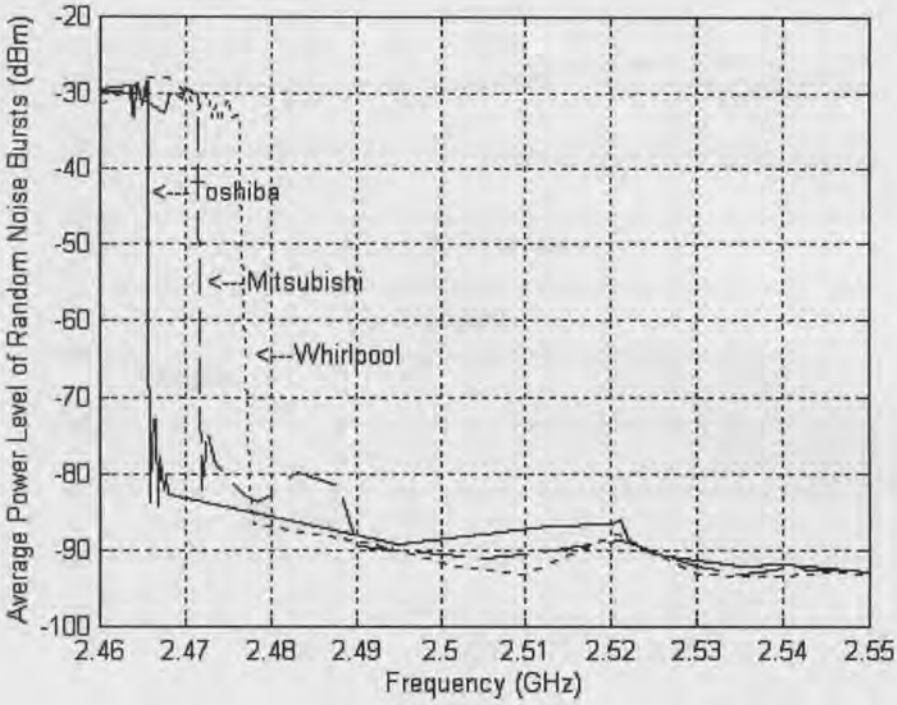

Figure 18: Magnetron Upper Cut-Off Frequencies

The identification of the existence of measurable upper cut off frequencies led to further data gathering and analysis to see if lower cut off frequencies that could be verified by measurement existed. The measurements previously conducted [4] [76] revealed a gradual fall off in power level at frequency values below 2.46 GHz extending down to approximately 2.15 GHz. By extending the observation time for each measurement period from 2 minutes to 15 minutes a significant change of shape to the spectrum analysers peak hold plot was observed. The longer measurement period allowed identification of received power radiated by the operational microwave ovens at frequency values not evident in the plots for the 2-minute measurement period. The existence of a lower cut-off frequency for all three ovens evaluated is clearly identified by measurement, with the results plotted from the measurement data as Figure 19.

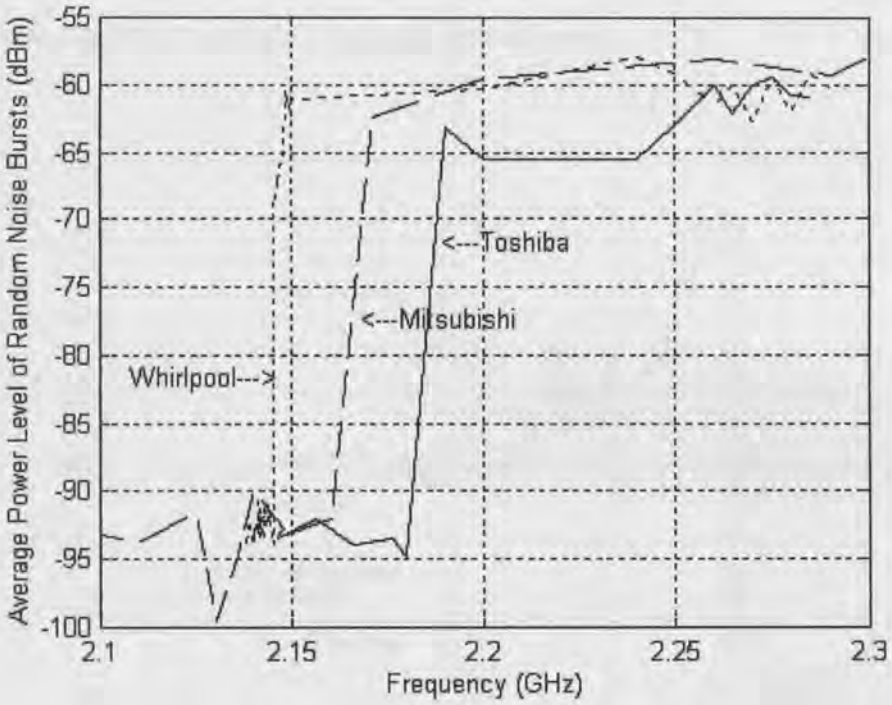

Figure 19: Magnetron Lower Cut-Off Frequencies

The results were surprising, as field measurements had not shown a significant step fall in power level of approximately 30 dB at lower frequencies. This finding is attributed to the very short duration of the noise burst combined with the short observation period of the measurement, and the spectrum analyser used for the measurement analysis, which has a minimum sweep time of 20 milliseconds. The magnetron anode voltage V_a applied during the "on" pulse rises from 0 volts to 800 volts in a measured time of typically 0.45 milliseconds. From Figure 17 it can be seen that a rapid frequency change in the order of 2.15 GHz-2.45 GHz can occur during this 0.45 millisecond time period. A similar reverse frequency change occurs when the voltage doubler action turns the anode voltage off. For the shorter spectrum analyser peak hold observation time of 2 minutes (with its 20 milliseconds minimum sweep time) these short duration "on and off frequency chirps" are often missed and not displayed by the analyser. The longer observation time of 15 minutes allowed their detection, which explains the change in shape to the typical peak hold plot, and the consequent identification of the existence of a lower cut –off frequency for the magnetrons.

Figure 20 depicts the overall peak hold plots for the three operational microwave ovens evaluated by the longer 15 minute measurements.

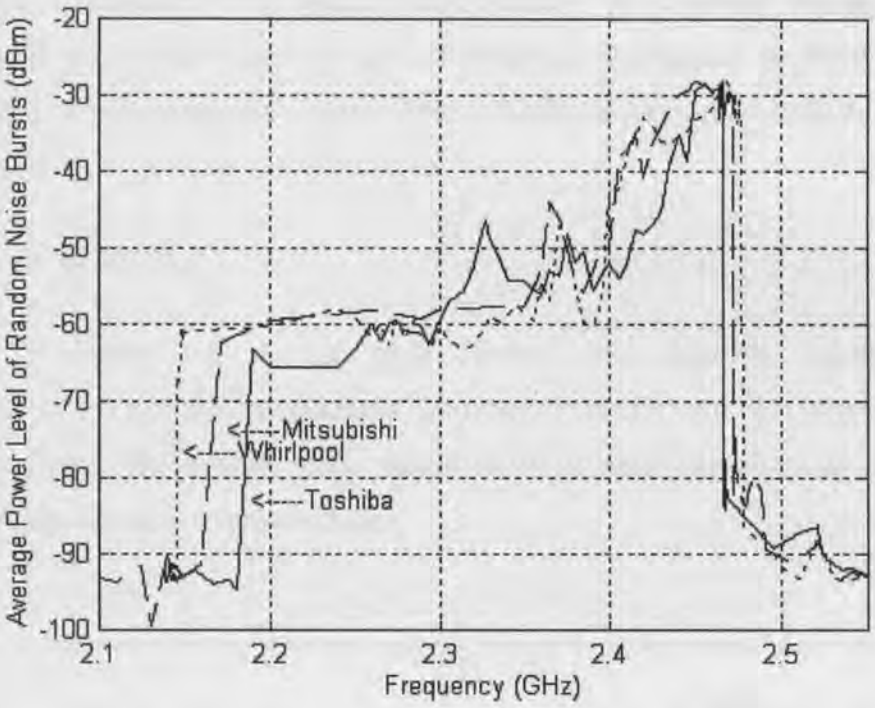

Figure 20: Average peak measured power level of the random noise bursts from an operational microwave oven at range 5 metres (receive antenna :- resonant ¼ λ monopole).

5.2 Average Peak Electric Field Intensity

An accurate estimate of the received electric field intensity E_R at the measurement antenna position can only be obtained by the correct application of AF correction, where AF is given by the relationship in Equation (4.7). Also, as stated in Section 4.3, AF is applied to the voltage at the input terminals of the measurement instrumentation. It is therefore necessary to convert the average peak power level values, given as the ordinate of Figure 20, to voltage levels that are representative of the average peak voltage values across the input of the receive feeder cable. The receive feeder cable being defined as the cable that connects the receive antenna to the measurement instrumentation. By performing the necessary computations (Appendix

E), two arrays each with twenty elements are obtained, one array representing the AF value at centre frequency of the twenty measurement bins, and the other the average peak voltage values computed from the average peak power level measurements for the same frequencies. The average peak voltages (V_{50}) in the voltage array are calculated for a real value of $Z_L = 50$ ohms as determined in Section 4.3. E_R, expressed as an average peak electric field intensity, is then found from the product of the arrays:

$$E_R = [AF][V_{50}] \tag{5.14}$$

Figure 21 depicts the average peak electric field intensity calculated from Equation (5.14) and the data obtained from measurements with the receive antenna at 5 metre range. The average peak electric field intensity expressed as dBμV/m, is depicted for the three ovens evaluated.

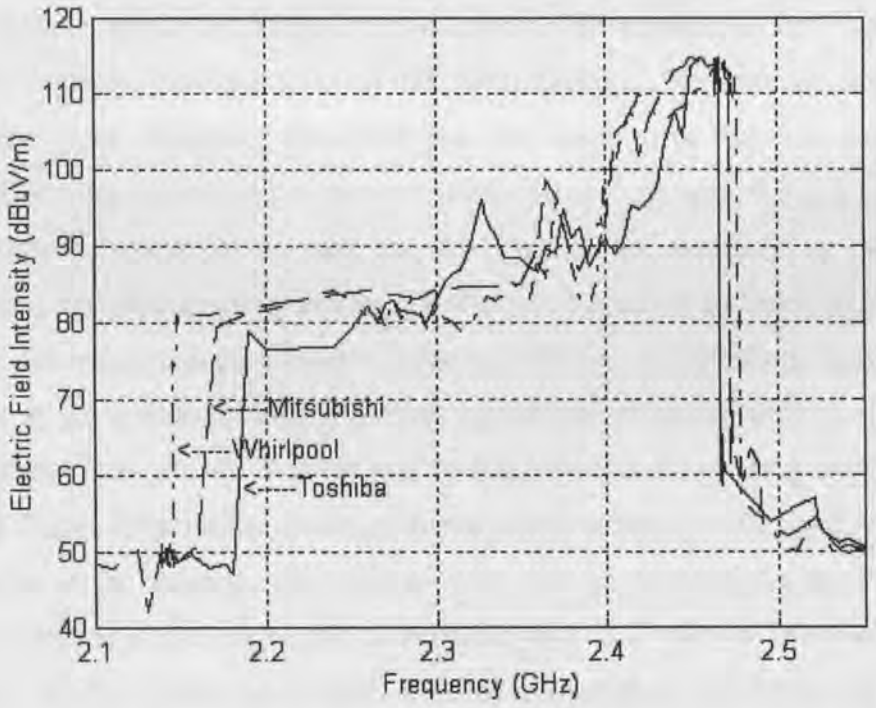

Figure 21: Average peak electric field intensity (E_R) produced by an operational microwave oven at 5 metre range.

5.3 The Magnetrons Influence on the Shape of the Peak Hold Plot

The upper and lower cut-off frequencies and general shape of the peak hold plots were found by measurement to be independent of the load placed into the operational microwave oven cooking cavity, or oven turntable rotation. Evaluation of data collected under no load (empty oven) with turntable enabled or disabled, and also through a variety of loaded (oven occupied) turntable enabled or disabled conditions produced the same cut-off frequencies and general shape. The test loads consisted of three containers each of varying size containing 0.5, 1.0, and 2.0 litres of water. For the three loads a measurable variation of 10 dB average fall in received power at the receive antenna for loaded measurements was observed at all frequencies depicted in Figure 20 when compared to measurements for unloaded operational ovens. This is attributed to microwave energy dissipation by the load, therefore reducing the amount of microwave energy available for production of RF currents in the ovens metallic external housing, and the level of RF oven leakage. The overall shape of the amplitude versus frequency peak hold plot was found to be the same regardless of oven cavity load. A reason for this amplitude versus frequency shape is given in the diagrammatical plots often used to show magnetron performance, the typical magnetron performance diagrams for our Whirlpool oven are shown as Figures 22, 23 and 24. The magnetron performance diagram of Figure 22 depicts the Average Anode Current as the abscissa which is plotted against two measured ordinate parameters, these being, Peak Anode Voltage and Average Output Power (P_0) using the same scaling. Figure 23 plots the Average Output power as the ordinate against Frequency (f) shown as the abscissa. From Figure 22 it can be seen that as the Peak Anode Voltage applied to the magnetron is increased from 300 volts to 1820 volts then the Average Anode Current is increased from 20 milliamps to 122 milliamps. Over this voltage and associated current range the magnetron frequency changes from 2147.7 MHz to 2475.6 MHz. This frequency change is in agreement with that plotted in Figure 17 for the same voltage and frequency ranges.

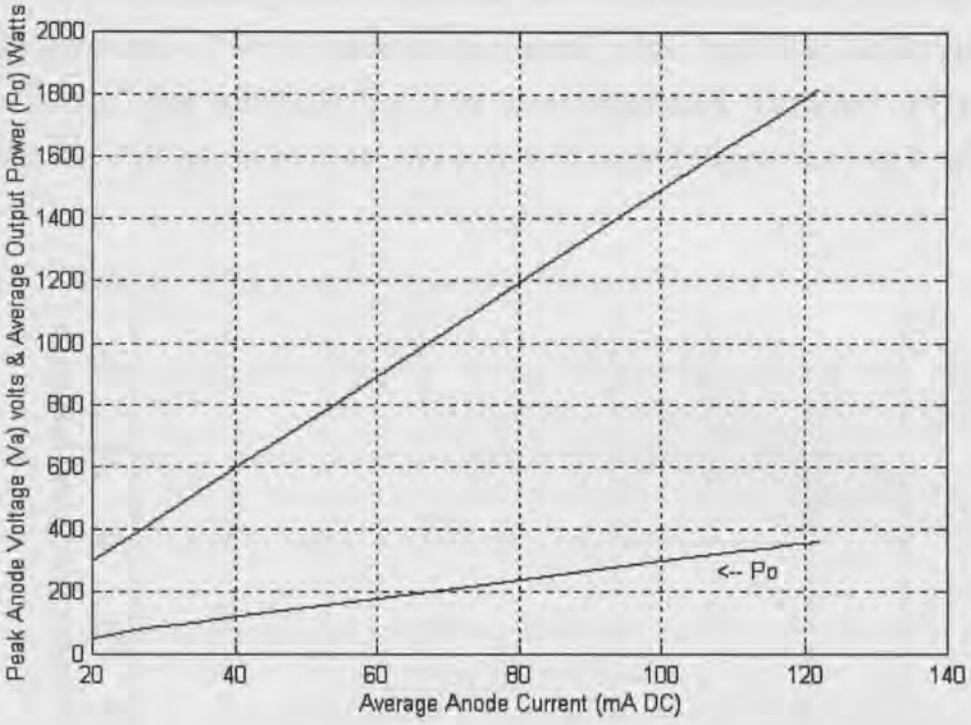

Figure 22: Magnetron Performance Diagram for V_a , P_0 , and Average Anode Current (Whirlpool Microwave Oven)

Of particular interest is the change in P_0 of the magnetron and its relationship with operating frequency. Our measurements for the Whirlpool magnetron output power into the oven cavity are plotted in Figure 23. Measurements revealed that as the peak anode voltage was increased from zero volts to a 300v the first significant oscillation occurred at frequency 2147.7 MHz, the average anode current at this value was 20 milliamps and the average measured output power P_0 was 50 watts. At a peak anode voltage of 1820 volts the maximum frequency of 2475.6 MHz was measured, and further increase in anode voltage caused no increase in operating frequency. Further increase in anode voltage did increase the average anode current and magnetron power output up to a maximum of 800 watts as depicted in Figure 24, with no additional increase in frequency. The 2475.6 MHz value being the magnetron upper cut-off frequency for the Whirlpool oven previously identified by measurement and plotted in Figure 18. The magnetron power frequency relationship is therefore one factor that influences the shape of the average peak electric field intensity measured at five-metre range as depicted in Figure 21. Because the magnetron output power

delivered to the cooking cavity of the oven varies with frequency as shown in Figure 23, by deduction a lower magnetron output power at the lower frequencies produces lower average peak field intensities at the lower frequencies. The shape of Figure 21 reflects this with the measured average peak field intensity increasing with frequency.

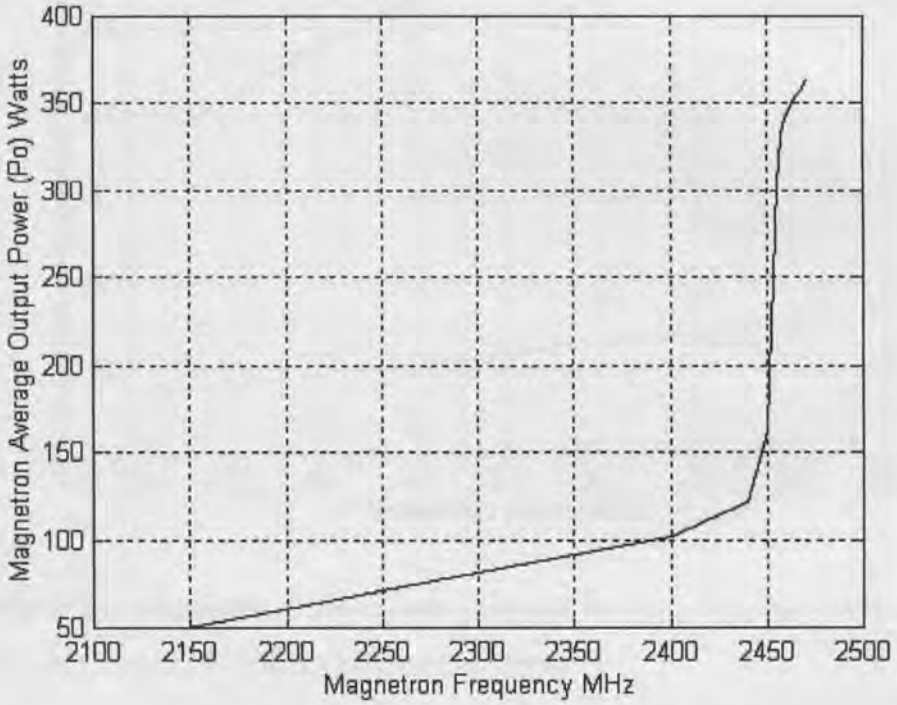

Figure 23: Magnetron Performance Diagram for P_0 and Magnetron Frequency (Whirlpool Microwave Oven)

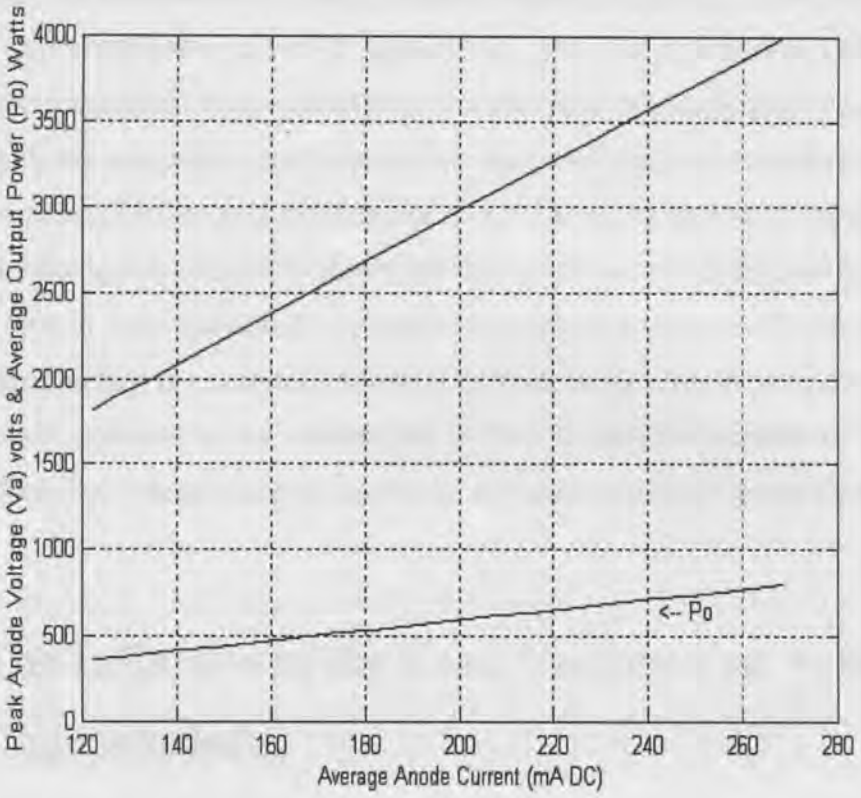

Figure 24: Magnetron Performance Diagram for V_a , P_0 , and Average Anode Current (Whirlpool Microwave Oven)

Another factor that is difficult to quantify is the gain frequency performance of the microwave oven when it is considered as a radiating antenna. As previously noted our measurements in the far field showed no clear E-field polarisation dependency for the microwave oven acting as a radiating antenna. It is postulated that the gain frequency performance of the microwave oven acting as an antenna is related to its dimensions and other structural factors that influence RF leakage. As with all antennae the gain is related to frequency and hence wavelength and resonance. With the significant frequency variation of the magnetron as measured and plotted in performance diagrams (Whirlpool oven shown in Figure 23) gain variation is also expected. Quantification of the gain/frequency characteristics for microwave ovens acting as antennae using statistical analysis of measurement data is a difficult exercise and predicably would vary considerably for ovens of different manufacture. The plots shown as Figures 20 and 21 represent the overall gain / frequency performance of the magnetrons and associated oven structures acting as antennae for three specific

models from three different oven manufacturers. Figures 20 and 21 clearly display the measured upper and lower cut-off frequencies as previously determined which are related to the magnetron. Also evident is the overall gain frequency shape, which is a result of both the magnetron power/frequency response and the performance of the oven structure itself acting as a radiating antenna. The results do not reveal a smooth curve of increasing received RF field strength level with increasing frequency, and the peaks and dips in the responses are related to the gain/frequency performance of the oven structures acting as antennae. Follow up measurements were performed at a later time to further substantiate the consistency of results, and the analysis of the data gathered from these measurements replicated the same statistical plots for all three ovens.

5.4 The Influence of the Load Variance on Noise Characteristics

Reference [75] notes that the noise characteristics of the electromagnetic radiation from an operational microwave oven vary with roughly the 12 second rotational period of the oven turntable. From our previous analysis of measurement data for operational ovens with the turntable firstly enabled and then disabled (for three different oven load conditions) we noted that both the upper and lower cut-off frequencies were unaltered. The nature of the load and its rotational influence do not cause the frequency of operation of the magnetron to extend beyond the identified range bounded by the upper and lower cut-off frequencies. The qualitative description and equations developed in Section 5.1 reveal that the dimensions of the magnetron and the anode to cathode voltage applied govern the frequency of operation. The operational frequency is from this analysis predicted as stable if the anode to cathode voltage is maintained constant during the 10 millisecond "on" period, and is defined by manufacturers as the operational frequency of the oven. However, the analysis of data gathered during measurements has shown that the rotation of the load within the microwave oven produces a variation to the standing wave ratio at the output of the magnetron, which results in a variation to the magnetron power output with frequency of operation. A plot of how the power output varies with frequency of operation under

various load conditions is provided by microwave oven manufactures and is termed a "Rieke" diagram. A Rieke diagram is essentially a Smith Chart with the VSWR circles drawn in, while the reactance circles are omitted. The change in operating frequency for a given change in standing wave ratio at the output of the magnetron is obtained from the Rieke diagram. Figure 25 is a Rieke diagram for the Whirlpool oven produced by measurement data for a range of VSWR values. From the Rieke diagram a "pushing" and "pulling" of the nominal magnetron operational frequency can be seen for changes in VSWR with load impedance variation for a given output power. Frequency variation of up to 15 MHz is common when the VSWR varies due to turntable rotational affects on the electrical load as seen by the operational magnetron. The result is a second order of statistical variance for the frequency being radiated by operational microwave ovens. Measurement data has shown that the rate of frequency change is directly related to the rotational velocity of the turntable, and the range of the frequency change is related to the nature of load within the oven cavity. The largest frequency variation of ±15 MHz with respect to nominal operating frequency was measured over a 12 second rotational period for no-load (oven cavity empty) conditions with the oven at full power. Measurements with test loads of no-load, and a container filled with 2.0 litres of water provided data for determining the frequency drift statistics for our three microwave ovens. The statistics for loaded operational ovens are depicted in Figures 26-28 and provide an estimate of the total time the operating frequency is located within any nominal 10 MHz bin expressed as a percentage value. The percentage value is computed from data gathered over a full 12 second turntable rotation period and represents an average of 50 such periods. The data is for the 10 millisecond "on" pulse time period at stable anode voltage and maximum power. It is of note that the same container filled with 0.5 litres and 1 litre respectively, gave statistically the same results as for 2 litres, and that the maximum frequency variation with respect to the nominal operational frequency occurred for all load values inclusive of no-load. The statistics for operational ovens with no-load are presented in Figures 29-31.

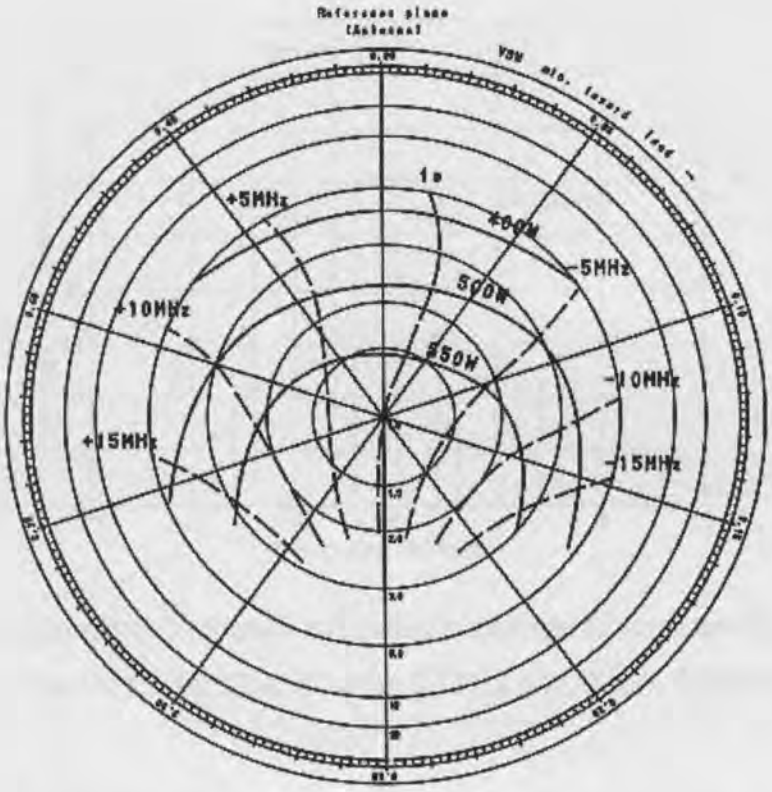

Figure 25: Rieke Diagram (Whirlpool Microwave Oven)

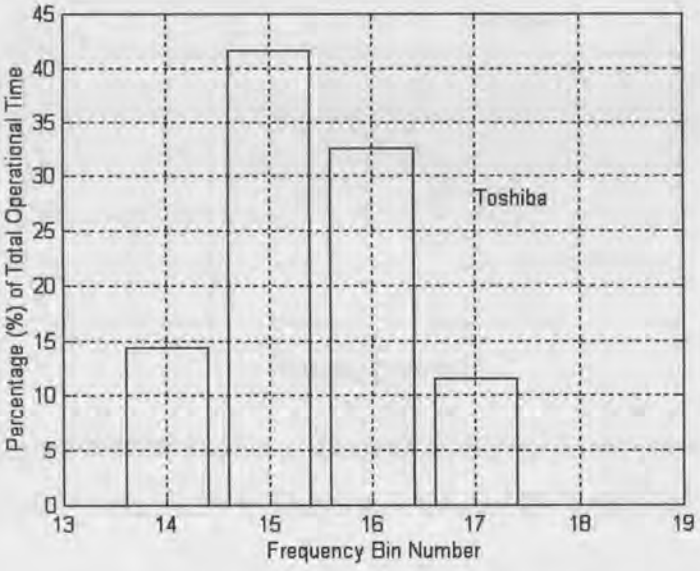

Figure 26: Frequency Drift Statistics (Loaded Toshiba Microwave Oven). Centre frequencies of bin 14, 15, 16 & 17 being 2.435, 2.445, 2.455 & 2.465 GHz.

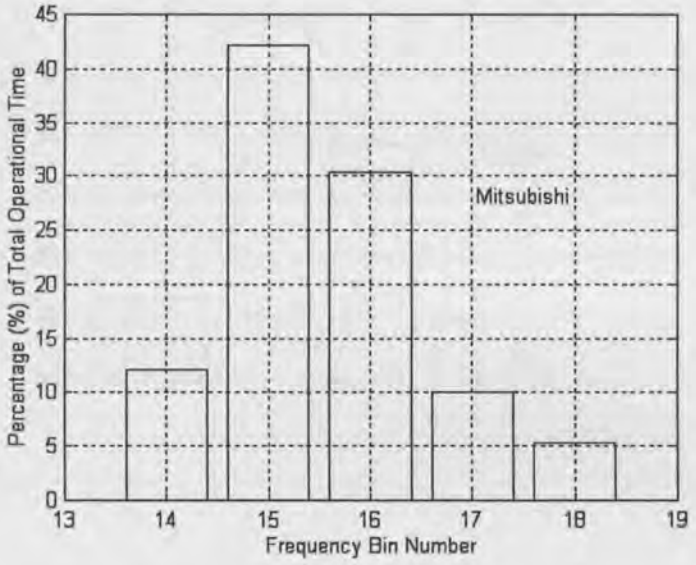

Figure 27: Frequency Drift Statistics (Loaded Mitsubishi Microwave Oven). Centre frequencies of bin 14, 15, 16, 17 & 18 being 2.435, 2.445, 2.455, 2.465 & 2.475 GHz.

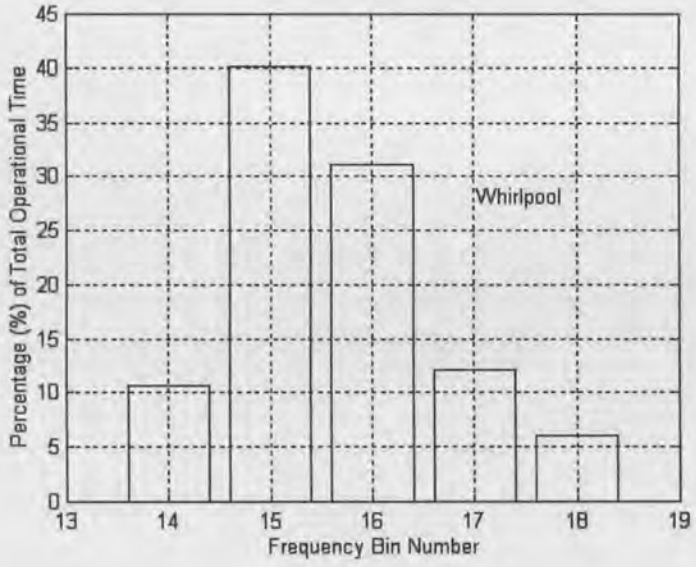

Figure 28: Frequency Drift Statistics (Loaded Whirlpool Microwave Oven). Centre frequencies of bin 14, 15, 16, 17 & 18 being 2.435, 2.445, 2.455, 2.465 & 2.475 GHz.

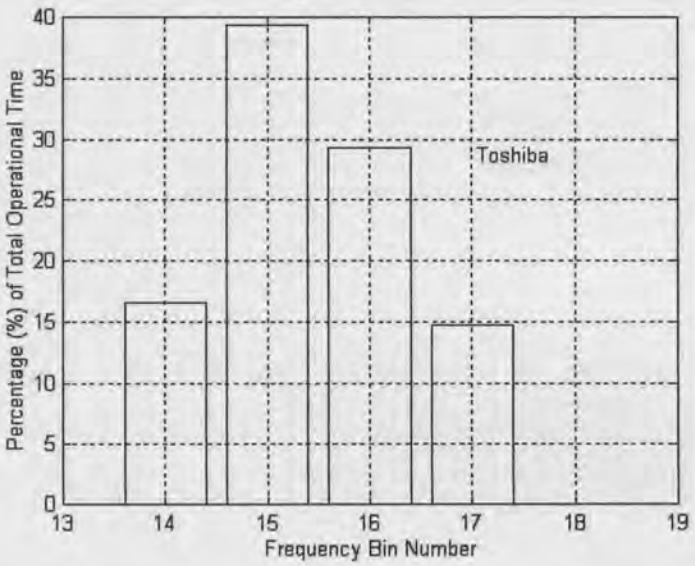

Figure 29: Frequency Drift Statistics (Non-loaded Toshiba Microwave Oven). Centre frequencies of bin 14, 15, 16 & 17 being 2.435, 2.445, 2.455 & 2.465 GHz.

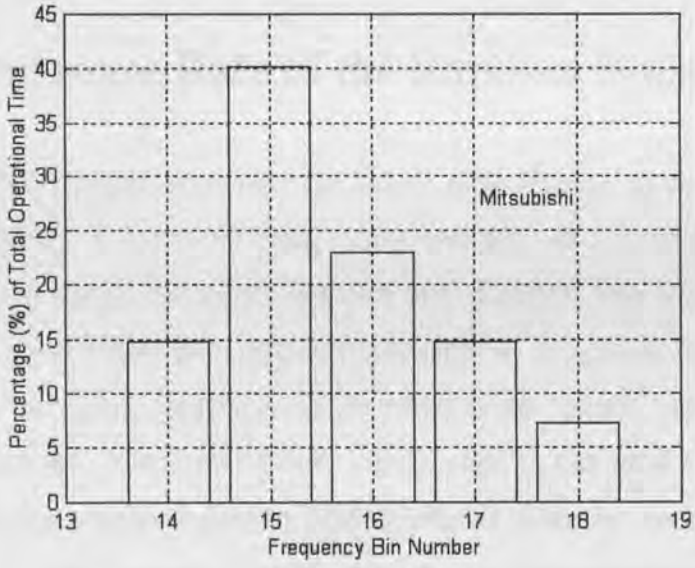

Figure 30: Frequency Drift Statistics (Non-loaded Mitsubishi Microwave Oven). Centre frequencies of bin 14, 15, 16, 17 & 18 being 2.435, 2.445, 2.455, 2.465 & 2.475 GHz.

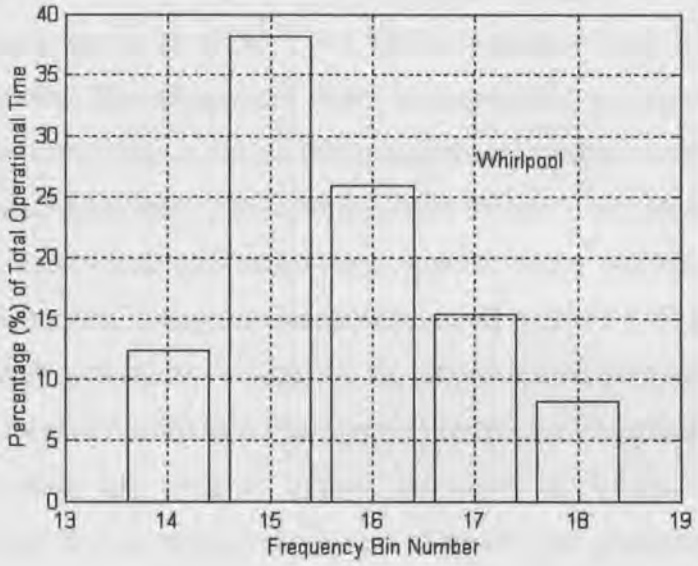

Figure 31: Frequency Drift Statistics (Non-loaded Whirlpool Microwave Oven). Centre frequencies of bin 14, 15, 16, 17 & 18 being 2.435, 2.445, 2.455, 2.465 & 2.475 GHz.

5.5 Occurrence Rate of the Random Noise Bursts

The BER for data transmissions over the indoor radio channel is not only dependent on the magnitude of any interfering non-systematic noise bursts, but also the occurrence rate of these noise bursts and their time duration. Reference [75] identified two groups of noise pulses one synchronised with the AC power line, and the other related to the switching frequency of switched mode power supplies sometimes employed where the transformer power supply type is not used. The noise in the 1.9 GHz band of interest evaluated by [75] "is related to the fast switching (≅ 30 kHz) of the power supply". As the 1.9 GHz band is not investigated for noise sources within this thesis the noise phenomena attributed to the switched mode power supplies in some microwave ovens is not evaluated. It has been shown by measurement [75] that a period "of strong emissions of second harmonics coincide with that of the main oscillation". The harmonics were detected in the range of 4.75-4.94 GHz and were approximately 45 dB below the values for the main 2.4 GHz band. The 4.75-4.95 GHz frequency band is not investigated in this thesis.

An estimate of the occurrence rate of the random noise bursts produced by an operational microwave oven in the 2.3–2.5 GHz frequency band has been obtained from measurements. The analysis of these measurements provided a count of the number of noise bursts that exceeded the measurement system sensitivity for each of our twenty measurement bins. The noise has been shown to be sinusoidal and have a frequency that varies with the magnetrons applied anode voltage, as depicted in Figure 17. The sudden change of magnetron anode voltage (0V to 800V in 0.45 milliseconds) with a resulting change to the magnetrons operational frequency of 300 MHz over this 0.45 millisecond time period causes the measured electromagnetic noise radiated from the oven to appear impulsive in nature. A measurement bandwidth of 100 kHz as employed for measurement data gathered for analysis in reference [75] proved by analysis against measurement data gathered with larger resolution bandwidth to be sufficient as to not reduce the power level of the measurement values. This bandwidth was selected to allow for the shortest spectrum analyser sweep time of 20 milliseconds. To further verify the sinusoidal nature of the non-systematic noise bursts produced by operational microwave ovens, a series of measurements were completed with the measurement instrumentation depicted in Figure 6. The measurement laboratory shown as Figure 40 was selected as the indoor channel most suitable for gathering data of this form. Measurement analysis of radio waves propagating between the transmit and receive antennae located within this particular laboratory venue has quantified the variation of the received power local mean for the "temporally static" situation at less than ±0.2 dB (Section 6.3). To achieve this temporally static situation the motion of people and any other animate or inanimate objects within the laboratory is kept at zero. The motion of objects such as people and motor vehicles located external to the laboratory had no measurable affect on the local mean receive power level for the temporally static situation. This is attributed to the fact that the laboratory is without windows, which generally offer low attenuation entry and exit points for radio waves, and is constructed primarily from materials that offer high attenuation to radio waves that propagate at gigahertz frequencies, thus reducing the affect of external temporal variations to an insignificant level. A temporally static measurement situation is of importance because any variation in the value of the received average modulating signal power produces a

variation to the EVM as given in Figure 10. The primary purpose of checking that the EVM value corresponds to the expected value for the average modulating signal power being received over the test link is to permit identification of non-systematic noise entering the link by way of the receive antenna. This non-systematic noise may be identified by an increase in both peak and rms EVM value. The cyclic transmission of 600 symbols (1200 data bits for 2 bits/symbol) at a rate of 4 megasymbols/second using QPSK modulation (raised cosine filtering $\alpha = 0.5$) was selected for the measurements. This format was one that had previously been chosen to establish our calibration datum for the systematic noise and its associated EVM (Figure 10). The receive antenna for each measurement bin was again the calibrated resonant 1/4 λ monopole situated at a range of 5 metres from the operational microwave oven. Each of the calibration measurements was completed prior to gathering measurement statistics for data transmission in the presence of the non-systematic noise bursts produced by the operational microwave oven. The EVM measurements were performed as before for each of the twenty frequency bins. A carrier frequency equal to each bin centre was QPSK modulated by a 1200 bit cyclic pseudo-random data sequence, and then transmitted over the indoor radio channel. For each measurement time period the microwave oven was in continuous operation at full power. To further reduce measurement error the transmit power was set to provide a received average modulating signal power of -45 dBm in the absence noise from the microwave oven, with care taken to maintain the temporally static situation for the indoor channel. As can be seen from Figure 10 the selection of -45 dBm minimises the affect of small variations in received average modulating signal power, and as a consequence maintains the average received signal to systematic noise power ratio, and the associated EVM relatively constant. Therefore the EVM value obtained by measurement for the static situation, and in the absence of noise bursts from the microwave oven, is simply the value attributed to the systematic noise (Section 4.1.1). A measured rms value of 4.1048 % EVM was obtained for a received average modulating signal power of –45 dBm, and this value is considered as wholly caused by systematic noise generated within our measurement system itself. Of particular note is the value of the peak value of EVM (9.1065 %) as this is representative of the peak value of received noise. Figure 32 presents the data associated with the

systematic noise measurement, it also shows the display format provided by the measurement instrumentation and it is applicable to all our measurements. The format includes the received data constellation picture, eye pattern, error table, and spectrum.

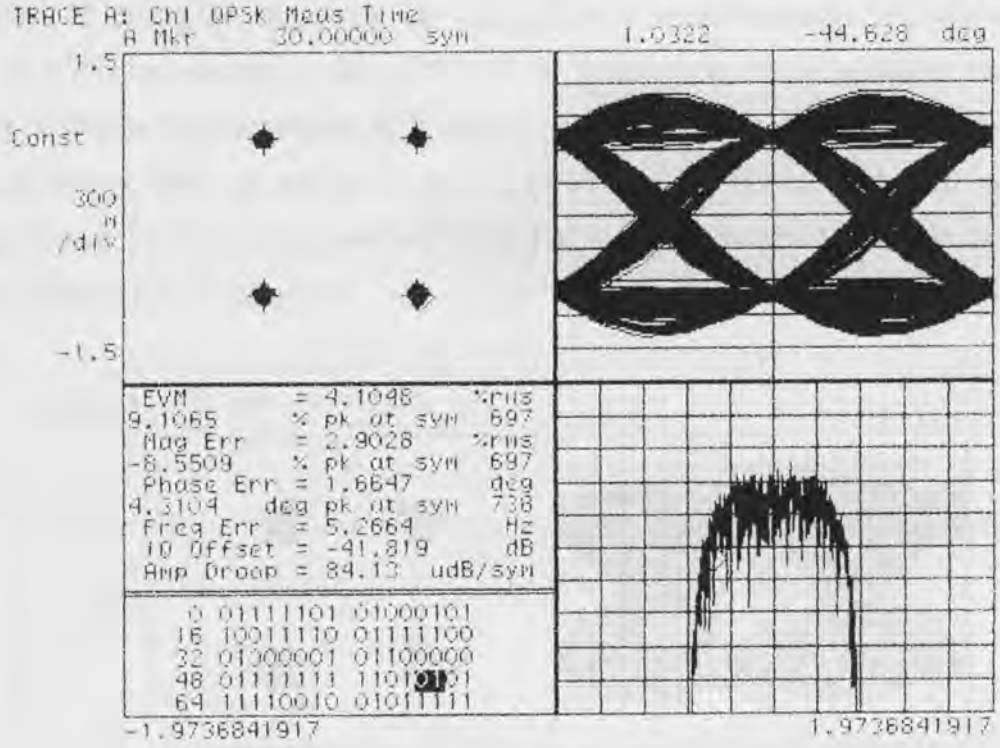

Figure 32: Measurement of EVM for systematic noise (receive antenna :- resonant 1/4 λ monopole at range 5 metres from the microwave oven).

Figure 33 presents the measurement data obtained in the presence of noise bursts from the Toshiba operational microwave oven for frequency bin number 15 (2.44-2.45 GHz). It is representative of a series of measurements completed with the aim of characterising the nature and intensity of the noise. As can be seen from the data in Figure 33 the magnitude of the received power spectrum approximates that of the calibration datum of Figure 32 for the estimation of the systematic noise EVM value, however the value of EVM has now increased significantly to a rms value of 16.583 %. The spread of decoded QPSK data points in the constellation is also seen to be relatively uniform for each quadrant, however a grouping of decoded symbol signal points into four clusters around the optimum decode point for each quadrant is evident. Also the degradation in eye pattern is evident as compared to the calibration

eye pattern shown in Figure 32. The random nature of the noise bursts is dependent on rate, duration, and intensity. For frequency bin number 15 as we have determined from the analysis of previous data both the rate and intensity are near maximum with the frequency drift statistics showing typically a 40 % occupancy of frequency bin number 15 during the magnetron "on" time period of 10 milliseconds. The peak value of the EVM has reached a value of 52.041 %, which is significantly higher than our peak EVM calibration datum of 9.1065 %. Peak EVM is a statistic used for the calculation of BER probability of data received with the presence of noise and or interference, it represents a measured value that is directly related to the erfc variable of Equation (7.5) in Chapter 7.

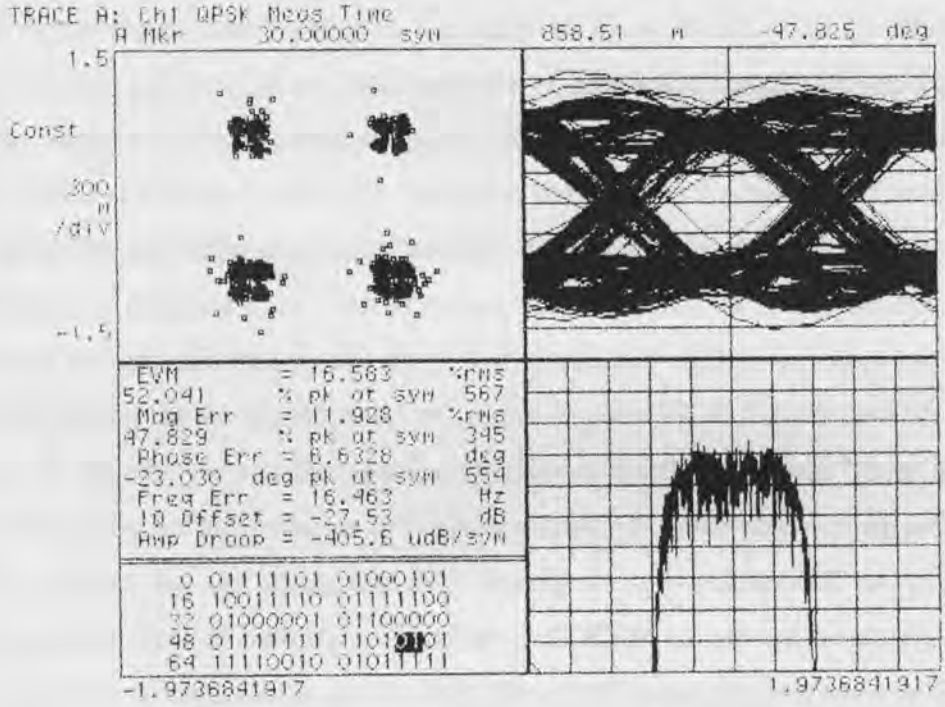

Figure 33: Measurement data obtained in the presence of noise bursts from the Toshiba operational microwave oven for frequency bin number 15 (2.44-2.45 GHz, receive antenna :- resonant 1/4 λ monopole at range 5 metres from the microwave oven).

5.6 Sinusoidal Tone Interference

The nature of the sinusoidal tone interference produced by an operational microwave oven has been discussed in the preceding sections, from our analysis of measured data a detailed picture of why some frequency bins suffer greater interference than others has emerged. The magnetron performance diagram for the Whirlpool oven that is shown as Figure 23 is typical of the other ovens evaluated. It reveals that a magnetron output power of less than 100 watts is typical at frequencies below approximately 2400 MHz and that a significant increase does not occur in output power until frequencies above 2450 MHz are reached. Additionally the frequency drift statistics show that for the 10 millisecond "on" period of the magnetron there are no emissions in the measurement bins numbering 1 through to 13, or bins 19 and 20. These bins being affected only during the rapid increase of magnetron anode voltage on power up, and decrease of the voltage on power down either side of the "on" pulse.. The nature of the interference is directly related to the nominal frequency and intensity of the sinusoidal tone. The transient sinusoidal interference during rapid anode voltage change occurs as stated in all bins. However bins 1-13, 19, and 20 for the three ovens evaluated are not affected by the magnetron frequency drift that occurs with SWR variation during the 10 millisecond "on" pulse. Figures 34-36 depicts data for bins 4, 8, and 11 respectively and the Toshiba operational microwave oven. These bins are only affected by the rapid change of frequency during magnetron power up and power down, and not by the frequency drift during the 10 millisecond on period. A progressive increase in both the rms and the peak EVM values can be clearly seen as the magnetron voltage, output power, and operational frequency increases with higher bin numbers. For bin numbers 4, 8, and 11 a study of the error table associated with the Figures 34-36 reveal that no data bits were received in error at the signal to noise ratio set for the measurement system for the 5 metre test distance from the operational microwave oven. This is expected as from Figure 20 the average measured power level of random noise bursts at range 5 metres for the Toshiba oven are typically less than –45 dBm, our chosen average receive power level for system calibration. The power levels of the random noise bursts increase suddenly at frequencies corresponding to measurement bin number 12 (2.41-2.42 GHz) and are of significant

levels above this bin frequency range up to and including the upper magnetron cut-off frequency shown in Figure 18. The peak EVM value measured for bins 4, 8, and 11, were respectively, 12.676 %, 13.768 %, and 25.983 %.

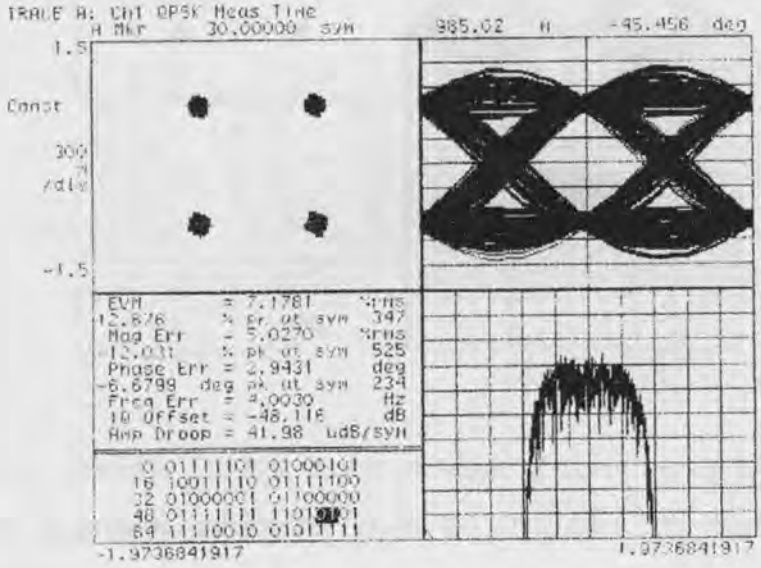

Figure 34: Measurement data in the presence of noise bursts from the Toshiba operational microwave oven for frequency bin number 4 (2.33-2.34 GHz, receive antenna :- resonant 1/4 λ monopole at range 5 metres from the microwave oven).

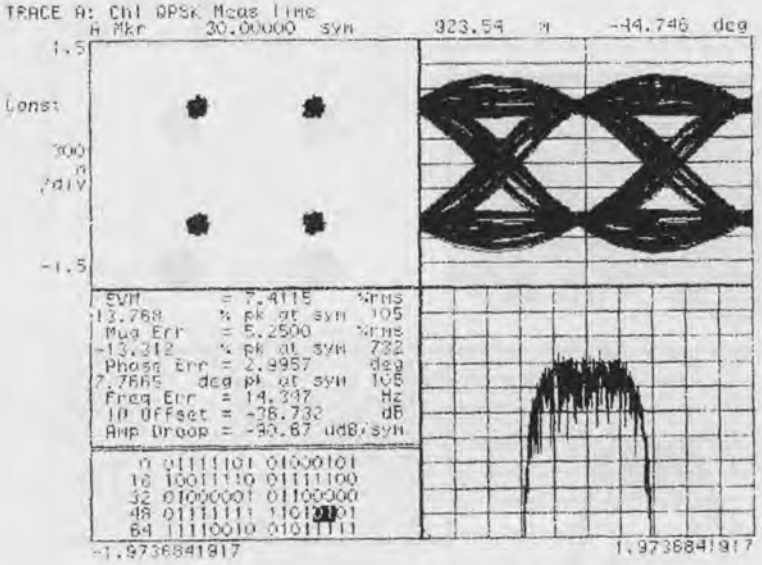

Figure 35: Measurement data in the presence of noise bursts from the Toshiba operational microwave oven for frequency bin number 8 (2.37-2.38 GHz, receive antenna :- resonant 1/4 λ monopole at range 5 metres from the microwave oven).

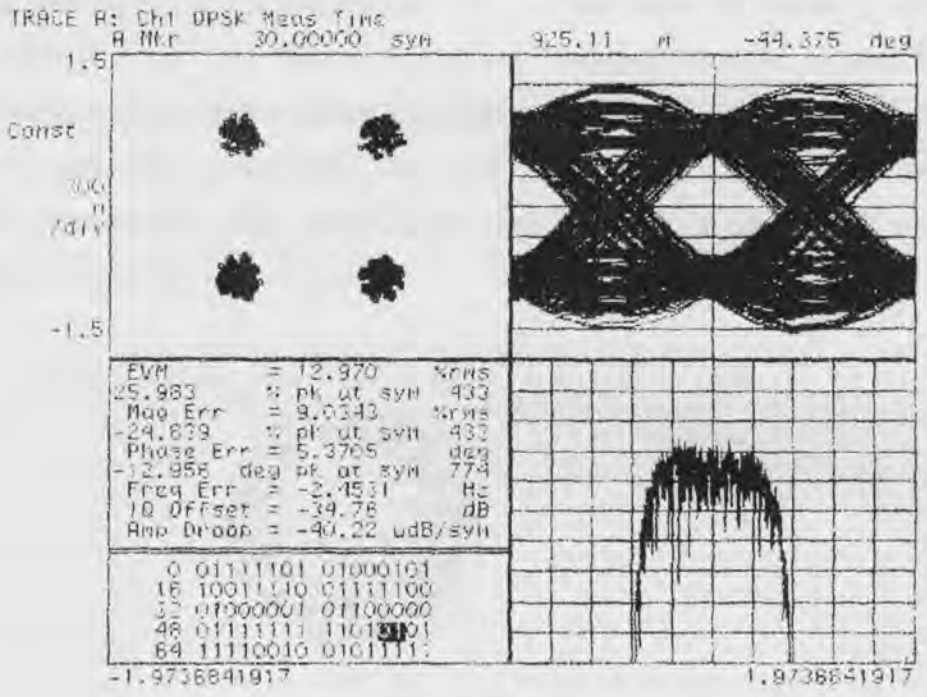

Figure 36: Measurement data in the presence of noise bursts from the Toshiba operational microwave oven for frequency bin number 11 (2.40-2.41 GHz, receive antenna :- resonant 1/4 λ monopole at range 5 metres from the microwave oven).

Sinusoidal tone interference can result in extremely high error rates for data transmitted and received over the test link. The interference can create circles, or dependent on the time duration of the interference partial circles in the received constellation. The sinusoidal interferer generates this circular shape due to the rotating vector of the interference signal, which is frequency offset from the digital radio carrier frequency. This was observed for the frequency bin numbers 14-18 when the received power of the interference sinusoid (generated from the operational microwave oven) exceeded the average received power level for the data transmission test link. Figure 37 shows a measurement result for bin 16 with the Whirlpool microwave oven operating, and the same data sequence being transmitted as for Figures 34, 35, and 36. The interfering sinusoid causes all received data symbols to be decoded in the top left quadrant of the received constellation, therefore all received symbols are decoded as the two data bits 10. The received data bit stream is a sequence 101010101010... for the time duration that the interference frequency is

stable at this particular spectral position. As we have seen the magnetron has two factors affecting the time that an interfering frequency remains in any spectral position, one being the anode voltage variation applied to the magnetron, the other the frequency drift with varying SWR. Due to the rotating vector of the sinusoidal tone interferer the received data constellation often takes on a 'doughnut" shape as depicted in Figure 37.

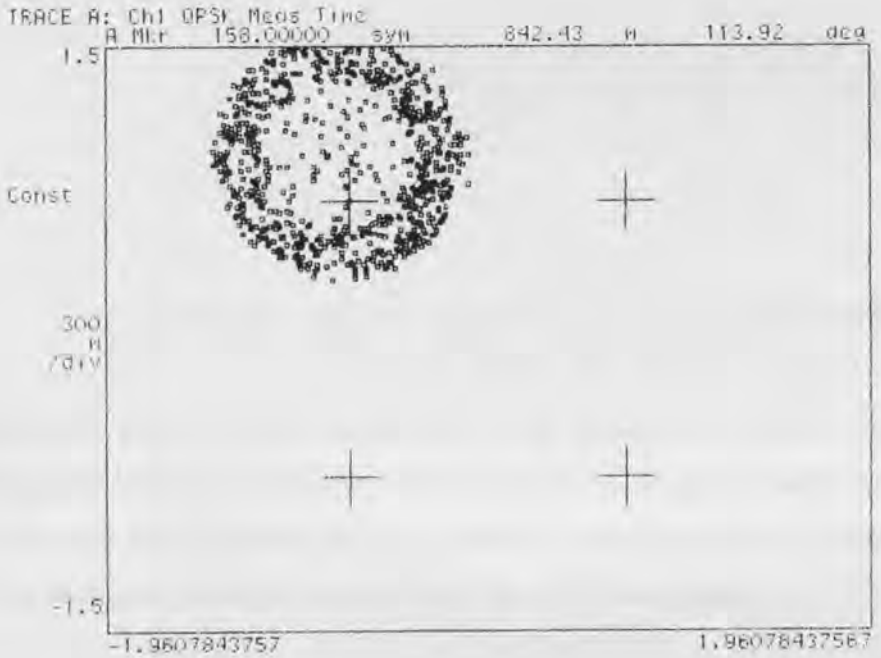

Figure 37: Received data constellation in the presence of an interfering sinusoidal tone generated from a Whirlpool operational microwave oven for frequency bin number 16 (2.45-2.46 GHz, receive antenna :- resonant 1/4 λ monopole at range 5 metres from the microwave oven).

Figure 38 provides another example of where the received data is concentrated into a cluster in the shape of a partial circle within the constellation with the symbol 00 dominating the decoded result with 576 symbols each representing 00 data bits decoded. Additionally 24 symbols each representing 10 data bits were decoded. The interfering sinusoidal noise in this case occurred in measurement bin number 15 with the Mitsubishi oven operating.

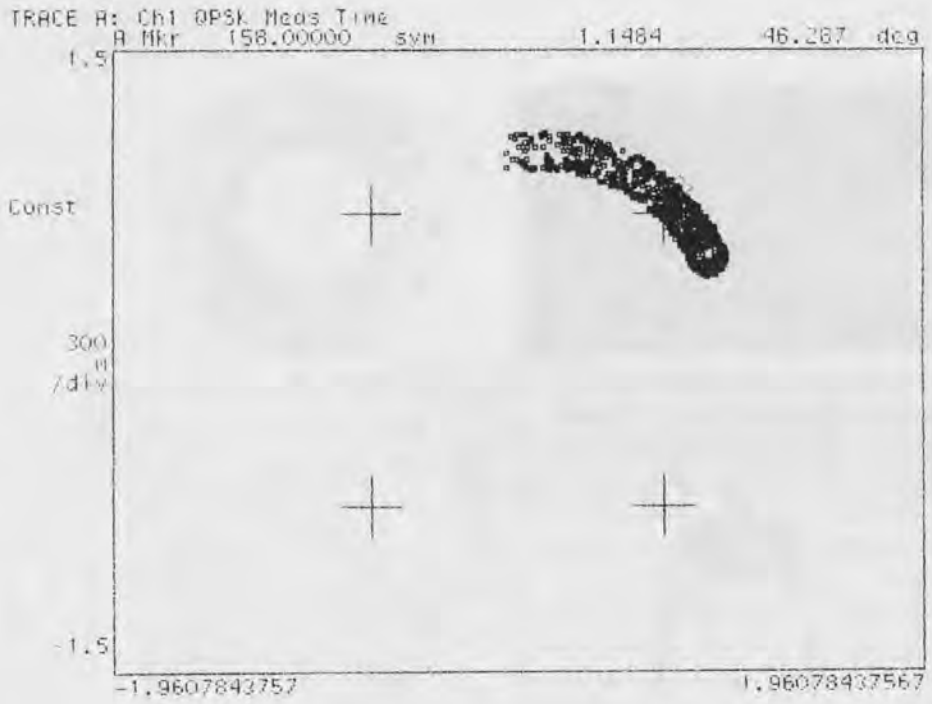

Figure 38: Received data constellation in the presence of an interfering sinusoidal tone generated from a Mitsubishi operational microwave oven for frequency bin number 15 (2.44-2.45 GHz, receive antenna :- resonant 1/4 λ monopole at range 5 metres from the microwave oven).

Figure 39 shows a measured constellation that in the presence of an interfering sinusoid takes the form of a complete circle, each symbol having approximately equal probability of occurrence, but not necessarily in their correct constellational positions. The measurement was for bin number 17 and the Mitsubishi oven operational.

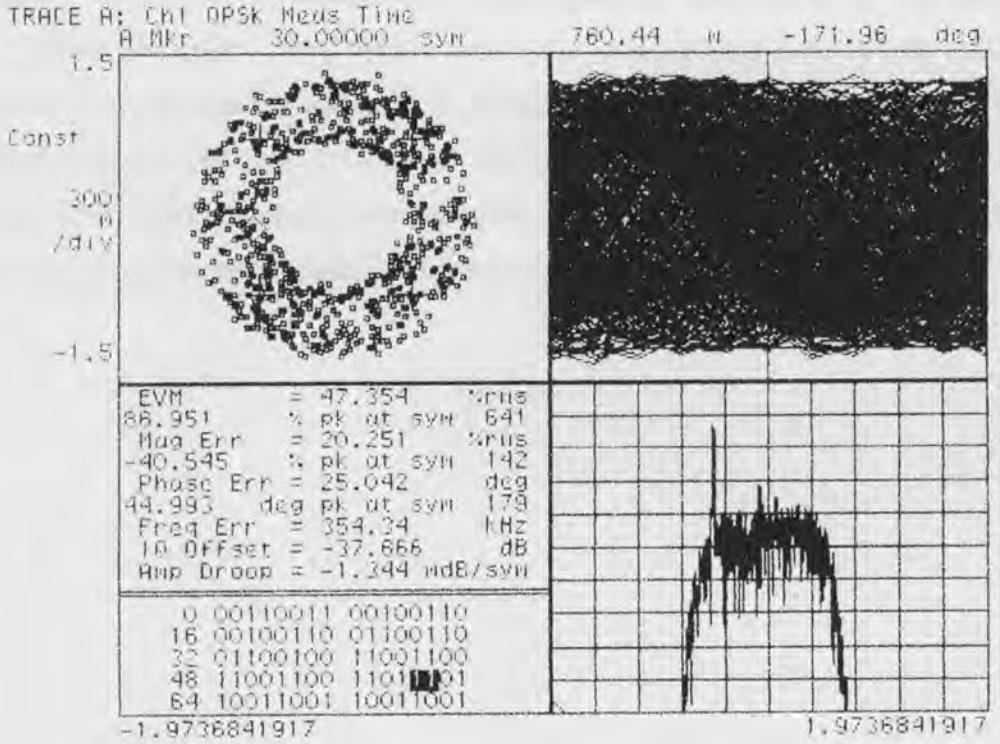

Figure 39: Received data constellation in the presence of an interfering sinusoidal tone generated from a Mitsubishi operational microwave oven for frequency bin number 17 (2.46-2.47 GHz, receive antenna :- resonant 1/4 λ monopole at range 5 metres from the microwave oven).

5.7 Conclusions

The noise generated in the 2.3-2.5 GHz band by operational microwave ovens can cause significant interference to communications systems intercepting this noise via their receiving antenna and degrade the BER performance of data transmitted over the link. The BER performance of such systems (including our measurement system) in the presence of noise generated by operational microwave ovens will vary. The BER has been shown to be dependent on the selection of carrier frequency for the communications system (level of noise and duration differs for our 20 bin numbers evaluated). The bandwidth occupied by the data transmitted over the system is therefore also significant, as is the received signal level of the carrier signal for the communications system, and the systems bit error rate floor characteristics. To further

estimate the BER performance of communications systems in the presence of interference from operational microwave oven a series of experiments with our three microwave ovens and the test instrumentation shown in Figure 6 would advance the understanding in this area. To this end, the results of a completed set of experiments on the BER performance for data transmitted using QPSK digital modulation in the presence of microwave oven noise is presented in Chapter 7 of this thesis.

Chapter 6

Characterisation of Channel Fading

In this Chapter, we present fading measurements for the indoor radio propagation channel in the 2.4 GHz-ISM band where the controlled motion of one or more people was deliberately introduced to the channel. The motion introduced is considered typical of that encountered when personal communications systems are used in an indoor situation. The measurements are conducted in a typical laboratory environment, and the type of motion introduced to the channel was restricted to that of people moving around the receive antenna. Cumulative distribution functions (CDF), level crossing rates (LCR), and average duration of fades (ADF) are the statistics extracted from the measurements. The analysis of these statistics is undertaken and the obtained fading distributions, LCR's, and ADF's will be presented and discussed. The measurement system used to gather the fading data is shown as Figure 6 in Chapter 4, and a brief reference to the hardware used to extract the fading data for the indoor channel is undertaken in Section 4.1 of Chapter 4, this will be described in greater detail in Section 6.1 of this chapter.

6.1 Fading Measurement System

The Marconi TF2300A modulation analyser, Aphex VCA1001 voltage controlled attenuator (VCATT), and the personal computer (PC) fitted with a sampler card is used to record fading data for the indoor channel. The transmit and receive antennas used in all fading measurements are identical quarter wave omni-directional monopole antennas constructed for the frequency range 2.3-2.5 GHz. The antennas were mounted on separate identical non-metallic pipes of adjustable height from

1.0 to 2.5 m. The transmit antenna was set to a height of 2.5m, and the receive antenna to a height of 1.2m for all measurements. These height settings being chosen to best simulate a base station transmit antenna communicating with a portable unit. All measurement equipment is accommodated on a movable steel trolley as shown in Figure 7. The fading data were obtained from the over-sampled 100 Hz amplitude modulated carrier by the use of software rectification to extract the positive half cycles. Then, a fifth order Butterworth low pass filter was applied to this rectified signal to remove all frequency components above 40 Hz. The cut-off frequency of 40 Hz was selected to ensure that any 50 Hz AC power supply hum, and 100 Hz rectification hum generated within the measurement system itself was minimised.

6.2 Building Topology

Measurements were carried out at the Cooperative Research Centre for Broadband Telecommunications and Networking laboratory located at Curtin University of Technology, Perth, Australia. A plan view of the laboratory with the antenna positions used for the measurements is shown in Figure 40.

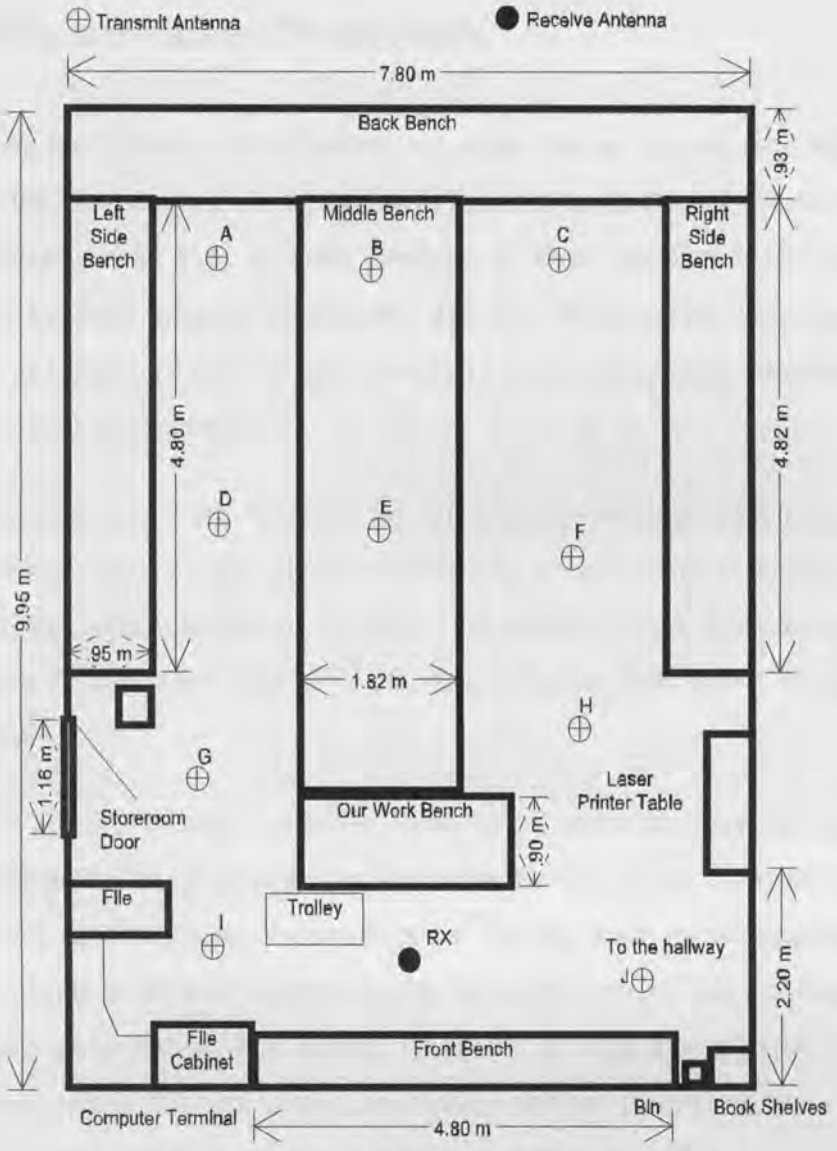

Figure 40: Plan view of the laboratory.

The laboratory has two doorways, no windows, and is rectangular of size 7.8 m by 9.95 m with a three metre ceiling. The ceiling is located 1.5 m below the concrete floor for the second storey of the four storey building. The laboratory has steel framed walls clad with plaster-glass, a dropped ceiling constructed with non-metallic acoustic tiles, and a carpeted concrete floor. This environment is one cluttered with test equipment on benches as shown in Figure 7.

6.3 Measurement Procedure

To determine the influence of movement by people, motor vehicles, and other objects external to the laboratory, a series of measurements were performed where the motion in the laboratory was kept at zero. Analysis of these measurements showed the variation of the local mean to be less than ±0.2 dB. Therefore, the local mean can be considered as influenced only by the controlled motion deliberately introduced as part of our measurement procedure.

Fading measurements were obtained for 10 different transmit antenna placements within the laboratory. For each placement and with no movement of people, the initial received signal level was set to –65 dBm. This receive level provided a signal to measurement system noise ratio of 35 dB, thus allowing fade depths of this order to be identified.

The receive antenna location remained fixed for all measurements and the transmit antenna was moved to a different location within the laboratory for a series of fading measurements each of twenty second duration. During these measurement periods, a number of people moved in a similar manner about the receive antenna only, keeping within a two metre radius. The number of people in motion was varied from three through to six people for each particular transmit antenna placement, and the average velocity estimated at 0.85 metres/second for each person in motion.

6.4 Measurement Results

From our set of measurements, four representative recordings will be considered in detail. Figures 41, 42, 43 and 44 display the short term envelope fading obtained for transmit antenna placements at positions C, J, D and F.

For C, J, and D antenna placements, similar motion of three people about the receive antenna was maintained for the full record period. Although the distance between transmit and receive antenna is relatively large for transmit position C with respect to J, only once did the fading envelope fall below the -9 dB level (Figure 41). For placement J the fading envelope depth fell below -9 dB on seven occasions, with three

of these fades being even lower than -21 dB (Figure 42). The fading obtained for transmit antenna placement D is shown in Figure 43 with the fading envelope depth going below the -21 dB level twice during the record period.

Figure 44 shows fading where six people moved about the receive antenna with the transmit antenna located at position F. The increased level of motion resulted in an increase in variance of fading amplitude about the mean. In addition, we observe frequent signal enhancements in the range of +5 dB to +9 dB, with the fading being more balanced about the mean.

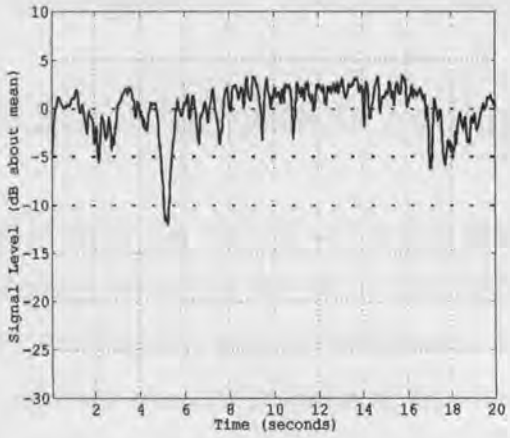

Figure 41: Fading for transmit position C, three people in motion.

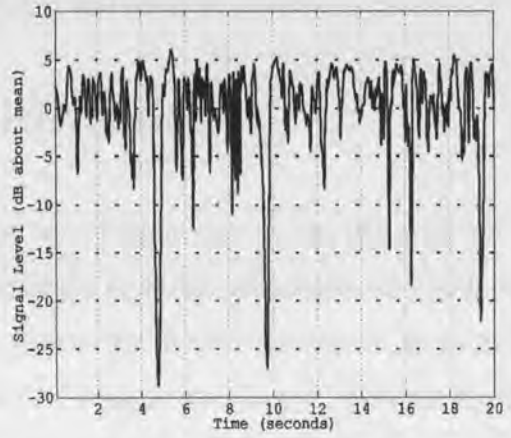

Figure 42: Fading for transmit position J, three people in motion.

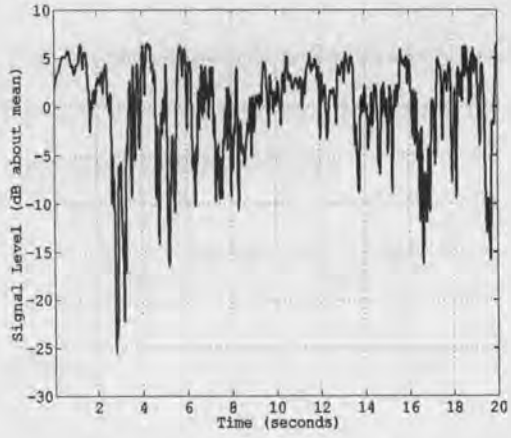

Figure 43: Fading for transmit position D, three people in motion.

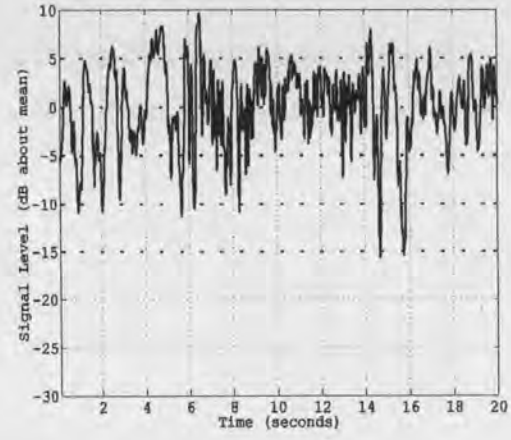

Figure 44: Fading for transmit position F, six people in motion.

6.5 Statistical Analysis

The statistical analysis of the channel fading data produces estimates for parameters such as LCR's, ADF's, and Rician k-factors. These estimates of the parameter values form part of the data variables which are input to specific mathematical equations that determine important transmission link performance indicators, such as the average BER expectation for data transmitted over the indoor radio propagation channel. A statistical analysis of the four representative recordings for short term envelope fading which are depicted in Figures 41, 42, 43, and 44 respectively as received signal level plotted against time, is presented in Section 6.5.1, and Section 6.5.2.

6.5.1 Amplitude Fading Distributions

If between the transmit and receive antenna a line of sight path exists, the probability density function of the fast varying amplitude of the received instantaneous signal can be described by a Rician distribution. Let A denote the direct waves peak amplitude, and σ the standard deviation of the overall received signal envelope R, then the Rician k-factor is given as [68]:

$$k = \frac{A^2}{2\sigma^2} \tag{6.1}$$

The Rician cumulative distribution function (CDF) is dependent on the value of k, and for $k = 0$ it degenerates into that of a Rayleigh distribution. The Rician CDF is calculated as follows [68]:

$$C_{Rice}(R) = 1 - \overline{C_{Rice}}(R) \tag{6.2}$$

where:

$$\overline{C_{Rice}}(R) = \exp\left(-k - \frac{R^2}{2\sigma^2}\right) \sum_{m=0}^{\infty} \left(\frac{\sigma\sqrt{2k}}{R}\right)^m I_m\left(\frac{R\sqrt{2k}}{\sigma}\right)$$

and $I_m(.)$ is the modified mth order Bessel-function of the first kind. Although the computation of the Rician CDF appears difficult because of the summation of an infinite number of terms, in practice the summation of m = 50 terms was sufficient to reduce the remaining terms contribution to a negligible level.

In calculating the empirical CDF, the measured data was classified into a number of bins B according to the formula [65]:

$$B = 1.87(S-1)^{2/5} \tag{6.3}$$

where S is the number of data samples obtained for 20 second measurement period. Then, a set of hypotheses for the Rician CDF with k = 0 to 15 in 0.1 increments were tested to match with the measured CDF where the power level is normalised about the root mean square (rms) value. We applied the Kolmogorov-Smirnov goodness-of-fit technique for testing the relevance of match between measured and hypothesis CDF. The maximum deviation between measured and hypothesis CDF over the considered normalised amplitude range was then used to indicate the significance of the match. Appendix D provides a listing of the computer program used for Rician k-factor testing. Table 2 shows the obtained k-factors. Note that we also performed curve fitting for the case where the CDF's are normalised about the median. The obtained k-factors are slightly higher but give the same ranking for the antenna placements shown in Table 2.

Table 2: Rician k-factor Laboratory Venue

Placement	k
C	8.7
J	2.0
D	2.0
F	1.3

The CDF's for fading measurements at C, J, D and F are depicted in Figures 45, 46, 47 and 48 respectively. Note that a Rayleigh CDF is depicted as well for comparison. The results indicate a dominant line-of-sight path for transmit antenna placement C (Figure 45) which has a k value of 8.7 for best fit. Placement J (Figure 46) exhibits a lower k value of 2.0 for similar motion of three people around the receive antenna. Placement D (Figure 47) also had a k value of 2.0. The fading data for transmit antenna placement F (Figure 48) provided the best fit for $k = 1.3$, which is approaching the Rayleigh distribution. A reduction in the effect of the line-of-sight path caused by the increased motion of six people about the receive antenna is thought to be the main factor for the low k value for this measurement. This reasoning is supported by the measurement at F for three people in motion where a higher value of $k = 3.1$ provided best fit. Although measured CDF's for placement C and F look similar at first sight, the different k values are mainly due to the CDF characteristic about the normalised 0 dB level. In this region the probability that the power level is less than the abscissa is in the range 10 % to 100 %. Therefore, the influence on the curve fit is more significant than that of the lower normalised power region. In the case of six people moving about the antenna, a match to a CDF other than the Rician distribution may be considered.

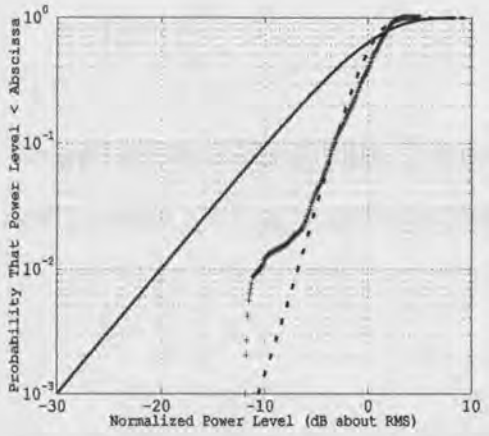

Figure 45: CDF for fading at C and three people.
+ measured, -- Rician k = 8.7,
solid : Rayleigh.

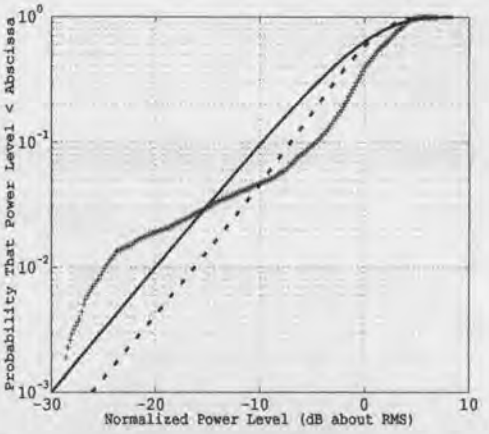

Figure 46: CDF for fading at J and three people.
+ measured, -- Rician k = 2.0,
solid : Rayleigh.

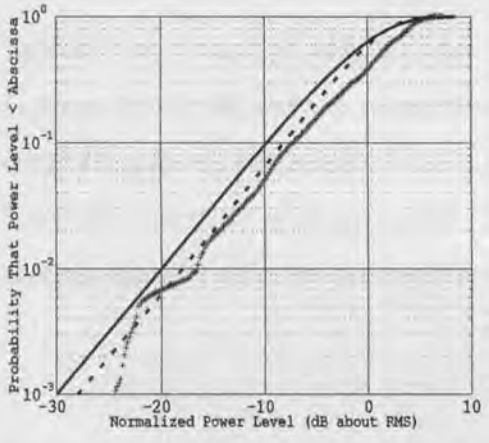

Figure 47: CDF for fading at D and three people.
+ measured, -- Rician k = 2.0,
solid : Rayleigh.

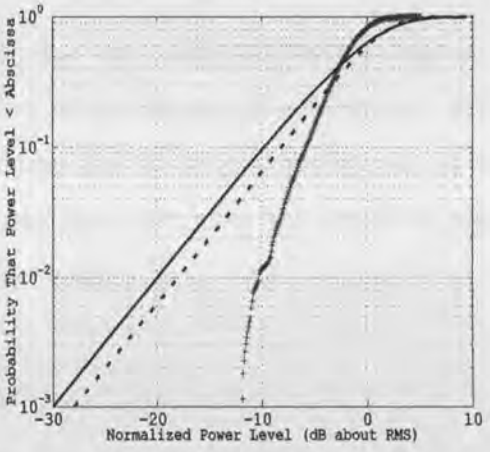

Figure 48: CDF for fading at F and six people.
+ measured, -- Rician k = 1.3,
solid : Rayleigh.

6.5.2 Fading Statistics

The level crossing rate N_L is defined as the expected rate at which the envelope crosses a specified signal level in the positive direction [66]. By counting all crossings N with a positive slope at a specified signal level L, and for a fading record of T_F seconds duration, the level crossing rate is given by:

$$N_L = \frac{N}{T_F} \tag{6.4}$$

The average duration of fades $\overline{t_L}$ is defined in [66] as the sum of N fades at level L, of time duration t_i for each individual fade, divided by N:

$$\overline{t_L} = \frac{1}{N}\sum_{i=1}^{N} t_i \tag{6.5}$$

Note that the product of Equations (6.4) and (6.5) gives the CDF as follows:

$$N_L\overline{t_L} = \frac{1}{T_F}\sum_{i=1}^{N} t_i = \text{Prob}(R \le L) \tag{6.6}$$

where normalisation is about the mean of the received signal level.

Tables 3, 4, 5 and 6, display the statistics for the fading envelopes shown in Figures 41, 42, 43 and 44 respectively. As far as the degree of motion as a fading controlling factor is concerned, the results indicate that the level crossing rates at level L = 0 dB increases with increased motion and simultaneously the levels at which crosses actually occur are scattered over a larger range.

Table 3: Statistics for Tx at C and three people

L (dB)	N_L (sec^{-1})	$\bar{t}_L$ (sec)
3	0.554	1.765
0	1.308	0.295
-3	0.755	0.150
-6	0.151	0.158
-9	0.050	0.275
-12	0.050	0.008

Table 4: Statistics for Tx at J and three people

L (dB)	N_L (sec^{-1})	$\bar{t}_L$ (sec)
6	0.101	9.868
3	2.526	0.290
0	3.183	0.118
-3	1.768	0.080
-6	0.859	0.092
-9	0.354	0.143
-12	0.303	0.131
- 15	0.202	0.147
- 18	0.202	0.110
- 21	0.152	0.115
- 24	0.152	0.079
- 27	0.051	0.079

Table 5: Statistics for Tx at D and three people

L (dB)	N_L (sec^{-1})	$\bar{t}_L$ (sec)
6	0.403	2.425
3	2.013	0.335
0	2.567	0.146
-3	1.761	0.126
-6	1.309	0.095
-9	1.107	0.059
-12	0.352	0.090
-15	0.302	0.058
-18	0.101	0.080
-21	0.101	0.060
-24	0.050	0.027

Table 6: Statistics for Tx at F and six people

L (dB)	N_L (sec^{-1})	$\bar{t}_L$ (sec)
9	0.101	9.894
6	0.756	1.256
3	2.269	0.331
0	3.177	0.144
-3	2.219	0.094
-6	1.059	0.082
-9	0.454	0.075
-12	0.101	0.121
- 15	0.101	0.022

For the situation of transmit antenna at placement J we obtained level crossings down to –27 dB about the mean. As can be seen by the tabulated results, the average duration of these very deep fades are rather short.

To compare the results obtained in the cluttered laboratory shown in Figure 40 with results extracted from a venue of larger dimensions, a further set of measurement data were obtained at a large vacant uncluttered office building. The building is located at 153 Rockingham Road Hamilton Hill, Perth, Australia, and is now used as an office for a new radio station. The construction material employed for the walls of this building is different to that of the laboratory, being double brick. The materials used for the floor and ceiling are similar to that of the laboratory being non-metalic acoustic tiles for the roof, and a carpeted concrete floor. The office also has the same ceiling height as the laboratory of 3 m. At the time of measurement the office was unfurnished. Our preliminary measurements revealed that the local mean was not influenced by factors such as external vehicular or pedestrian motion, this being primarily assisted by the fact that the office is located on the vacant first floor of the building. The office has two doorways, seven windows, and is rectangular of size 18.4 m by 12.6 m. A plan view of the office is shown in Figure 49.

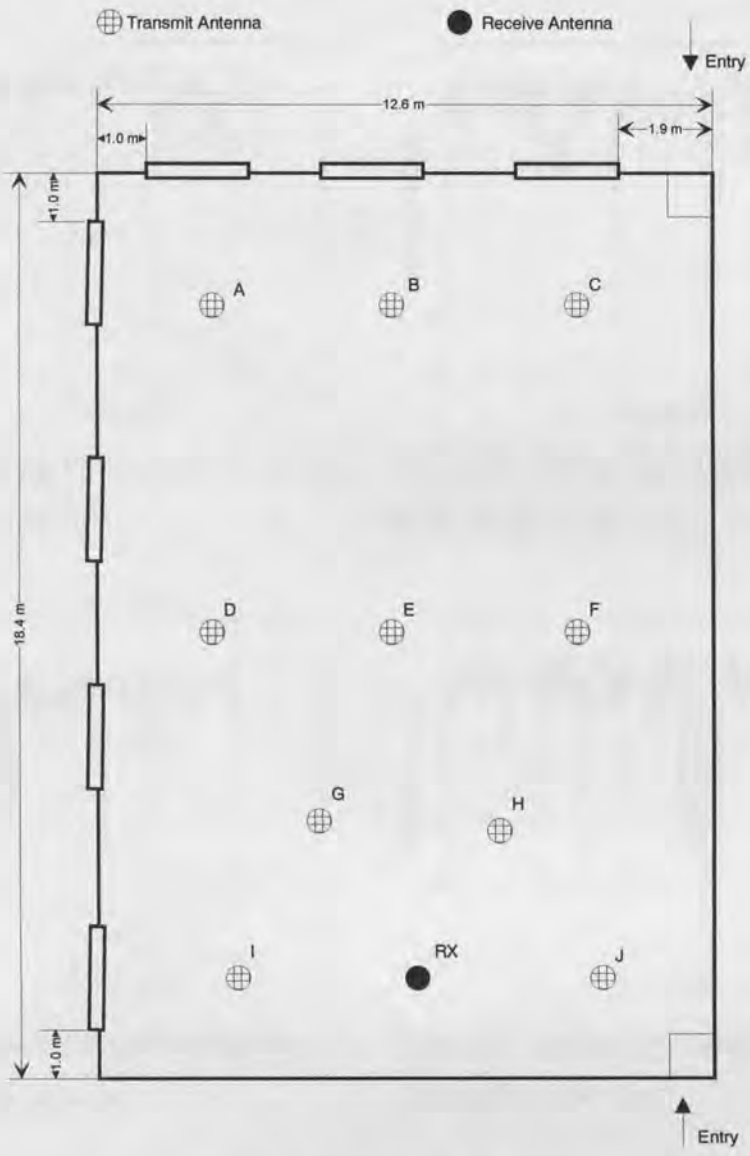

Figure 49: Plan view of the office

The same measurement procedure was adopted as given in Section 6.3 and from our measurements four representative recordings are shown in Figures 50, 51, 52, and 53.

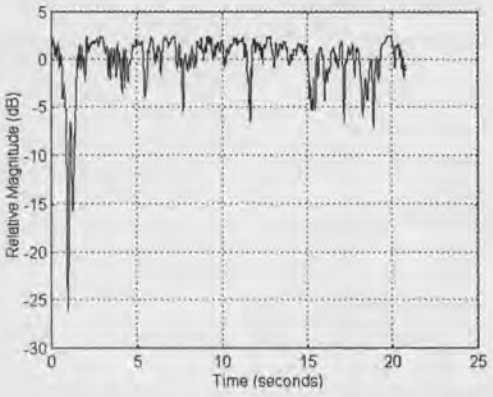

Figure 50: Fading for transmit position C, three people in motion.

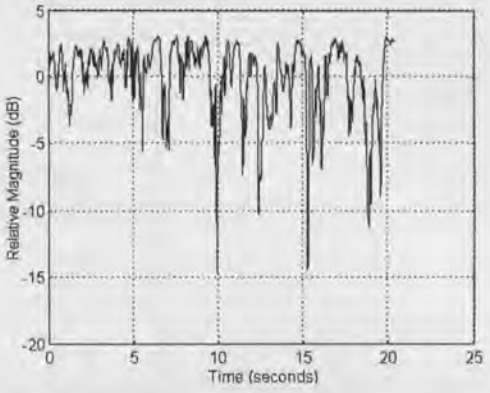

Figure 51: Fading for transmit position J, three people in motion.

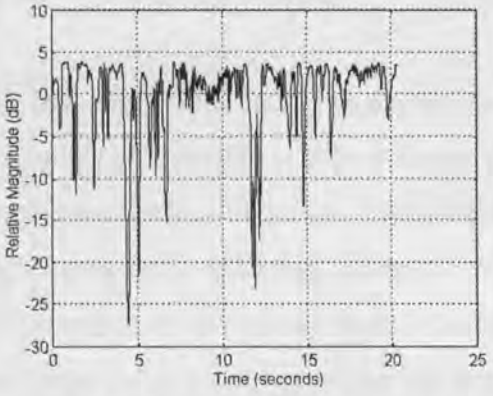

Figure 52: Fading for transmit position D, three people in motion.

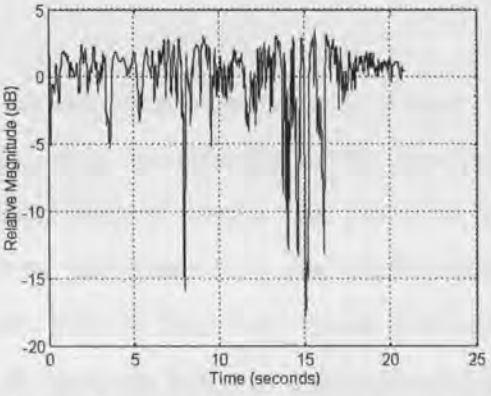

Figure 53: Fading for transmit position F, six people in motion.

The data depicted in Figures 50, 51, 52, and 53 was gathered eighteen months after that shown as Figures 41, 42, 43, and 44. The computation of the Rician k-factor for the latter set of data (for the larger vacant office building) approximated the same overall k-factor range for similar motion of people around the receive antenna as was found for the smaller cluttered laboratory. Table 7 displays the results.

Table 7: Rician k-factor Office Venue

Placement	k
C	8.5
J	2.6
D	2.2
F	1.5

6.6 Conclusions

We investigated the fading characteristics of the indoor radio propagation channel at a frequency of 2.4 GHz at two different venues, one a cluttered laboratory, the other a uncluttered office of larger dimensions. The motion of people was found to be a significant factor affecting fading at both venues, and results were remarkably similar with respect to their fit to Rician distributions. For the laboratory venue k values in the range $1.3 \leq k \leq 8.7$ provided the best fit. A statistical analysis of the recorded data was performed which results in level crossing rates and average duration of fades. From this analysis which is detailed in Tables 3, 4, 5, and 6, it can be seen that the level crossing rates reduce as L the depth of the fade value relative to the mean value reduces, which is an intuitive result. A relationship between the computed Rician k-factors presented in Table 2, and level crossing rates L shown in Tables 3, 4, 5, and 6, is also evident. Lower Rician k-factor values in the range from 1.3-2 were computed from measurement data for antenna placements J, D, and F respectively. Analysis of Tables 3, 4, 5, and 6, shows that the level crossing rates N_L for any nominal value of L are much higher for antenna placements J, D, and F, than for antenna placement C which had a value for k of 8.7. The tables also show that the maximum measured fade depth recorded for antenna placements J, D, and F, of -27, -24, and -15 dB respectively, are of much higher order than the maximum measured fade depth recorded for antenna placement C, which was –12 dB. The higher order of the fade depths and N_L values implies a greater variation of the received signal

envelope with the effect of the more dominant direct wave being reduced. There is therefore a movement towards the Rayleigh distribution as the magnitude of the Rician k-factor reduces. The k-factor values computed from our measurement data are related to the degree of motion introduced in the laboratory, which has been shown to be an important fading influencing factor. The second series of measurements performed eighteen months later in the office provided data that after analysis produced approximately the same range for k-factor as derived from data for the first series of measurements. In Chapter 7 of this thesis the k-factor statistics computed from our fading measurements are used to estimate the BER performance of the indoor radio propagation channel for BPSK and QPSK digital modulation.

Chapter 7

Bit Error Rate Analysis

In this Chapter we analyse and predict the BER for digital modulation. The modulation method considered is coherently detected QPSK with a raised cosine signalling pulse. The pulse is realised by a filter having the square root of a raised cosine spectrum of roll-off factor 0.5. This signalling waveform and its matched filter form an ISI-free pulse in the absence of delay spread [5]. BER probabilities are computed for the indoor measurement channel for both Rician and Rayleigh fading using the fading data gathered and analysed in Chapter 6. The affect of non-systematic noise generated from an operational microwave oven on BER is analysed and a set of curves computed and plotted from data gathered experimentally for a calibrated antenna measurement at 5 metre range from the oven. The affect of delay spread on BER is also discussed, and compared with data obtained from a computer simulation given in [5].

7.1 Bit Error Rate and Digital Modulation

In the absence of interference from non-systematic noise sources, received signal fading is the primary factor affecting the BER performance of the indoor radio propagation channel. By the selection of an indoor venue which offers a static measurement environment, and therefore provides a constant received signal level in the absence of motion, it has been possible to determine the affect of fading and interference on BER for the indoor radio channel with data transmission rates up to 8 megabits/second. The upper limit of 8 megabits/second being for QPSK modulation at the 4 megasymbols/second rate (2 bits/symbol).

The nature of received signal fading for the indoor radio propagation channel can be separated into two main categories:

1. Flat Fading.

2. Frequency Selective Fading.

Both of these fading mechanism result in dynamic changes to the BER probability for the digital modulation employed to transmit data over the indoor radio channel. Our measurement data has shown that both fading mechanisms coexist for the indoor channel. By moving the position of either the transmit or receive antenna a small distance, typically less than 12.5 cm, which corresponds to λ at the mid-band measurement frequency of 2.4 GHz, then fading that is predominantly either wide-band flat fading or frequency selective fading was observed for the static channel. Examples of these fading mechanisms are shown for a coherently detected QPSK modulated received signal in Figures 54, 55, and 56. In Figure 54 the received wide-band signal has minimal fading and is relatively flat across the full frequency band, with the centre frequency of 2.4 GHz having a received power level of -65.886 dBm as shown at top right of the Figure. For Figure 55, a small movement of the receive antenna, with the static situation still being maintained within the laboratory, produced a fade that is in the main a flat fade where all received frequencies are significantly reduced in power across the whole band. It can be seen for the flat fade of Figure 55 that the reduction in power level received for the mid-band 2.4 GHz frequency is to a value of -98.12 dBm, a margin of 32.234 dB. This substantial fade is solely due to the vector addition of all multipath signals in the static laboratory, and the measurement was easily repeated by maintaining the same transmit and receive antenna placements. Similarly, a further small movement of the transmit antenna resulted in the received power spectrum shown as Figure 56. From Figure 56 it can be seen that there has been frequency selective fading, the lower frequencies in the band have suffered greater attenuation than the higher frequencies, and the asymmetry is evident. The mid-band power level at 2.4 GHz has fallen to a value of -74.591 dBm, which is only 8.705 dB lower than its value for the minimally faded value of Figure 54. Only an extremely small change to the received power values can be attributed to the small variation in distance (or range) between the transmit and

receive antennae, as this distance approximated 6 metres (48 wavelengths mid-band), and as previously stated the movement of the transmit antenna was less than one wavelength mid-band.

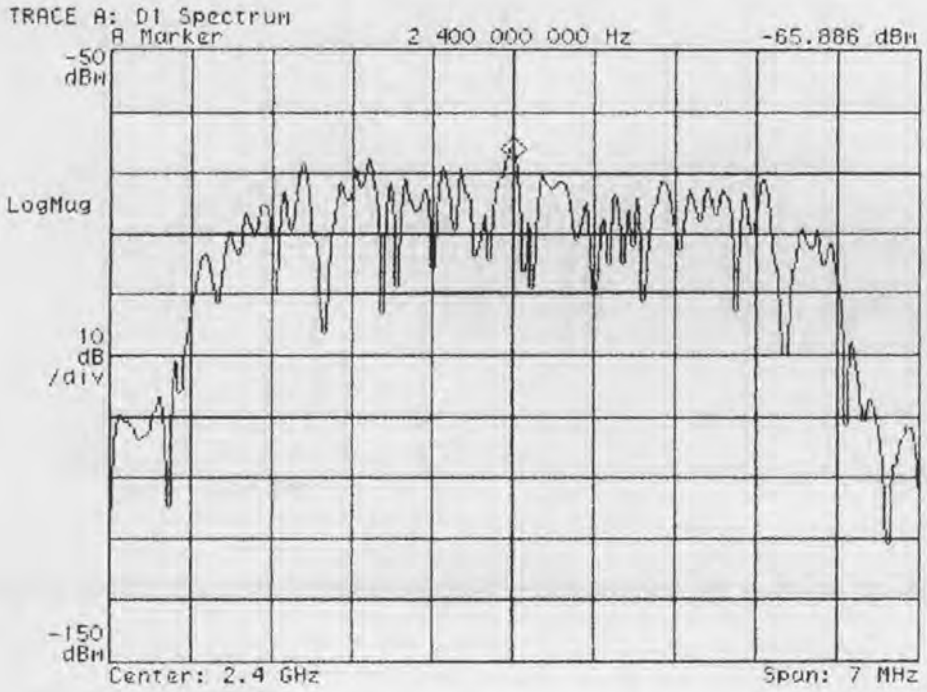

Figure 54: Received wide-band coherently detected QPSK with minimal fading.

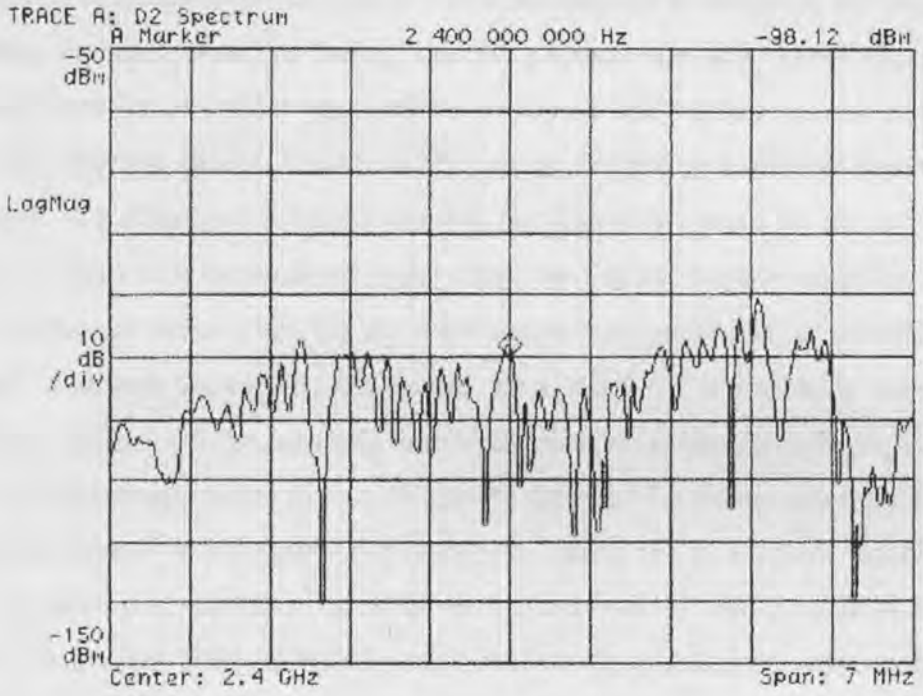

Figure 55: Received wide-band coherently detected QPSK with flat fading.

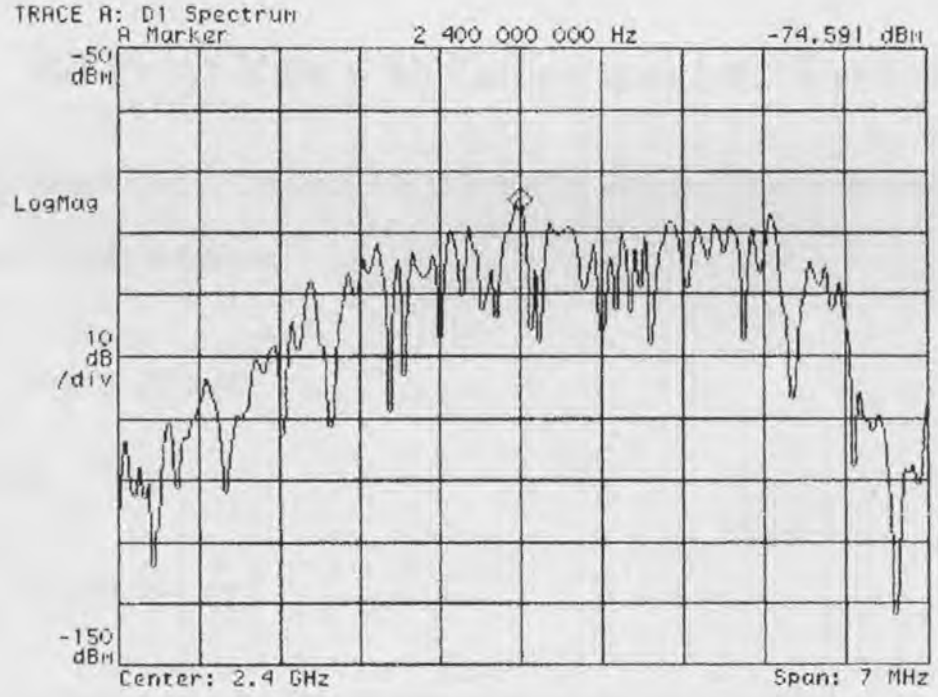

Figure 56: Received wide-band coherently detected QPSK with frequency selective fading.

The motion of people or other objects within the channel is identified in Chapter 6 as providing the main cause for fading, also the physical size and type of construction materials used for the indoor venue affects multipath delay spread and the consequent frequency selective fading. The irreducible errors, defined as those that occur at very high SNR in a frequency selective channel, are primarily caused by the level of ISI which interferes with the received signal component at the receiver sampling instants. These errors can occur when (a) the main signal component path is cancelled by a delayed multipath signal, (b) ISI exists as a result of a non-zero value of d (Equation 3.25), or (c) the sampling time of the receiver is shifted as a result of delay spread. In our measurement system (Figure 6) the need for carrier recovery from the transmitted signal is not required to establish timing for receive bit sampling, (c) therefore does not contribute to BER in the analysis of our measurements. The increase in average BER probability attributed to (a), (b), and non-systematic noise interference from sources such as operational microwave ovens can be characterised from our measurement data presented in Chapter 6, Appendix F and Chapter 5 respectively.

7.2 Bit Error Rate with Fading and Interference

The Q-function Q(x) in Equation (3.5) is frequently used in another form where it is related to erfc(x) as follows:

$$\text{erfc}(x) = 2Q(x\sqrt{2}) \tag{7.1}$$

Therefore:

$$Q(x) = \frac{1}{2}\text{erfc}\left(\frac{x}{\sqrt{2}}\right) \tag{7.2}$$

by the substitution from Equation (3.5) for Q(x) into Equation (7.2), where:

$$x = \sqrt{\frac{2E_b}{n_0}} \tag{7.3}$$

then:

$$P_{e,BPSK} = \frac{1}{2} erfc \sqrt{\frac{E_b}{n_0}} \tag{7.4}$$

By the introduction of a fading variable (χ) Equation (7.4) can be modified as follows:

$$P_{e,BPSK}|\chi = \frac{1}{2} erfc\left[\sqrt{\frac{E_b}{n_0}}(\chi)\right] \tag{7.5}$$

If instead of a sample value of a random fading variable χ in Equation (7.5) we have a constant value C_0, then Equation (7.5) becomes:

$$P_{e,BPSK}|_{\chi} = \frac{1}{2} erfc\left[\sqrt{\frac{E_b}{n_0}}(C_0)\right] \tag{7.6}$$

In the absence of any fading or interference, that is $C_0 = 1$, the BER is given as before by Equation (7.4) the well known equation for average bit error rate of a coherently demodulated BPSK signal.

7.3 Bit Error Rate and Error Vector Magnitude

The EVM is a measurement parameter that is expressed as a % rms value and a % peak value. It is often convenient to think of physical data in terms of a static or time invariant component, and a dynamic or fluctuating component [65]. We can describe the static component by its mean value, which is the average of all measured values. In equation form the mean ($\bar{x}$) is given by:

$$\bar{x} = \lim_{N \to \infty} \frac{\sum_{j=1}^{N} x_j}{N} \tag{7.7}$$

The dynamic, or fluctuating component (υ_x^2) may be described by a variance, it is simply the mean square value about the mean value found from Equation (7.7), and it is given by:

$$\upsilon_x^2 = \frac{\lim_{N \to \infty} \sum_{i=1}^{N} (x_i - \bar{x})^2}{N} \tag{7.8}$$

The EVM is the square root of this variance value expressed as a percentage and its value when expressed numerically is directly related to the magnitude of the erfc variable of Equation (7.5), that is:

$$\left[\sqrt{\frac{E_b}{n_0}} (\chi) \right] \tag{7.9}$$

For the static situation with no received signal variation attributed to fading, Equation (7.6) applies, EVM % is directly related to the magnitude of the received signal power, and without the presence of interference such as noise from operational microwave ovens is representative of the systematic noise. The use of EVM as a calibration datum (Figure 10) permitted the identification of non-systematic noise entering via the antenna. By careful calibration of our test link for the static situation the value of EVM for received power level was checked to ensure that no external noise other than our noise which was deliberately introduced for the test measurements was present. An increase in particularly the % peak value of EVM was used to identify unwanted noise ingression that may affect our measurement data leading to invalid results.

7.3.1 Microwave Oven Noise and Bit Error Rate

BER performance statistics are derived from measured received data for QPSK modulation in the presence of random noise bursts from an operational microwave oven at 5 metre range. The cyclic transmission of a random data sequence of 600 symbols (1200 bits) in the presence of noise from the operational microwave ovens permitted experimental determination of BER for a range of received carrier levels.

The data sequence transmitted is presented in its received form without error as Figure 57.

TRACE A: Ch1 QPSK Syms/Errs
A Marker 158.0000 sym 1.0000

EVM	= 6.3780	%rms	20.335	% pk at sym	113
Mag Err	= 4.4481	%rms	16.263	% pk at sym	625
Phase Err	= 2.6237	deg	8.4447	deg pk at sym	413
Freq Err	= 8.5787	Hz			
IQ Offset	= -43.236	dB	Amp Droop = 166.2		udB/sym

0	01111101	01000101	10011110	01111100	01000001	01100000
48	01111111	11010101	11110010	01011111	11001101	01101111
96	11010100	00111110	01010000	01010101	00001111	00000011
144	01110111	01000111	01101011	11101111	11111111	00111101
192	11101101	00010101	10111110	01110001	01111101	10110111
240	11000111	01110111	11011011	00110101	01111111	00100101
288	00110001	01011001	01111100	1111[illegible]01	11011100	11010101
336	10010001	01111010	01111101	01111010	11001101	00000001
384	11111111	01010101	11101110	01111000	11100010	10101111
432	11010111	11111001	00010110	11100010	10010110	11110100
480	01111111	00010111	11101001	01110111	00110111	01111101
528	11010011	10111101	11111001	01111101	11100101	11111101
576	10010100	10001101	11100011	01101110	11001110	11111110
624	01001111	11001111	10111101	10101010	00011001	10010101
672	00110011	11011110	00110001	11000010	11101101	11101111
720	11000111	01110111	01011011	01110000	10101110	01101110
768	10110011	11110100	01110000	11011101	00111111	01111010
816	11111011	11101101	01110100	01101111	11110101	10001011
864	01001011	01111110	00100111	01011001	11100110	00011101
912	10010101	01110111	01011[illegible]01	01111010	11110111	10110111
960	01000011	01100101	00011111	01110101	01010111	00011001
1008	00110100	01110111	00111101	10110000	00011100	11010001
1056	01011101	11000111	11110011	11010100	11101101	01111001
1104	01010101	10001111	01111011	10011011	01010000	10001110
1152	01000010	00110101	11000001	01000001	10001101	11111101

Figure 57: Received Test Bit Sequence for cyclically transmitted data with QPSK modulation in the absence of random noise bursts from an operational microwave oven at range 5 metres (receive antenna :- resonant 1/4 λ monopole).

Analysis of received data for the test bit sequence shown in Figure 57 when the noise bursts from an operational microwave oven are present provided the statistical input for the development of BER performance curves for a range of receive carrier levels. A received test bit sequence with errors caused by microwave oven noise interference is depicted as Figure 58. The Figure shows an increase in EVM % rms from 6.3780 % in Figure 57 to 58.375 % in Figure 58, and an increase in EVM % peak from 20.335 % to 186.62 %. From analysis of the data received 516 errors occurred for the 1200 bits transmitted. Note that the two bit QPSK symbol number 158 (which represents data 01) and is highlighted in the tables was transmitted without error, but many other symbols were not.

TRACE A: Ch1 QPSK Syms/Errs
A Marker 158.0000 sym 1.0000

EVM	= 58.375	%rms	186.62	% pk at sym	50
Mag Err	= 41.318	%rms	153.95	% pk at sym	50
Phase Err	= 25.418	deg	44.976	deg pk at sym	689
Freq Err	= -9.3907	kHz			
IQ Offset	= -41.388	dB	Amp Droop = 2.259		mdB/sym

0	11101011	01111111	00111011	01101001	01110111	11100101
48	01101011	11110100	11110100	11001011	00001100	11001011
96	11110100	00101100	11010010	01011101	00000111	01000011
144	11110111	01000111	01001011	11001111	10111111	00111101
192	11101101	00100101	11111100	00111001	01110101	10110111
240	11000101	01110011	11001011	00100100	00110110	00110100
288	10001001	00001110	00011110	0111[illegible]000	01000110	11000001
336	11000000	00111111	01010100	00011110	01100100	10011000
384	11010111	00001100	01110111	00011111	01111010	11011001
432	01000001	00011100	10000001	01011011	01100011	01000000
480	10010001	10100000	01110111	00011001	10111100	00000000
528	00101101	01000110	00000110	00000010	01011011	00000010
576	01101011	01110011	00011101	10011101	00110001	01000011
624	10111010	00110000	11100010	01010101	11100010	01001010
672	11001110	00101001	01101110	10110110	10011010	10001010
720	00011000	10101100	11110110	11000111	01001000	10000000
768	00100110	10111101	11100110	10111011	01101010	11110010
816	11100010	10000011	11101101	01001010	00101101	00010110
864	11110010	01101001	01001110	11010011	10111100	11011011
912	00011111	11101111	01001111	01111011	10110111	10110111
960	01000011	01100101	00110111	01110101	11010111	01011011
1008	00111100	01100111	10111100	10110000	00011100	11010001
1056	01011100	11000111	11110011	00010100	10101101	01110001
1104	00010001	10001101	01111101	10011111	01001010	01100111
1152	01101011	00110000	11011000	00001000	11100100	01010100

Figure 58: Received Test Bit Sequence for cyclically transmitted data with QPSK modulation in the presence of random noise bursts from an operational microwave oven at range 5 metres (receive antenna :- resonant 1/4 λ monopole).

A series of measurements allowed data on BER to be gathered for carrier frequencies centred on each of the twenty frequency bins in the 2.3-2.5 GHz range. For each measurement the BER was averaged over the operating duration of the oven, which was selected as 3 minutes. As expected from Figures 26-28 the bins with the highest BER rates are bins 14-18 where the frequency of noise emissions from the operational microwave ovens exhibit the greatest time presence. Figure 59 displays data on BER performance for bins 14-17 when the loaded Toshiba oven was operational (note that from previous measurements for the Toshiba oven shown in Figure 26 that frequency drift does not affect bin 18). The curve for the BER rate performance of the measurement system as the received carrier level is varied is also depicted where the microwave oven is off and as such the system is only influenced by systematic noise. This curve is labelled "Microwave Oven Off" in each of the family of BER Figures shown following for the three ovens evaluated.

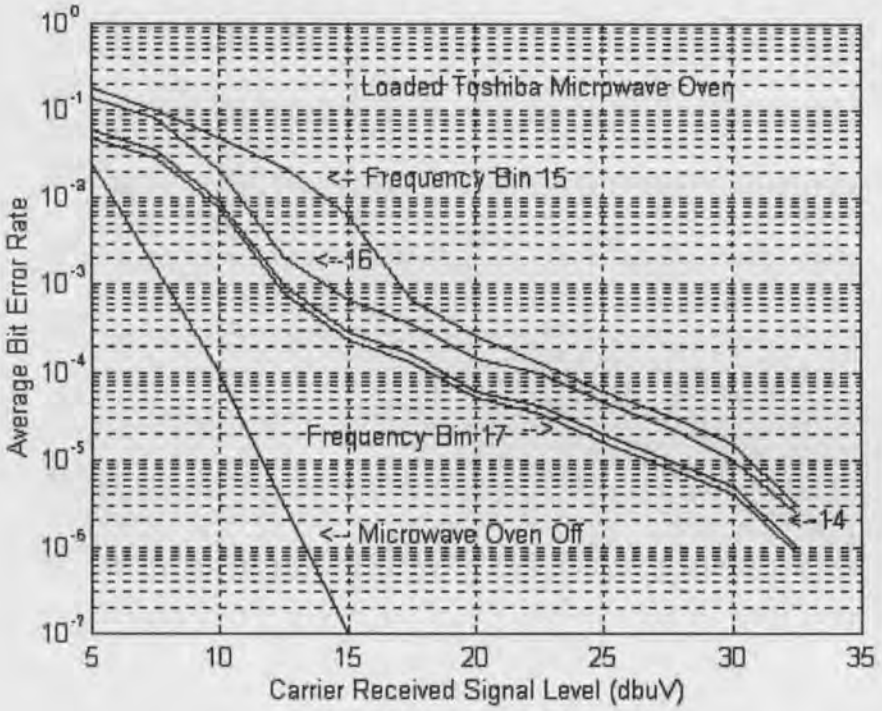

Figure 59: Measured BER performance of Received Test Bit Sequence for cyclically transmitted data with QPSK (Loaded Toshiba Oven receive antenna :- resonant 1/4 λ monopole at range 5 metres).

Figure 60 displays data on BER performance for bins 14-18 when the loaded Whirlpool oven was operational. Frequency drift does in this case affect the BER performance for bin 18.

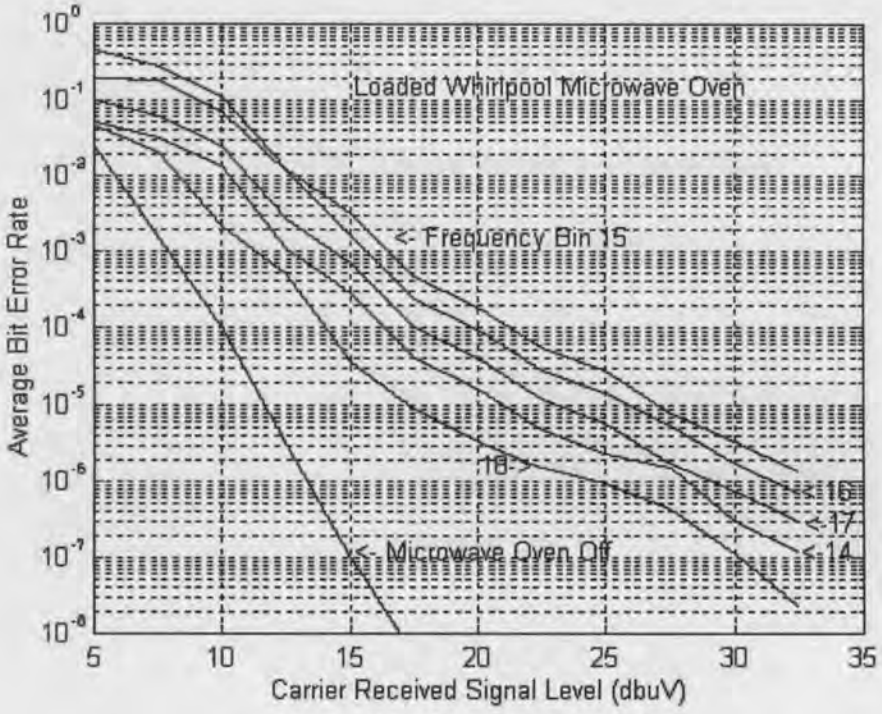

Figure 60: Measured BER performance of Received Test Bit Sequence for cyclically transmitted data with QPSK (Loaded Whirlpool Oven receive antenna :- resonant 1/4 λ monopole at range 5 metres).

Figure 61 displays data on BER performance for bins 14-18 when the loaded Mitsubishi oven was operational. As for the Whirlpool oven frequency drift does in the case of the Mitsubishi oven affect the BER performance for bin 18.

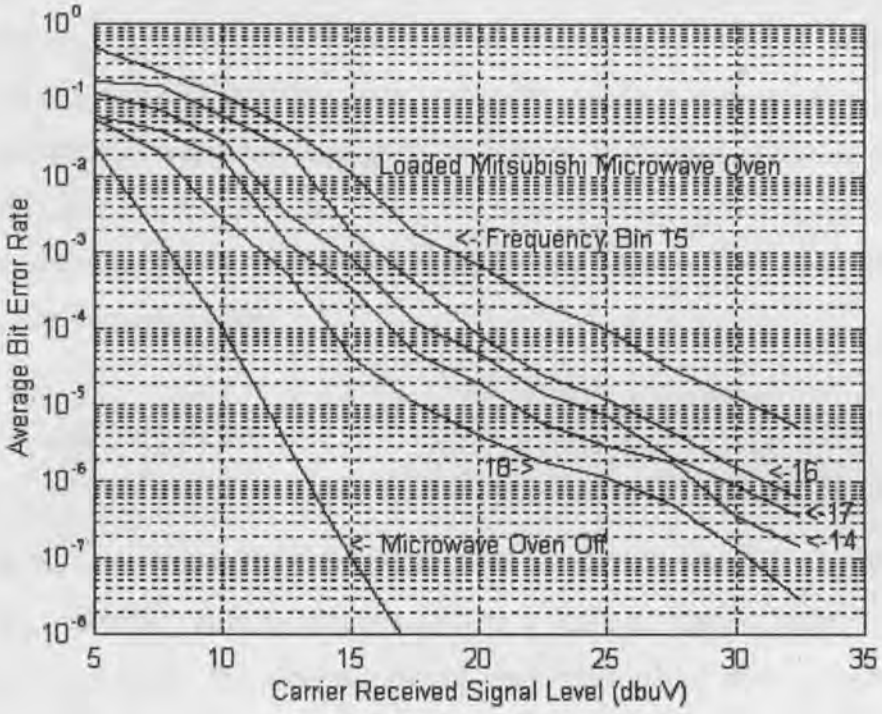

Figure 61: Measured BER performance of Received Test Bit Sequence for cyclically transmitted data with QPSK (Loaded Mitsubishi Oven receive antenna :- resonant 1/4 λ monopole at range 5 metres).

For measurements in frequency bins 1-13, 19, and 20 the three ovens (when operational) produced BER plots that approximated the plot for "Microwave Oven Off" in Figures 59, 60, and 61. A measurable increase in peak EVM was detected for these frequency bin numbers (Section 5.5). This was caused by the presence of the transient sinusoidal interference on magnetron power up and power down, however no errors were detected until the received carrier level was reduced to a values where thermal (systematic) noise which produced the "Microwave Oven Off" curves" is prevalent.

7.3.2 Fading and Bit Error Rate

If we now consider the effects of fading on BPSK and QPSK digital modulation for the indoor channel propagation path as caused by the motion of people within the channel, then the fading characterisation developed in Chapter 6 can be used to estimate average BER for received signal envelopes with Rician probability

distributions. By taking the approach of averaging the probability of error for a particular modulation in AWGN channels over the possible range of received signal levels caused by fading, then the error probability can be considered as a conditional error probability, where the condition is that χ in Equation (7.5) is fixed. The probability of error for slow flat fading channels is found by averaging the error in AWGN channels over the fading probability density function [40]. The probability of error is then evaluated from:

$$P_e = \int_0^{\infty} P_e(X)p(X)dX \tag{7.10}$$

$P_e(X)$ is the error probability at a specific SNR equal to X, where $X = \chi^2 E_b/N_0$, and p (X) is the probability density function of X as a result of channel fading. The fading variable χ represents the received fading amplitude values with respect to E_b/N_0 which is held constant. The Rician probability density function is well known, and using the same notation for the variables described in the CDF Equations (6.1), and (6.2) in Chapter 6, then it is given by:

$$p(R) = \frac{R}{\sigma^2}\exp\left(\frac{-(R^2+A^2)}{2\sigma^2}\right)I_0\left(\frac{AR}{\sigma^2}\right) \quad \text{for} A \geq 0, R \geq 0 \tag{7.11}$$

The Rician distribution of Equation (7.11) can be transformed [40] and expressed in terms of X a specific value of SNR (see Equation (7.10)) as:

$$p(X) = \frac{1+k}{\Gamma}\exp\left(-\frac{X(1+k)+k\Gamma}{\Gamma}\right)I_0\left(\sqrt{\frac{4(1+k)kX}{\Gamma}}\right) \tag{7.12}$$

where:

$$\Gamma = \frac{E_b}{N_0}\overline{\chi^2} \tag{7.13}$$

and Γ is defined as the average value of SNR. By setting the interference term ($I_T = 0$), and moving the fading variable (χ) under the square root sign in Equation (7.5) it can be expressed as follows:

$$P_{e,BPSK}|z = \frac{1}{2}\operatorname{erfc}\left[\sqrt{\frac{E_b}{n_0}\chi^2}\right] \tag{7.14}$$

As previously defined, $P_e(X)$ is the error probability at a specific SNR equal to X, where $X = \chi^2 E_b/N_0$, therefore the substitution can be made for X into Equation (7.14):

$$P_e(X) = \frac{1}{2}\operatorname{erfc}\left[\sqrt{X}\right] \tag{7.15}$$

Equation (7.15) is the familiar BER probability calculation for BPSK and QPSK coherently detected digital modulation at a SNR specified by X. Substituting Equations (7.15) and (7.12) in Equation (7.10) gives:

$$P_e|\Gamma,k = \int_0^\infty \left[\frac{1}{2}\operatorname{erfc}\left[\sqrt{X}\right]\right]\left[\frac{1+k}{\Gamma}\exp\left(-\frac{X(1+k)+k\Gamma}{\Gamma}\right)I_0\left(\sqrt{\frac{4(1+k)kX}{\Gamma}}\right)\right]dX \tag{7.16}$$

Solving the integration numerically provides the average probability of bit errors for BPSK and QPSK coherently detected modulation in a Rician slow flat fading channel. The numerical integration was performed using Matlab© and the results for average BER probability for a range of average E_b/N_0 is presented in Figure 62. The curve representing k = 8.7 is truncated at an E_b/N_0 value equal to 9 dB, this limit resulted from restricted computational value ranges in Matlab©. By setting k in Equation (7.16) equal to zero, where Rician degenerates to Rayleigh fading conditions, the comparison with simulation results shown for coherent PSK in a Rayleigh flat fading channel given in Figure 5.53 of reference [40] was made. An excellent correlation between the two Rayleigh flat fading BER probability curves for PSK modulation is evident, with both simulations providing the same results and therefore lending support to the validity of Equation (7.16) and our Matlab© computations for k values other than zero.

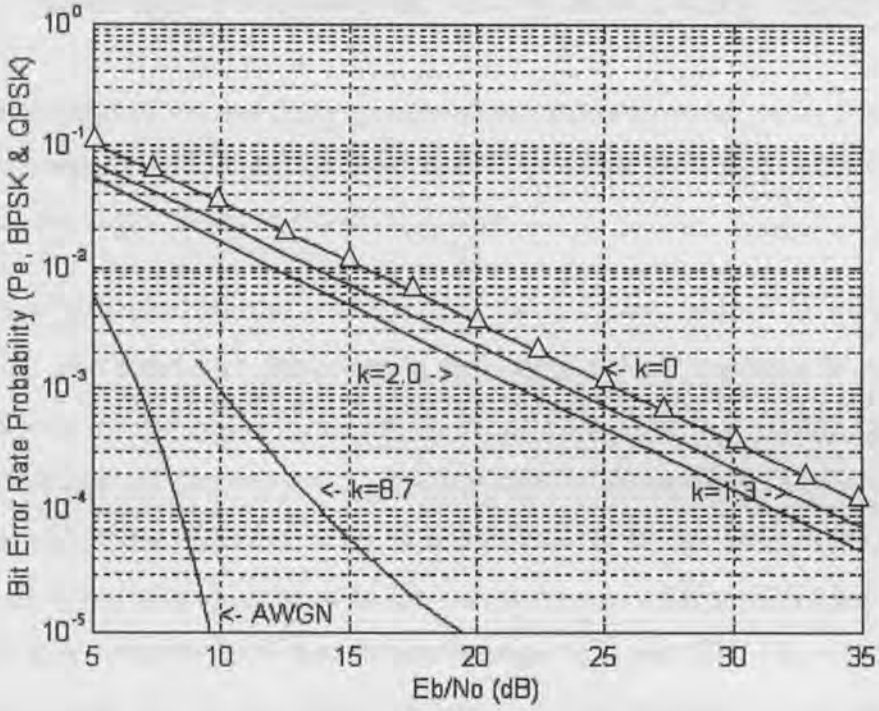

Figure 62: Average bit error rate probability for coherently detected BPSK and QPSK modulation with received signal fading caused by the motion of people around the receive antenna.

For k=0 solid: plot from Equation (7.16)

△: plot from Reference [40]

In Figure 62 we present predictions of the average BER probability for our indoor radio propagation channel measurement venue where the motion of people is present as for the fading measurements of Chapter 6. The results presented here are representative of those expected for indoor channels where this kind of movement of people commonly occurs, and are therefore most useful from a channel modelling perspective. Figure 62 clearly shows that a significantly higher probability of error exists for Rician flat fading channels when compared with AWGN at the same E_b/N_0 values. The BER probability curves corresponding to the Rician k values of 1.3, 2, and 8.7 as computed in Chapter 6 are shown, together with the Rayleigh (k = 0) and AWGN for BPSK and QPSK modulation over the flat fading indoor radio propagation channel. The results are for transmit antenna placements F, D, J, and C of the measurement venue depicted in Figure 40.

7.4 Average Irreducible BER and Delay Spread

With knowledge of the rms delay spread values calculated in Appendix F Table 8, the average irreducible BER can be estimated for transmit antenna placement F which exhibited the largest value of rms delay spread.

At the 4 megasymbol transmission rate used for all measurements the symbol period is 250 ns. The static rms delay spread (σ_r) computed in Appendix F for transmit antenna placement F at the measurement venue was 16.4433 ns. Using these values the normalised σ_n denoted by d, is computed from Equation (3.25) as 0.06577. Comparison of this value of d for raised cosine QPSK modulation of $\alpha = 0.5$ as employed in the measurements with the curves shown in Figure 63 (taken from [5]), predicts an irreducible BER somewhere between 10^{-2} and 10^{-3}. The analysis of the simulation used shows that these irreducible errors are those errors that occur if AWGN causes no errors. The simulation that produced Figure 63 indicated that the signal at the sampling instant is always in a deep fade when irreducible errors occur, and for small delay spread values then envelope fading is the most important mechanism causing error bursts.

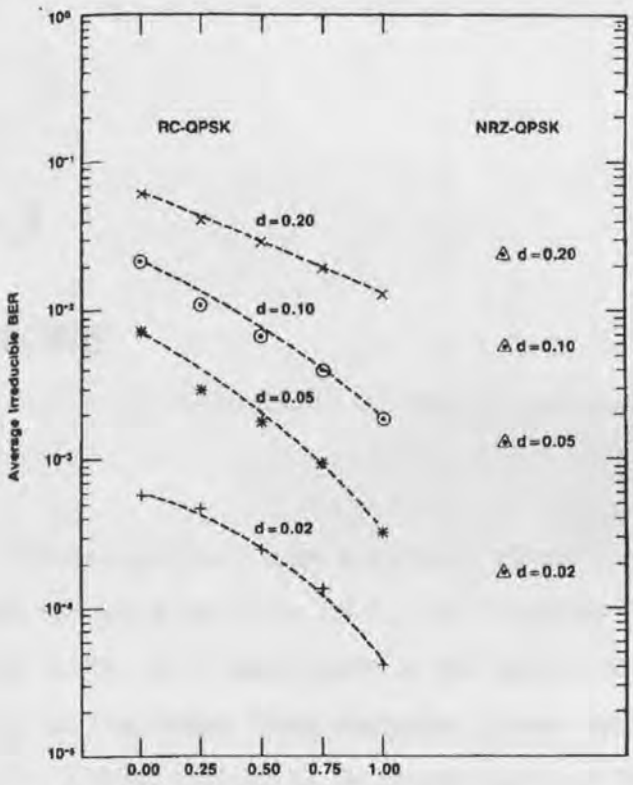

Figure 63: The irreducible error performance for raised cosine QPSK modulation with coherent detection. The parameter d is the rms delay spread normalised by symbol period, and α is the roll-off factor of the raised cosine filter. The curves were obtained from the results of a computer simulation [5] that used a measured impulse response profile for an office building as an input to the simulation.

Chapter 8

Conclusions

Electromagnetic radiation generated from operational microwave ovens is identified as a cause of radio receiver noise in the 2.3-2.5 GHz frequency band. The impact of this received noise on the BER performance of the indoor radio channel for data transmission must be considered when designing indoor radio channels in this frequency band. An in depth analysis on the characteristics of this form of noise is presented in Chapter 5 of this thesis. The identification of the existence of upper and lower cut-off frequencies for oven magnetrons, frequency drift statistics of the magnetrons when operational, and the characterisation of the noise duration and intensities emitted from operational microwave ovens is an original contribution of this thesis. The analysis of received data error rates over a test link in the presence microwave oven noise in concert with EVM values of the received data constellation permitted BER performance to be estimated for the test link. Measurement frequency bins 12 through to 18, which span the frequency range 2.41-2.48 GHz, have the highest levels of noise presence caused by operational microwave ovens. Data gathered from measurements of the non-systematic noise generated from operational microwave ovens at 5 metre range using a resonant monopole 1/4 λ antenna with a known antenna factor (AF) versus frequency relationship given by Equation (4.7) is presented in Section 5.2. From this data an estimate of the average peak electric field intensity (E_R) in the far field can be obtained, and Figure 21 provides the estimate of average peak electric field intensity at the 5 metre measurement range. The equivalent average peak electric field intensity at the radiating source can be computed by using the propagation path analysis techniques and equations introduced in Chapter 3 of this thesis. By the transposition of Equation (3.19) the equivalent

transmit power P_T from the operational microwave oven acting as an omnidirectional antenna can be calculated. This is achieved by substitution of 5 metres for range (r), and the appropriate E_R values from Figure 21 (after their conversion to volts/metre). For the twenty spectral measurement bins selected in Section 4.4, bin number 16 representing the frequency range 2.45-2.46 GHz exhibits the highest level of emission, and at range 5 metres the average measured peak electric field intensity is 114 dBμV/m or 0.50118 V/m. By the substitution of these values into Equation (3.19) then P_T is calculated as 209.323 milliwatts/m^2 (+23.208 dBm). For wavelengths of this order the operational microwave oven approximates an omnidirectional radiating antenna at measurement distances of 5 metres and greater. This worst case value of P_T can be considered a "Benchmark Value" when designing systems that operate in the frequency range of bin number 16. Similar benchmark values can be easily computed from our measurements for the 19 other measurement bins covering the 2.3-2.5 GHz range evaluated in this thesis. By the application of radio path design techniques, and the inclusion of appropriate building exit and entry losses at the propagation frequency for the proposed indoor channel, then an estimate of the worst case interfering noise levels expected from operational microwave ovens for any range can be computed.

The impact of the interfering noise levels generated by operational microwave ovens on the received BER for data transmitted over indoor radio transmission systems (for BPSK or QPSK digital modulation) is discussed in Chapter 7 of this thesis. It is also evident from our characterisation of additive channel noise from operational microwave ovens in Chapter 5 that the worst degradation of BER performance occurs for frequency measurement bin numbers 14-18 inclusive. These bins have the highest level of electromagnetic radiation for a significant part of the magnetrons "on-period" as given by the measured drift statistics presented in Section 5.4 of this thesis. The frequency span corresponding to measurement bin numbers 14-18 is 2.43-2.48 GHz. The selection of an operating frequency within this frequency span for an indoor radio channel will potentially expose the transmission system to interference from noise generated by operational microwave ovens, and therefore possible degradation of overall transmission system BER performance. The selection of a carrier frequency and a bandwidth that avoids the 2.43-2.48 GHz frequency range such as the

2.40-2.43 GHz portion of the ISM band will minimise the interference noise from operational microwave ovens. This selection will therefore provide best BER performance for indoor channels where oven noise is likely to be present. The proliferation of microwave ovens has increased the probability of one or more operational ovens degrading BER performance, with ovens being found at most measurement venues evaluated for noise in our measurement campaign. It is therefore recommended that 2.40-2.43 GHz be used as first choice for ISM band indoor radio propagation channels to minimise interference from noise generated by operational microwave ovens.

In the presence of operational microwave ovens the BER performance for bins 1-13, 19 and 20 approached the level of that attributed to systematic noise only, and although an increase in % peak EVM (maximum 25.983 % for bin number 11) was measured there were no data errors recorded. Although the probability for error increased as indicated by increase in EVM values, the receive carrier level had to be significantly reduced to a level where thermal systematic noise was high enough to produce BER degradation when combined with the introduced microwave oven noise for bins 1-13, 19 and 20.

In Chapter 6 of this thesis the received signal power variations caused by the motion of people around the receiving antenna of the indoor radio propagation channel was statistically characterised. This type of people activity within the physical channel itself is considered as the most typical occurrence that causes variance to the received signal power for indoor radio propagation systems [36], [37]. As a result of a series of propagation measurements at two selected indoor channel venues, data was gathered and statistically analysed to determine which was the most suitable fading distribution that best matched the measurement results. At both venues the variance in the received signal level was only influenced by the controlled motion of people around the receiving antenna, with no received signal level variance evident when the motion was not present. Rician flat fading was found as the most suitable distribution to fit our measured data for both venues. This finding is attributed to the geometry of the indoor channels used for the measurements which often had an unobstructed LOS path between transmit and receive antennae, along with many reflective paths off walls furniture people and other objects. For these conditions, where the reception of

a strong received signal over a direct LOS path exists simultaneously with many reflective multipath received signals, the fading distribution generally approximates a Rician one as the best fit.

Rician flat fading caused by the motion of people within the indoor radio propagation channel increases the average BER probability markedly when compared with the predicted BER for BPSK and QPSK modulation in the presence of AWGN at the same SNR values. From the analysis of measurement data gathered at our venue with people in motion (Section 6.5.1), we observed that the indoor radio propagation channel exhibited Rician flat fading characteristics with k values being typically in the range 1-2. The largest computed value of k for both venues was 8.7, and as depicted in Figure 62 the larger k value provided the best BER performance for the same SNR when compared with the lower k values. For the lower values of k there is a much higher probability of received bit errors, and for typical received E_b/N_0 ratios of 10-15 dB, from Figure 62 an average BER of one bit error for every one hundred bits transmitted over the indoor channel is predicted (10^{-2}). A BER probability of this order is not acceptable where large volumes of data are transmitted at high speed. The errors were observed to occur in bursts during periods of deep signal fading, and are large in number. The mechanism of receiving a large number of errors in bursts prevents the accurate restoration of the corrupted data by the application of error correction protocols, as too much data is received with consecutive errors. Tables 3-6 of Chapter 6 present fading statistics, these statistics show that the measured ADFs that reduce the SNR by 15 dB or more below the mean value, are within the range of 0.022-0.147 seconds. Many indoor radio systems operate with a design fade margin from signal to noise of 15 dB, therefore fades of this depth, and with these average duration's, can effectively reduce the received SNR to 0 dB. At the 4 megasymbol/second data symbol rate, and for ADFs of this time order, this equates to the reception of 88-588 kilobits of data for BPSK modulation, and 176-1176 kilobits of data for QPSK modulation for time period of the fade. Burst errors were observed to occur in all transmitted data sequences at SNR values approaching 0 dB, therefore error recovery was not possible when Rician fading caused fade depths to exceed the typical 15 dB design fade margins. The burst errors were not evident when motion of people was introduced to the channel after setting a

higher fade margin of 30 dB, thus lending support to the accuracy of the measured depth of fades (L) presented in Chapter 6, where the maximum fade depth measured was 27 dBm below the mean received power level.

Finally as a result of our investigation into "Factors Affecting the BER Performance of the Indoor Radio Propagation Channel for the 2.3-2.5 GHz Frequency Band" we conclude: -

Noise generated from operational microwave ovens and channel fading as a result of people in motion within the channel are the two main factors affecting BER performance of the indoor radio propagation channel for the 2.3-2.5 GHz band. Although other sources of noise exist within this frequency band the receive level of interfering noise from these sources was found to be sufficiently low as to deem them of no consequence when considering BER performance over links with minimal design carrier receive levels. The BER performance for data transmission in the presence of noise from operational microwave ovens is analysed in depth within this thesis.

The fading caused by people in motion within the channel is an important factor affecting the BER performance for the 2.3-2.5 GHz band and statistics obtained by measurement at two dissimilar sites under identical test conditions revealed highly correlated results. The BER predictions computed from measurement data and presented in this thesis can be used by other researchers as input data for development of smart antenna systems to reduce fading depths and improve BER performance.

Extreme care has been taken in the calibration of all measurement equipment employed in the data acquisition to provide statistics for presentation within this thesis. Experimental physics often leads to knowledge in areas yet unmapped in the theoretical sense, but care is essential to avoid experimental errors and consequently incorrect assumptions based on the measured results being proffered. All due care has been taken in the extremely time consuming experimental work undertaken within this thesis, and the author is confident that the results of this work has advanced the knowledge in this area of physics.

Chapter 9

References

[1] Rappaport, T.S., "Cellular Radio and Personal Communications Volume 2", *Institute of Electronic and Australian Engineers Inc*, Piscataway, N. J., 1996.

[2] Jakes, W.C., "Microwave Mobile Communications", *IEEE Press*, 1994.

[3] Cheah, J.Y.C., "Submission on Interference Characteristics of Microwave Ovens in Indoor Radio Communications", *IEEE P.802.11/91-52*, May 1991.

[4] Walker, E., Wysocki, T., and Hislop, J., "Noise Measurements in the 2.3-2.5 GHz Range", *UK/Australian International Symposium on DSP for Communication Systems*, September 1996, pp. 90-98.

[5] Chuang, J., C-I., "The Effects of Time Delay Spread on Portable Radio Communication Channels with Digital Modulation", *IEEE Journal on Selected Areas in Communications*, vol. 5, no. 5, June 1987, pp. 879-889.

[6] Lo, T., et.al., "New Approach for Estimating Indoor Radio Propagation Characteristics", *IEEE Transactions on Antenna and Propagation*, vol. 42, no. 10, October 1994, pp. 1369-1376.

[7] Bultitude, R.J.C., et al., "The Dependence of Indoor Radio Channel Multipath Characterisation on Transmit/Receive Ranges", *IEEE Journal on Selected Areas in Communications*, vol. 11, no. 7, September 1993, pp. 979-990.

[8] Devasirvatham, D.M.J., "Time Delay Spread Measurements of Wideband Radio Signals Within a Building", *Electronic Letters*, vol.20, no. 23, November 1984, pp. 950-951.

[9] Devasirvatham, D.M.J., Murray, R.R., and Banerjee, C., "Time Delay Spread Measurements at 850 MHz and 1.7 GHz Inside a Metropolitan Office Building", *Electronic Letters*, vol.25, no. 3, February 1989, pp. 194-196.

[10] Bultitude, R.J.C., Mahmoud, S.A., and Sullivan, W.A., "A Comparison of Indoor Radio Propagation Characteristics at 910 MHz and 1.75 GHz", *IEEE Journal on Selected Areas in Communications*, vol. 7, no. 1, January 1989, pp. 20-30.

[11] Takeuchi, T., Sako, M., and Yoshida, S, "Multipath Delay Estimation for Indoor Wireless Communications", in Proc. *IEEE Vehicle Technology Conference*, 1990, pp. 401-406.

[12] Devasirvatham, D.M.J., Banerjee, C., Krain, M.J., and Rappaport, D.A., "Multi-Frequency Radio Propagation Measurements in the Portable Radio Environment", in Proc. *IEEE International Conference on Communications*, 1990, vol. 4, pp. 1334-1340.

[13] Hawbaker, D.A., and Rappaport, T.S., "Indoor Wideband Radio Propagation Measurement System at 1.3 GHz and 4.0 GHz", in Proc. *IEEE Vehicle Technology Conference*, 1990, pp. 626-630.

[14] Devasirvatham, D.M.J., Krain, M.J. and Rappaport, D.A., "Radio Propagation Measurements at 850 MHz, 1.7 GHz and 4 GHz Inside Two Dissimilar Office Buildings", *Electronic Letters*, vol.26, no. 7, March 1990, pp. 445-447.

[15] Devasirvatham, D.M.J., Banerjee, C., Murray, R.R. and Rappaport, D.A., "Four-Frequency Radiowave Propagation Measurements of the Indoor Environment in a Large Metropolitan Commercial Building", in Proc. *IEEE GLOBECOM 91*, pp. 1282-1286.

[16] Hashemi, H., Tholl, D., and Morrison, G., "Statistical Modeling of the Indoor Radio Propagation Channel - Part I", in Proc. *IEEE Vehicle Technology Conference*, 1992, vol 1, pp. 338-342.

[17] Hashemi, H., Lee, D., and Ehman, D., "Statistical Modeling of the Indoor Radio Propagation Channel - Part II", in Proc. *IEEE Vehicle Technology Conference*, 1992, vol 2, pp. 839-843.

[18] Howard, S., and Pahlavan, K., "Autoregressive Modeling of Wide-Band Indoor Radio Propagation", *IEEE Transactions on Communications*, vol. 40, no. 9, September 1992, pp. 1540-1552.

[19] Hodale, P., Storoshchuk, O.L., Maslied, M.A., Van Der Jagt, L. Martin, G.L., and Szabados, B., "Propagation Measurements at a G.M. Manufacturing Plant for Wireless LAN Communication", in Proc. *IEEE International Symposium on Personal, Indoor and Mobile Radio Communications Proceedings*, 1992, pp. 334-338.

[20] Ganesh, R., and Pahlavan, K., "Statistical Characteristics of a Partitioned Indoor Radio Channel", *IEE Proceedings-I*, vol. 139, no. 5, October 1992, pp. 539-545.

[21] Huang, C., and Khayata, R., "Delay Spreads and Channel Dynamics Measurements at ISM Bands", in Proc. *IEEE Supercomm/ICC Conference*, 1992, vol 3, pp. 1222-1226.

[22] Morrison, G., Fattouche, M., and Zaghloul, H., "Statistical Analysis and Autoregressive Modeling of the Indoor Radio Propagation Channel", in Proc. *IEEE International Conference on Universal Personal Communications*, 1992, pp. 04.03/1-5.

[23] Zaharia, G.H., Elzein, G., and Citerne, J., "Time Delay Measurements in the Frequency Domain for Indoor Radio Propagation", in Proc. *IEEE Antennas and Propagation Society International Symposium*, 1992, vol 3, pp. 1388-1391.

[24] Manabe, T., and Takai, H., "Superresolution of Multipath Delay Profiles Measured by PN Correlation Method", *IEEE Transactions on Antennas and Propagation*, vol. 40, no. 5, May 1992, pp. 500-508.

[25] Hashemi, H., and Tholl, D., "Analysis of the RMS Delay Spread of Indoor Radio Propagation Channels", in Proc. *IEEE Supercomm/ICC Conference*, 1992, vol 2, pp. 875-881.

[26] Hashemi, H., "Impulse Response Modeling of Indoor Radio Propagation Channels", *IEEE Journal on Selected Areas in Communications*, vol. 11, no. 7, September 1993, pp. 967-978.

[27] Tholl, D., Fattouche, M., Bultitude, R.J.C., Malancon, P., and Zaghloul, H., "A Comparison of Two Radio Propagation Channel Impulse Response Determination Techniques", *IEEE Transactions on Antennas and Propagation*, vol. 41, no. 4, April 1993, pp. 515-517.

[28] Plattner, A., Prediger, N., and Herzig, W., "Indoor and Outdoor Propagation Measurements at 5 and 60 GHz for Radio LAN Application", *IEEE MTT-S*, 1993, OF-2-2.

[29] Rappaport, T., and Sandhu, S., "Radio-Wave Propagation for Emerging Wireless Personal-Communication Systems", *IEEE Antennas and Propagation Magazine*, vol. 36, no. 5, October 1994, pp. 14-24.

[30] Rustako, A.J. Jr., Amitay, N., Owens, G.J., and Roman, R.S., "Propagation Measurement at Microwave Frequencies for Microcellular Mobile and Personal Communications", in Proc. *IEEE Vehicular Technology Conference*, 1989, vol 1, pp. 316-320.

[31] Shimbo, O., Fang, R.J., and Celebiler, M., "Performance of M-ary PSK Systems in Gaussian Noise and Intersymbol Interference", *IEEE Transactions on Information Theory*, vol. 19, no. 1, January 1973, pp. 44-58.

[32] Prabhu, V.K., and Salz, J., "On the Performance of Phase-Shift-Keying Systems", *Bell System Technical Journal*, vol. 60, no. 10, December 1961, pp. 2307-2343.

[33] Ho, E.Y., and Yeh, Y.S., "A New Approach for Evaluating the Error Probability in the Presence of Intersymbol Interference and Additive Gaussian Noise", *Bell System Technical Journal*, November 1970, pp. 2249-2265.

[34] Lam, V.H., and Gaskell, P.S., "The Effect of Delay Spread on the BER Performance of Indoor Personal Communication Systems", in Proc. *IEEE International Conference on Mobile Radio and Personal Communications*, pp. 107-111.

[35] Nix, A. R., and McGeehan, J.P., Singapore ICCS/94.

[36] Walker, E., Zepernick, H-J., and Wysocki, T., "Fading Measurements at 2.4 GHz for the Indoor Radio Propagation Channel", in Proc. IEEE International Zurich Seminar on broadband Communications 1998, pp. 171-176.

[37] Zepernick, H-J., Walker, E., Singh, M., and Wysocki, T., "Fading Measurements and Analysis of the Indoor Propagation Channel in the 2.4 GHz ISM Band" in Proc. *Asia Pacific Conference on Communications*, Sydney, 1997, pp. 568-572.

[38] Walker, E., Wysocki, T., and Hislop, J., "Digital Signal Processing for Communication Systems", *Kluwer Academic Publishers*, Massachusetts, USA, 1997, pp. 121-130.

[39] Tan, K.T., and Wysocki, T., "A 7 Ray Empherical Based Model of an Indoor Microwave Wireless Mobile Channel with randomised Distortions", *VTC 97 IEEE 47th Vehicular Technology Conference Proceedings*, Phoenix, May 1997, vol. 2, pp. 1128-1132.

[40] Rappaport, T.S., "Wireless Communications Principles and Practice", Prentice-Hall Inc, Upper Saddle River NJ, 1996.

[41] Hashemi, H., "The Indoor Radio Propagation Channel", *Proceedings of the IEEE*, vol. 81, no. 7, July 1993, pp. 943-968.

[42] Stutzman, W.L., and Thiele, G.A., "Antenna Theory and Design", John Wiley and Sons, New York, 1991.

[43] Jordan, E.C., and Balmain, K.G., "Electromagnetic Waves and Radiating Systems", Prentice-Hall Inc, Englewood Cliffs NJ, 1968.

[44] Bello, P.A., "Characteristics of Randomly Time-Variant Linear Channels", *IEEE Transactions on Communications Systems*, vol. 11, December 1963, pp. 360-393.

[45] Friis, H.T., "Noise Figure of Radio Receivers", in Proc. *IRE*, July 1994, pp. 419-422.

[46] IRE Subcommittee 7.9 on Noise, Description of the Noise Performance of Amplifiers and Receiving Systems", in Proc. *IEE*, March 1963, pp. 436-442.

[47] Kennedy, G., and Davis, B., "Electronic Communication Systems", Macmillan/McGraw-Hill, Ohio, 1993.

[48] Turkmani, A.M.D., and Arowojolu, A.A., "Prediction of Microcellular Radio Propagation Characteristics Using Ray Theory", in Proc. *IEE Colloquium on Microcelluar Propagation Modelling*, Digest no. 234, pp. 2/1-6.

[49] Swarts, F., and Ferreira, H., C., "Markov Characterisation of Digital Fading Mobile VHF Channels", *IEEE Transactions on Vehicular Technology*, vol. 43, no. 4, November 1994, pp. 977-985.

[50] Hashemi, H., McGuire, M., Vlasschaert, T., Tholl, D., "Measurements and Modelling of Temporal Variations of the Indoor Radio Propagation Channel", *IEEE Transactions on Vehicular Technology*, vol. 43, no. 3, August 1994, pp. 733-737.

[51] Mitzlaff, J.E., "Radio Propagation and the Anti-Multipath Techniques in the WIN Environment", *IEEE Network Magazine*, November 1991, pp. 21-26.

[52] Molkdar, D., "Review on Radio Propagation Into and Within Buildings", *IEE Proceedings-H*, vol. 138, no. 1, February 1991, pp. 61-73.

[53] Karlsson, P., "Investigation of Radio Propagation and Macroscopic Diversity in Indoor Microcells at 1700 MHz", in Proc. *IEEE Vehicular Technology Conference*, 1990, pp. 390-395.

[54] Laurenson, D.I., Sheikh, A.U.H., and McLaughlin, S., "Characterisation of the Indoor Mobile Radio Channel Using a Ray Tracing Technique", in Proc. *IEEE International Conference on Selective Topics in Wireless Communications*, 1992, pp. 65-68.

[55] Karlsson, P., and Börjeson, H., "Measurement System for Indoor Narrowband Radio Propagation at 1700 MHz and some Results", in Proc. *IEEE Vehicle Technology Conference*, 1992, vol 2, pp. 625-628.

[56] Honcharenko, W., and Bertoni, H.L., "Mechanisms Governing Wireless Propagation Between Different Floors in Buildings", *Microwave Journal*, February 1994, pp. 24-34.

[57] Tadeuchi, T., Olsson, L., and Yoshida, S., "A Delay Profile Measuring Equipment For Indoor Radio Propagation", in Proc. *IEEE ICCS/ISITA Conference*, 1992, pp. 915-918.

[58] Yang, G., Pahlavan, K., and Lee, J.F., "A 3D Propagation Model with Polarisation Characteristics in Indoor Radio Channels", in Proc. *IEEE Global Telecommunication Conference*, 1993, vol 2, pp. 1252-1256.

[59] Yang, G., and Pahlavan, K., "Comparative Performance Evaluation of Sector Antenna and DFE Systems in Indoor Radio Channels", in Proc. *IEEE Supercomm/ICC Conference*, 1992, vol 3, pp. 1227-1231.

[60] McGladdery, W.A., and Stapleton, S., "Investigation of Polarization Effects in Indoor Radio Propagation", in Proc. *IEEE International Conference on Selective Topics in Wireless Communications*, 1992, pp. 53-56.

[61] Berkebile, J., Benalla, A., and Jacomb-Hood, A., "A Two Element Phased-array Antenna for Reducing Multipath Effects in Hand-held SATCOM Units", *Microwave Journal*, January 1996, pp. 24-36.

[62] Peterson, B., Hewlett Packard, "Spectrum Analysis Application Note 150", pp. 26-27.

[63] Sklar, B., "Digital Communications Fundamentals and Applications", Prentice-Hall Inc, Englewood Cliffs NJ, 1988.

[64] Holt, T., Pahlavan, K., and Lee, J.F., "A Computer Graphics Package for Indoor Radio Channel Simulation Using a 2D Ray Tracing Algorithm", in Proc. *IEEE Conference on Local Computer Networks*, 1992, pp. 511-518.

[65] Bendat, J.S., and Piersol, A.G., "Measurement and Analysis of Random Data", John Wiley and Sons, New York, 1969.

[66] Lee, W.C.Y., "Mobile Communication Design Fundamentals", Wiley and Sons, New York, 1993.

[67] Skomal, E.N., "Man-made Radio Noise", Van Nostrand Reinhold Company, New York, 1978.

[68] Steele, R., "Mobile Radio Communications", IEEE Press, New York, 1994.

[69] Viterbi, A.J., "Principles of Coherent Communications", McGraw Hill, New York, 1966.

[70] de Weck, J.P., Merki, P., and Lorenz, R.W., "Power Delay Profiles Measured in Mountainous Terrain", in Proc. 38th *IEEE Vehicular Technology Conference*, June 1988, pp. 105-111.

[71] Saleh, A.A.M., and Valenzuela, R.A., "A Statistical for Indoor Multipath Propagation", *IEEE Journal on Selected Areas in Communications*, Vol. 5, no. 2, February 1987, pp. 128-137.

[72] Janssen, J.M., Stigter, P.A., and Prasad, R., "Wideband Indoor Channel Measurements and BER Analysis of Frequency Selective Multipath Channels at 2.4, 4.75, and 11.5 GHz", *IEEE Transactions of Communications*, vol. 44, no. 10, October 96, pp. 1272-1288.

[73] HP89441A DC to 2.65 GHz Vector Signal Analyser, Technical Data, Hewlett Packard Co, 1994, p. 15.

[74] Oppermann, I., Graham, J.and Vucetic, B.S., "Modelling and Simulation of an Indoor Radio Channel at 20 GHz", in Proc. *IEEE Global Telecommunications Conference*, 1995, vol 1, pp. 744-748.

[75] Yamanaka, Y., and Shinozuka, T., "Statistical Parameter Measurement of Unwanted Emission from Microwave Ovens", Communications Research Laboratory, M.P.T, Japan 1995.

[76] Kobayashi, T., "Experimental Evaluation of Interference from Domestic Microwave Ovens to 1.9 GHz Digital Radio Transmission", NTT Wireless Systems Laboratories, Nippon Telegraph and Telephone Corporation, Japan 1995.

[77] Hashemi, H., and Tholl, D., "Statistical Modeling and Simulation of the RMS Delay Spread of Indoor Radio Propagation Channels", *IEEE Transactions on Vehicular Technology*, vol. 43, no. 1, February 1994, pp. 110-120.

[78] Blackard, K.L., Rapport, T.S., and Bostian, C.W., "Measurements and Models of Radio Frequency Impulsive Noise for Indoor Wireless Communications", *IEEE Journal on Selected Areas in Communications*, vol. 11, no. 7, September 1993, pp. 991-1001.

Appendix A

System Measurement Sensitivity for Non-Systematic Noise

The noise figure NF for the spectrum analyser HP8596E can be found by obtaining the true noise at its input port simply by terminating the input resistively with 50 ohms [62]. The input noise level (N) is then given by:

$$N = kTB \quad [W] \tag{A.1}$$

where:

k - Boltzmann's constant 1.38×10^{-23},

T - Absolute temperature in degrees Kelvin, and,

B - Bandwidth in Hz.

At reference temperature 290 K (which is a reasonable approximation of the source temperature of the 50 ohm resistive termination [63]) the input noise level can be calculated for a 1 Hz bandwidth from (A.1) as:

$$N = kTB = -174\text{dBm}$$

The noise level displayed on the spectrum analyser represents the noise contribution of the resistive 50 ohm termination, as well as internal noise generated within the analyser itself. This displayed level of noise has a random distribution and is bandwidth dependent. The power differential (D) that is measured in any RBW by the analyser relative to a 1 Hz bandwidth, can be calculated from the relationship:

$$D = 10\log(RBW/1) \quad [dB] \tag{A.2}$$

Allowing for the input noise N, the noise figure NF for the spectrum analyser can be determined from:

$$NF = (\text{measured noise}) - D - N \tag{A.3}$$

Substituting for the measured value of noise of –110 dBm (for the HP8596E spectrum analyser with a 50 ohm resistive termination on the input port, and the minimum RBW of 300 Hz) into Equations (A.2) and (A.3), then:

$$NF = (110\text{dBm}) - 10\log(300/1) - (-174) = 39.23\text{dB}$$

The spectrum analyser noise temperature (T_r) can be calculated at reference temperature (taken as 290 K), from its NF (expressed numerically) as follows:

$$T_r = (NF - 1)290 \quad [K] \tag{A.4}$$

$$T_r = 2.428 \times 10^6 \quad [K]$$

The overall system noise temperature (T_s) is given by:

$$T_s = T_a + T_r + (LT_r) \quad \text{(see Figure 11)} \tag{A.5}$$

where L is defined as the feeder line loss power ratio and is expressed as:

$$L = \text{feeder input power} / \text{feeder output power} \tag{A.6}$$

The measured loss of the RF feeder cable used for all noise measurements was 1.2 dB.

This insertion loss value translates to a feeder line loss power ratio, L = 1.3182.

The overall system noise out (N_{out}) can be found from:

$$N_{out} = G_r kB(T_a + T_r + (LT_r)) \quad [W] \tag{A.7}$$

The antenna is assumed to have no dissipative parts [63], its gain, unlike an amplifier, is thought of as a processing gain. The noise available at the antenna (T_a), after the antenna processing gain, has no contributive noise that is itself generated by the antenna.

The RF feeder noise temperature, T_f, can be calculated at reference temperature:

$$T_f = (L-1)290 = 93.2K \qquad (A.8)$$

The System Measurement Sensitivity is determined from (A.7) by calculation of the value of Nout with the antenna contribution Ta set equal to zero, and the RBW set to minimum at 300 Hz. This figure of Nout ($T_a = 0$) tells us the level a sinusoidal signal power at the antenna port must exceed before it can be resolved.

Setting Ta equal to zero, and substituting for G_r, k, T_r, T_f, L, and B in Equation (A.7) gives:

$$N_{out}(T_a = 0) = -108.8\text{dBm}$$

This value is the system measurement sensitivity and corresponds to the lowest level sinusoid that can be resolved by the overall measurement system as shown in Figure 11, for zero antenna gain. However, by use of the high gain corner reflector antenna the overall measurement sensitivity is increased by 15 dB to -123.8 dBm.

The noise available at the antenna N_a, can be calculated as:

$$N_a = G_a kBT_a \quad [W] \qquad (A.9)$$

The corner reflector antenna had the highest gain of the three antennas used in the noise measurements, with 15 dBi gain. This corresponds to a processing gain (G_a) of 31.62. The noise contribution for any given antenna temperature Ta, is found from Equation (A.9). The system measurement sensitivity of -123.8 dBm is adequate for the identification of noise sources that have sufficient intensity to significantly influence BER performance of data transmissions over the indoor radio channel [38].

Appendix B

Specifications for Measurement Antennae

Antenna Model: VO10-2325

Features:

- Omnidirectional.
- Vertical polarisation.
- Ground driven element for lightning protection.
- Fibreglass radome for weather protection.
- No assembly or tuning required.
- Lightweight design.

Specifications:

Electrical	
Frequency range	2.3-2.5 GHz
Gain (mid-band)	10.2 dBi
Bandwidth for 1.5:1 VSWR	2.3-2.5 GHz
Polarisation	Vertical
Maximum input power	100 watts
Lightning protection	Direct ground
Termination	N-type socket
Radiation pattern	Refer diagram

Mechanical	
Overall length	1.5 m
Diameter	0.048 m
Weight	2.1 kg
Support pipe material	aluminium
Radome material	Fibreglass
Effective wind area	0.62 m^2
Rated wind velocity	240 km/h
Shipping weight	5 kg
Shipping volume	0.005 m^3
shipping dimensions	1.3 x 0.06 x 0.06 m

Radiation Pattern for VO10-2325 antenna:

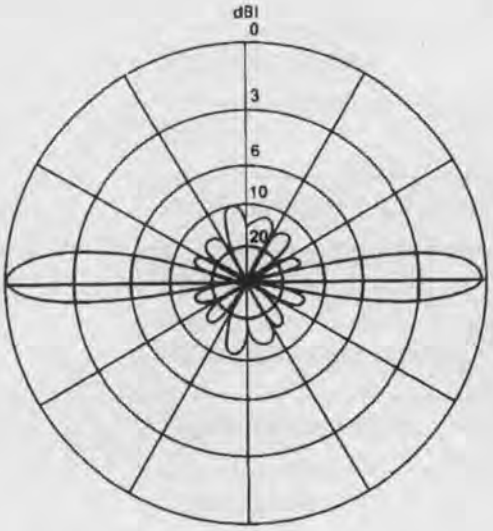

Vertical pattern (side view)

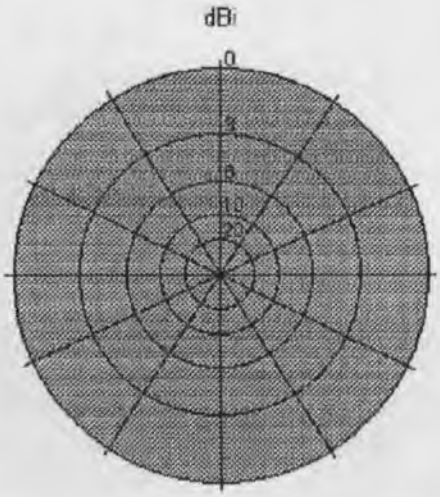

Horizontal pattern (top view)

Antenna Model: DRT 2415

Features:

- Broadband antenna suitable for diplexed and multi-coupled systems.
- High front to back ratio.
- Low side lobe gain provides additional protection against interference.
- Radome for weather protection.
- Supplied dismantled to minimise transport cost.
- Lightweight design.

Specifications:

Electrical	
Frequency range	2.3-2.5 GHz
Gain	15.0 dBi
Bandwidth for 1.4:1 VSWR	2.3-2.5 GHz
Polarisation	Horizontal or Vertical
Maximum input power	100 watts
Lightning protection	Direct ground
Termination	N-type socket
Radiation pattern	Refer diagram
Front-to-back ratio	> 25 dB
Crossed polarisation	> 25 dB
3 dB beam width E-plane	47 deg
3 dB beam width H plane	55 deg

Mechanical	
Reflector height	0.25 m
Reflector length	0.37 m
Reflector depth	0.25 m
Reflector material	Aluminium
Weight	1.5 kg
Mounting hardware	Designed for 25-42 mm diameter pipe
Radome material	ABS
Effective wind area	0.14 m^2
Rated wind velocity	200 km/h
Shipping weight	2 kg
Shipping volume	0.011 m^3
shipping dimensions	0.3 × 0.3 × 0.12 m

Radiation Pattern for DRT 2415 antenna:

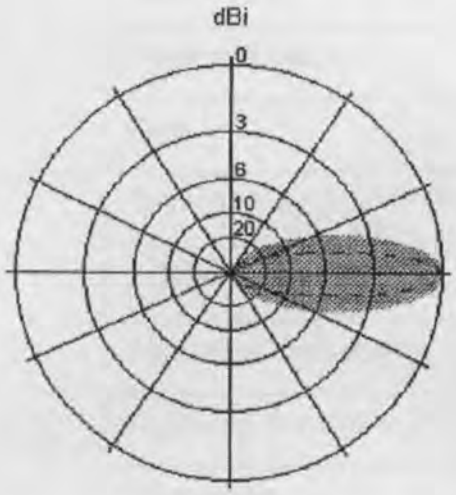

---------- H Plane (Vertical polarisation)

..... E Plane (Horizontal polarisation)

Antenna Model: Quarter-wave Monopole

Features:

- Omnidirectional.
- Vertical polarisation.
- Ground driven element for lightning protection.
- Lightweight design.

Specifications:

Electrical	
Frequency range	2.3-2.5 GHz
Gain	2.15 dBi
Bandwidth for 1.5:1 VSWR	2.33-2.47 GHz
Polarisation	Vertical
Maximum input power	100 watts
Lightning protection	Direct ground
Termination	N-type socket
Radiation pattern	Refer diagram

Mechanical	
Overall length	0.09 m
Diameter	125 mm
Weight	0.75 kg
Support pipe material	PVC
Radome material	none
Effective wind area	0.003 m^2
Rated wind velocity	310 km/h
Shipping weight	1 kg
Shipping volume	0.0023 m^3
shipping dimensions	0.15 × 0.15 × 0.10 m

Radiation Patterns for Quarter-wave Monopole antenna:

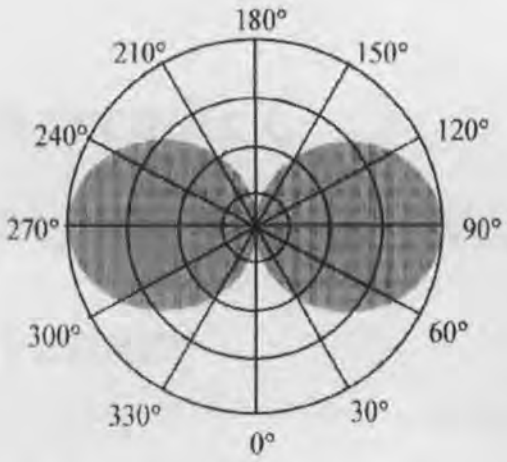

Vertical pattern (side view)

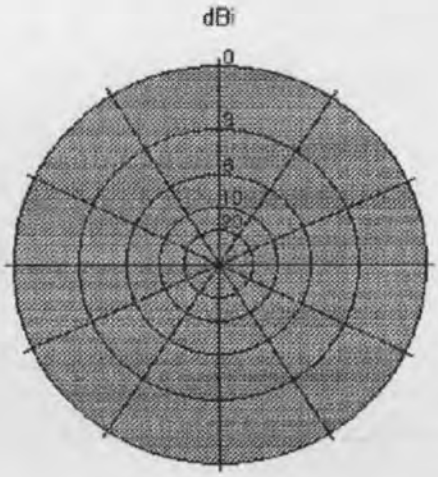

Horizontal pattern (top view)

Appendix C

Non-Systematic Noise Measurement Venues

Measurement Venues	**Zone 50 Australian Map Grid (AMG) Co-ordinates**
Edith Cowan University, Joondalup Drive, Joondalup. Lecture theatres, Library, Computing centre, Staff common room, PABX room, Administration main office, Student accommodation, Canteen and restaurant, Main car park, Joondalup Drive (road edge).	38350XmE 648630XmN
Curtin University Of Technology, Hayman Road, Bentley. Australian Telecommunications Research Institute building, Lecture theatres, Library, Campus radio station (6NR) Studios, Main canteen and tavern, Hayman Road (road edge).	39551XmE 645820XmN
Richmond Primary School, Osborne Road, East Fremantle. Class rooms, Main office, Play ground, Canteen, Library, Computer room, Sports oval, Osborne Road (road edge).	38370XmE 645474XmN

Measurement Venues	Zone 50 Australian Map Grid (AMG) Co-ordinates
Radio Station 100 fm, Canning Highway, East Fremantle. Main office, Studios, Master control room, Stand-by diesel and power room, Record library, Canning Highway (road edge).	38307XmE 645421XmN
Radio Station 100 fm Transmitter Site, Pier Street, East Fremantle. Transmitter hut, Base of the transmitting mast, Water Authority pumping station, Pier Street (road edge).	38381XmE 645505XmN
Wilson's Engraving Works, Westchester Road, Malaga. Main engraving work area, Administration office, Car park, Westchester Road (road edge).	39400XmE 647500XmN
Telstra Perth Head Office, Stirling Street, East Perth. Ground floor cafeteria, Ground floor gymnasium, Lift well, Library, Open office areas on the 5th and 6th floors, Main car park, Stirling Street (road edge).	39257XmE 646444XmN
Town of East Fremantle Works Depot, Allen Street, East Fremantle. Workshop area, Car park, Foreman's office, Allen Street (road edge).	38370XmE 645385XmN
Wanneroo Road, Balcatta. Wanneroo Road (road edge).	38985XmE 647126XmN
South Perth River Foreshore, South Perth. Sir James Mitchell foreshore parkland.	39200XmE 646175XmN

Measurement Venues	Zone 50 Australian Map Grid (AMG) Co-ordinates
Edgewater Train Station, Edgewater. Station main platform.	38424XmE 648400XmN
East Fremantle Football Club, Moss Street, East Fremantle. Main office, Car park, Hotel bar, Functions room, oval, Press boxes, Moss Street (road edge).	38360XmE 645365XmN
Whitford City Shopping Centre, Whitfords Avenue, Hillarys. Public shopping malls, Food hall, Car park, Goods delivery area, Security staff office area, Management offices, Whitfords Avenue (road edge).	38158XmE 648130XmN
Telstra Mobile Telephone Base station site, Ocean Reef Road, Woodvale. Base station hut and mast area.	38450XmE 648330XmN

Appendix D

Computer program for Rician k-factor testing

```
%%%%%%%%%%%%%%%%%%%%%%%%%%%%%%%%%%%%%%%%%%%%%%%%%%%%%%%%%%%%%%%%%%%%%%%%
%Matlab © program for Kolmogorov-Smirnov testing measured and
hypothesis CDF for a range of k.

%%%%%%%%%%%%%%%%%%%%%%%%%%%%%%%%%%%%%%%%%%%%%%%%%%%%%%%%%%%%%%%%%%%%%%%%
format long e
load RECT4.M
y_in=RECT4(500:109934,2);
%
%%%  5th Order Butterworth Filter
[b,a]=butter(5,40/5512.5);
y_out=filter(b,a,y_in);
%
%%%  Median
y_lin=10.^(y_out/10.);
m=median(y_lin);
m=10.*log10(m);
%
%%%  Norm
m=72.5*m-63;
y=72.5*y_out-63;
y=y-m;
%
%%%  CDF Measurement
[n,x]=hist(y,194);
n=n/(109934-500+1);
```

```
n=cumsum(n);
%
%%%  Plot Measurement
plevel=x;
cdf=n;
plottype='+';
german=0;
rayplot(plevel,cdf,plottype,german)

%
%%%  hypothesis
for k=0:15

  %
  %%%  CDF Ricean; k -> shift_k
  clear I F P x_k median_k cdf_k
  steps=200;
  x_k=linspace(-30,20,steps);

  for i=0:50
    I(i+1,1:steps) = besseli(i,sqrt(2*k)*10.^(x_k./20));
    F(i+1,1:steps) = (sqrt(2*k)./10.^(x_k./20)).^i;
  end
  P = I.*F;
  SC= sum(P);
  cdf_k = 1-exp(-(k+10.^(x_k./10)/2)).*SC;

  median_k=(cdf_k-0.5).^2;
  [Y,I]=min(median_k);
  shift_k=x_k(I);
  x_k=x_k-shift_k;

  plottype='--';
  german=0;
  rayplot(x_k,cdf_k,plottype,german)
  set(gca,'FontSize',18,'Fontname','roman')

  %
  %%%  CDF Ricean; k -> delta_k
  clear I F P x_k median_k cdf_k
```

```
  [ra,ca]=size(x);
  x_k=x+shift_k;

  for i=0:50
    I(i+1,1:ca) = besseli(i,sqrt(2*k)*10.^(x_k./20));
    P(i+1,1:ca) = (sqrt(2*k)./10.^(x_k./20)).^i;
  end
  P = I.*P;
  SC= sum(P);
  cdf_k = 1-exp(-(k+10.^(x_k./10)/2)).*SC;

  median_k=(cdf_k-0.5).^2;
  [Y,I]=min(median_k);
  x_k=x_k-x_k(I);

  plottype='o';
  german=0;
  rayplot(x_k,cdf_k,plottype,german);
  set(gca,'FontSize',18,'Fontname','roman');

  [Y_k,I_k]=max(abs(cdf_k-cdf));

  D(k+1)=100*Y_k;
  X(k+1)=x_k(I_k);
  K(k+1)=k;
end

[Y_best,X_best]=min(D);

D_min=D(X_best);
X_min=X(X_best);
K_fac=K(X_best);

fid = fopen('hyp4.dat','w');
  fprintf(fid,'** Fitting for RECT4.M **\n\n');
  fprintf(fid,'   D\t    X\t    K\n\n');
  for k=0:15
    fprintf(fid,'%6.3f\t %6.3f\t %6.3f\n', D(k+1), X(k+1), K(k+1));
  end
  fprintf(fid,'\n\nD_min = %6.3f\n\n',D_min);
```

```
  fprintf(fid,'X_min = %6.3f\n\n',X_min);
  fprintf(fid,'K_fac = %6.3f\n\n',K_fac);
status = fclose('all');
```

Appendix E

Computer program for conversion of the Average Peak Power measurements to Average Peak Electric Field Intensity values

```
%%%%%%%%%%%%%%%%%%%%%%%%%%%%%%%%%%%%%%%%
%Matlab © program for converting an array of Average Peak Power
Measurements to an array representing Average Peak Electric Field
Intensity.

%%%%%%%%%%%%%%%%%%%%%%%%%%%%%%%%%%%%%%%%

format long e
load dBm.M
D=dBm;

%
%%%  Convert a measured dBm power in 50 ohms to watts in 50 ohms

X=D./10;
W=(10.^(X)).*(1000.^(-1));

%
%%%  Convert watts to voltage across 50 ohms

V=(W.*50).^(0.5);
```

```
%
%%% Compute antenna factor for twenty bin centre frequencies

F=(2.305:0.01:2.495);
A=(20.*log10(F))+28.18194;

%
%%% Calculate the Average Peak Electric Field Intensity for each bin
centre frequency in dBUv/m

Er=(10.^(A./20)).*V;
Uv=Er.*1000000;
dBUv=20.*log10(Uv);

%The array for the variable dBUv contains the Average Peak Electric
Field Intensity values for each bin centre frequency.
```

Appendix F

Characterisation of Channel Impulse Response

In this Appendix an analysis of the indoor radio propagation channels impulse response for propagation frequencies in the 2.4 GHz-ISM band is undertaken. In Chapter 3 the basic equations for determining the electric field intensity E_i of all single propagation path signals as a function of distance or range (r) (which is termed $E_i(r)$) was developed. The equations are further developed to include the directional characteristics of the transmit and receive antennas and the respective exit angles and incidence angles for each path. These equations provide the basis to a method of characterising the indoor radio propagation channel in the time domain which is described in this appendix . For our characterisation the channel is kept static, and as such has zero motion of people, transmit antenna, or receive antenna, and therefore considered as time invariant. The superposition of all discrete paths E_i results in the total received field strength. The wideband impulse response measurements have been made using a vector network analyser and an associated scattering parameter (s-parameter) test set. The measurements were conducted within the laboratory used for the fading measurements.

F.1 Impulse Response Measurement System

Equation (3.6) provides the relationship between the channels impulse response $h(\tau,r)$, and the received electric field intensity E_i for each discrete path i contributing to the delay profile. This equation is valid from the theoretical perspective where

isotropic transmit and receive antennae are an inherent part of modelling the impulse response. The use of real physical antennae introduces the additional consideration of the transmit and receive antenna patterns. The effect of a real antenna pattern is equivalent to weighting each path, i, by a value dependent on the transmit and receive aspect angles of the reflector or scatterer as "viewed" initially by the transmit antenna and then finally by the receive antenna. If a direct line of sight path exists, then again the transmit and receive antenna patterns will directly influence the received field intensity E_i. Equation (3.6) is therefore modified to show antennae pattern dependence as follows:

$$h(\tau,r) = \sum_{i=1}^{n} A_R(\alpha_{Ri},\beta_{Ri})E_i(r)e^{-j2\pi f_c\tau_i}R_i\delta(t-\tau_i)A_T(\alpha_{Ti},\beta_{Ti}) \qquad (F.1)$$

where:

α_{Ri} - azimuth angle of incidence at the receive antenna with respect to the last point of scatter,

β_{Ri} - elevation angle of incidence at the receive antenna with respect to the last point of scatter (or reflection),

α_{Ti} - azimuth angle of exit from the transmit antenna with respect to the first point of scatter (or reflection),

β_{Ti} - elevation angle of exit form the transmit antenna with respect to the first point of scatter (or reflection),

R_i - reflection coefficient of the ith path,

τ_i - propagation delay of the ith path,

A_R - directional characteristic of the receive antenna,

A_T - directional characteristic of the transmit antenna,

f_c - radio wave carrier frequency,

$\delta(t)$ - dirac delta function,

E_i - received electric field intensity of the i^{th} path.

The impulse response obtained by channel measurement m(t) is further modified by the impulse response of the measurement system itself s(t) which included connection cables and a receive amplifier to improve the signal to noise ratio of the system. This is accounted for in the analysis of measurements by the convolution of $h(\tau,r)$ with the measurement system impulse response s(t):

$$m(t) = h(\tau,r) * s(t) \tag{F.2}$$

The value of the instantaneous received power, (W_R), is of main interest, and is plotted as the ordinate in all power delay profiles. The instantaneous received power is given by:

$$W_R(t) = K_2 e(t) e^*(t) \tag{F.3}$$

where * indicates complex conjugate, and the complex instantaneous electric field strength e(t) is:

$$e(t) = E_{MAX} m(t) = \left(\sum_{i=1}^{n} E_i\right) m(t) \tag{F.4}$$

K_2 is derived form the receive antenna's effective aperture (A_{Reff}) as follows [43]:

$$A_{Reff} = G_R \frac{\lambda^2}{4\pi} \tag{F.5}$$

where:

A_{Reff} - receive antenna effective aperture,

G_R - maximum gain of receive antenna,

λ - wavelength of radio wave carrier.

Using the relationship given in Equation (F.5) it can be shown that the effective aperture A_{Reff} is the ratio of the power available at the receive antennae terminals W_R, to the power per unit area of the appropriately polarised incident wave P_{AV} [43]. That is:

$$W_R = P_{AV} A_{Reff} \tag{F.6}$$

Substitution of P_{AV} from Equation (3.14) gives:

$$W_R = \frac{1}{2}\frac{E_0^2}{\eta} G_R \frac{\lambda^2}{4\pi} \tag{F.7}$$

For free space condition from (3.11) $\eta = \eta_0 = 120\pi$, then:

$$W_R = E_0^2 \frac{G_R \lambda^2}{960\pi^2} = E_0^2 K_2 \tag{F.8}$$

where:

$$K_2 = \frac{G_R \lambda^2}{960\pi^2} \tag{F.9}$$

$W_R(t)$ is a stochastic variable which is dependent on the statistical properties of the superposition of all single complex propagation path signals E_i. A received power profile of $W_R(t)$ is computed and displayed by the wide-band impulse response measurement system shown as Figure 64. The Hewlett Packard HP8753C network analyser and the associated S-parameter test set 85047A provide data on the frequency domain response of the overall system. A Mini-Circuits ZFL-2000 RX amplifier is included to improve the receive signal to noise performance of the measurement system, and to increase the dynamic measurement range. The RF TX cable, calibrated monopole transmit antenna, calibrated monopole receive antenna, RF RX cables, and RX amplifier behave as a two port network. By selection of S-parameter S21, the complex forward transmission coefficient frequency domain data

that includes both magnitude and phase is measured. By application of optional software installed in the HP8753C network analyser, the frequency domain data is Inverse Fourier Transformed (IFT) to time domain data equivalent to the variable m(t) given in Equation (F.2). As can be seen from this equation, m(t) is a convolution of the indoor radio channels impulse response $h(\tau,r)$, and the measurement systems impulse response s(t). It therefore includes the affects of the monopole antennae, RF connective cables, and Mini-Circuits ZFL-2000 RX amplifier.

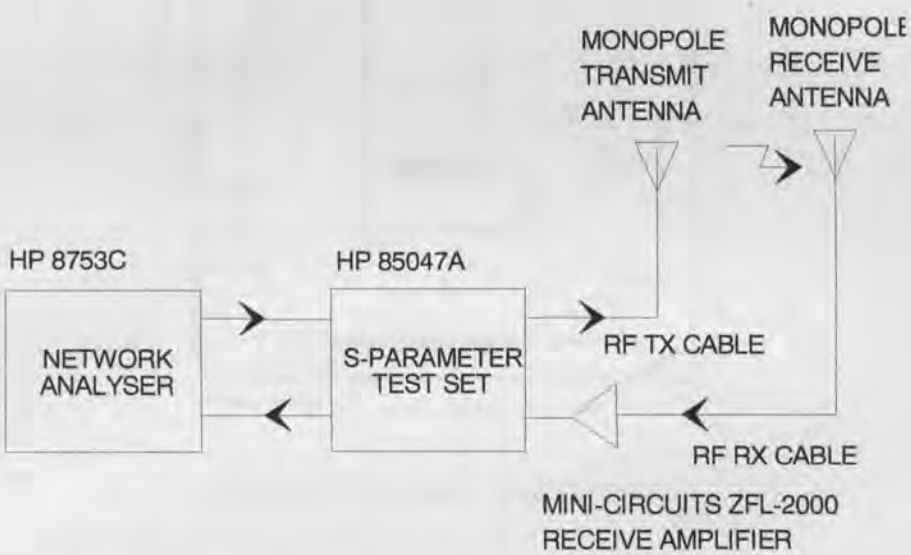

Figure 64: Wide-band Impulse Response Measurement System.

F.2 Building Topology

As previously stated the laboratory is the same venue used to gather fading data, and its physical structure and dimensions are discussed in Section 6.2. A plan view of the laboratory with the antenna positions used for the impulse response measurements is shown in Figure 65.

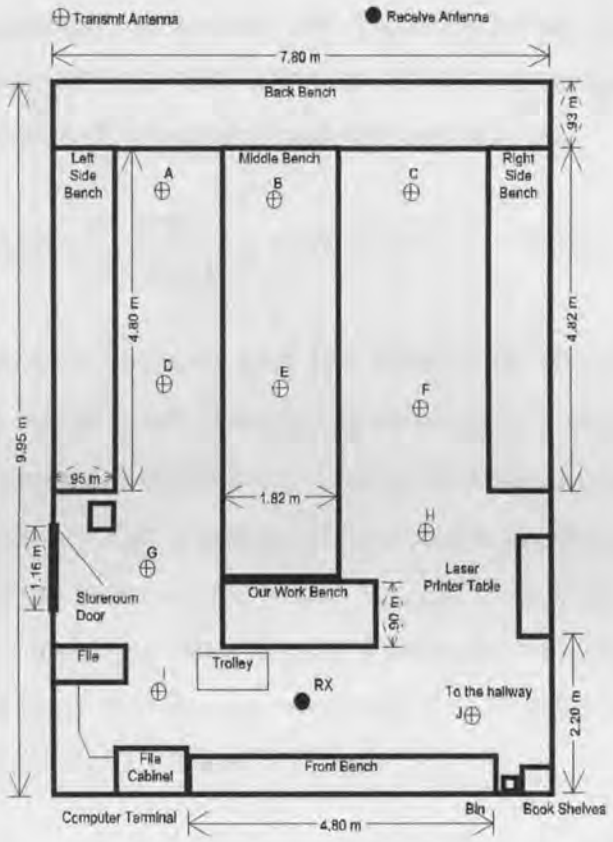

Figure 65: Plan view of the laboratory.

F.3 Measurement Procedure

The measurement data obtained by the system in the frequency domain consists of both amplitude and phase information representative of m(f). This data is at equally spaced points in a selected frequency band of the frequency domain. The important measurement parameter is the frequency span, as it is this parameter that determines the achievable time resolution (τ_{RES}) in the time domain after the IFT operation is performed. τ_{RES} is given by:

$$\tau_{RES} = \frac{1}{\text{frequency span}} \tag{F.10}$$

The relationship between the frequency span and the measurement time span is:

$$\text{measurement time span} = \frac{\text{number of frequency points} - 1}{\text{frequency span}} \tag{F.11}$$

For all our measurements we selected 801 frequency points, and a time span of 135.48 ns (225.48 ns – 90 ns), this selection allows the frequency span to be computed from Equation (F.11) (after transposition) as follows:

$$\text{frequency span} = \frac{800-1}{135.48\times10^{-9}} = 5904.930617 \quad [\text{MHz}]$$

Substituting this value of frequency span into Equation (F.10) results in a value for τ_{RES} of 0.16935 ns, which is the measurement resolution that can be achieved in the time domain. The frequency distance (Δ_f) between successive samples is simply the frequency span divided by 800. The value of Δ_f is used to determine the unambiguous range (R_{UNAMB}) of the measurement, where R_{UNAMB} is defined as the range over which $W_R(t)$ can be unambiguously related to a particular transmitted pulse. Aliasing occurs for distances larger than R_{UNAMB} as a result of under sampling in the frequency domain. R_{UNAMB} is given by Equation (F.12) as:

$$R_{UNAMB} = \frac{c}{\Delta f} \qquad (F.12)$$

where:

c - the speed of light [3×10^8 metres/second].

By substitution of Δ_f into Equation (F.12), then R_{UNAMB} is calculated as 40.644 metres for all measurements. The probability of receiving reflected multipath signal components of significant magnitude after propagation over path lengths in excess of the R_{UNAMB} distance of 40.644 metres is considered negligible for a measurement venue possessing the dimensions shown in Figure 65. The affect of aliasing on the measurement data can therefore be excluded. An accepted technique used in the analysis of data obtained from radio channel impulse response measurements is the division of the impulse response time axis into small time intervals called "bins". Each bin is assumed to contain either one multipath component or none at all. τ_{RES} has been suggested as a reasonable bin size because two or more received multipath components arriving within a bin time frame cannot be resolved as distinct paths by the measurement system [26]. This technique is adopted for all our measurement

analysis, and the selection of bin sizes equal to τ_{RES} when calculating impulse response statistics is made.

For all measured impulse response profiles, the excess time delay of the multipath components are referenced to the time delay of the first signal to arrive. This signal which intuitively arrives over the shortest path is defined as the path $i = 0$ in Equation (3.6), and for computation purposes it is given a normalised reference time of 0 seconds. The data representing the measured magnitude of the received impulse profile ($W_R(t)$) are also normalised to the magnitude of the first arrival path ($i = 0$). The selection of a threshold value for $W_R(t)$ below which the multipath received power level is no longer included in the summation calculations given in Equations (3.23) and (3.24) is important. Lowering the threshold value includes more multipath components at longer time delays thereby increasing the computed value of σ_τ. Therefore the calculated value of σ_τ is determined by the selection of a threshold value, and this threshold value must be chosen with the aim and objectives of the measurements in mind. The selection of a threshold value has been addressed by some researchers, and [70] suggests that the measurement system employed in gathering the impulse response data should experience similar path losses as the system proposed for use over the indoor radio channel. This approach is supported by logic, as the reception of any multipath components which fall below a threshold value that is representative of large value for received signal to noise ratio, contribute little to the overall BER performance. Therefore the method of performing impulse response measurements where the maximum instantaneous receive power level of $W_R(t)$ for the impulse response measurements has been selected to approximate the typical receive power levels of commercially available radio data systems is adopted in our measurements. The threshold value for $W_R(t)$, below which the multipath received power level is no longer included in statistical calculations, is selected as 30 dB lower than the normalised value of the magnitude of the first arrival path ($i = 0$) in each impulse response measurement profile. The selection of this 30 dB threshold meets the large value of received signal to noise criteria mentioned previously, and measurements have shown that any interfering multipath components with instantaneous power levels that are below this level, contribute little to the overall BER performance of data transmission links.

To characterise the measurement system's impulse response s(t), a calibration impulse response measurement was performed in an open flat field with the transmit and receive antennae placed at 6 metres separation, each mounted at 2.5 metre height above ground level on the stands shown in Figure 7. Apart from the 6 metre direct path between the antennae, and a possible ground reflected path, the nearest reflective surface was 250 metres distant from the receive antenna. The multipath reflections from this or other more distant surfaces can therefore be easily identified by the analysis of the time versus amplitude relationship of the calibration measurement. An allowance of 0.3 ns per metre for the propagation velocity of the wave, and the known distance to these distant reflecting surfaces, provided an estimation of the time position in the impulse response profile where the amplitude may be influenced by the multipath reflections produced from them. The affect of any multipath signal contributions with long time delays can therefore be identified, and not included in the calculation of delay spread parameters that are related only to the measurement system itself. The affect of the possible ground reflection on s(t) was tested by the completion of a further series of impulse measurements, where for each measurement a localised movement of one half wavelength of the receive antenna was made. This movement being initially toward, and then away from the transmit antenna, to vary the range between antennae from 6 metres to 5 metres, and then 5 metres to 7 metres. With each movement of 6.25 cm corresponding to a distance of one half wavelength for the mid-band frequency of 2.4 GHz, the receive antenna was moved through a total distance of 32 half wavelengths. Analysis of the impulse response data, after each movement of the receive antenna, showed the affect of the ground reflected path to be negligible, and as such the measurement system's impulse response, s(t), is characterised from the open field measured response and depicted as Figure 66. From Figure 66 it can be seen that for our 6 metre direct path the relative maximum value of instantaneous received power ($W_R(t)$) is -80.837 dBm, and it occurs at a measurement time of 142.5 ns. In Figure 66 the abscissa time span is 90→225.48 ns, therefore each of the ten horizontal divisions is equal to 13.548 ns in width. The ordinate is a base ten logarithmic scale of 5 dB per division.

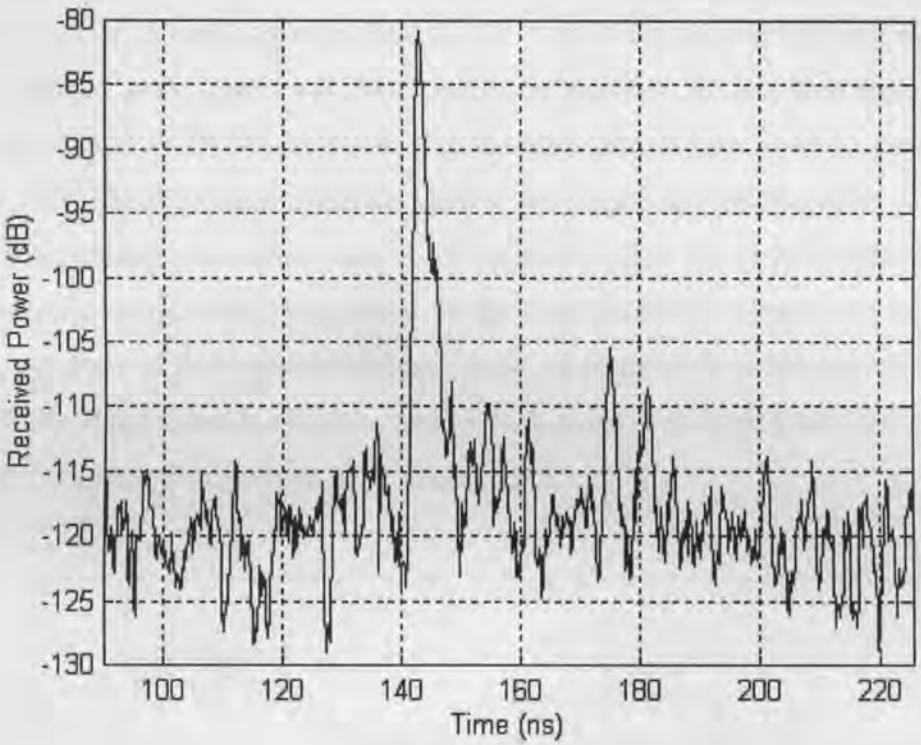

Figure 66: Impulse Response of the Measurement System.

F.4 Measurement Results

Impulse response measurements were performed for transmit antenna placements at positions C, J, D, and F shown in Figure 65. These placements being selected to match those where fading data were analysed in Chapter 6. The receive antenna was also placed at the same position as for the fading measurements, and the motion of people kept at zero. The impulse response data obtained is therefore for a static channel situation, and as discussed in Section 6.3 the motion of people, motor vehicles, and other objects external to the laboratory had no impact on the measurements. The impulse response plots are terminated where the average receive power level, calculated over a sliding window for twenty consecutive time points, approaches a value of 30 dB below that of the shortest and hence first arrival path value (i = 0). The nominal value of 30 dB is the threshold level discussed and selected in F.3. For the transmit antenna placements C, J, D, and F it can be seen from the impulse response plots shown as Figures 67, 68, 69, and 70 respectively, that the time taken for the received power to fall below the 30 dB threshold value approximates

50 ns for all positions. At the speed of light this value corresponds to a propagation path length of 15 metres greater than that of the first signal to arrive over the shortest path, defined as the path i = 0. As 15 metres is significantly less than R_{UNAMB} which was calculated as 40.644 metres in F.3, the selection of measurement parameters is supported. These impulse response figures also depict the measurement noise level, which are plotted as series of random values that precede the sudden increase in level to the value representing the arrival of the first resolvable signal over the shortest path. Analysis of the impulse responses noise level shows it to be below the average 30 dB threshold value in all plots, and as such noise is not considered as a source of error in the statistical analysis undertaken in F.5.

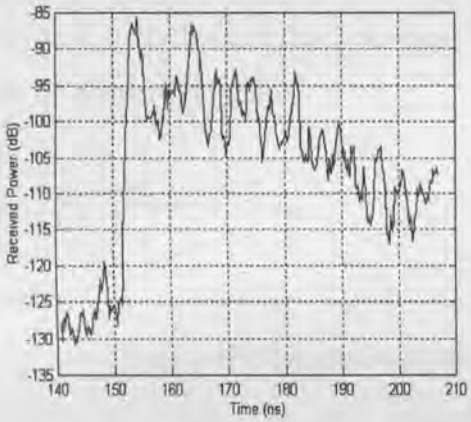

Figure 67: Impulse Response for transmit antenna position C.

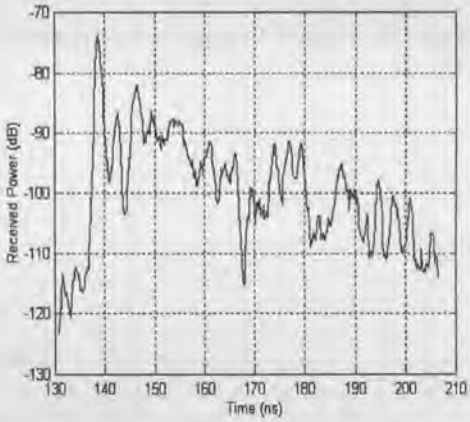

Figure 68: Impulse Response for transmit antenna position J.

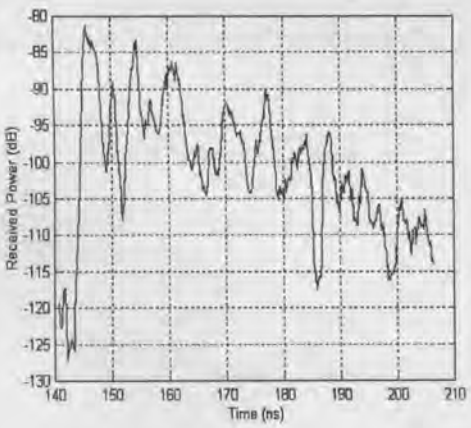

Figure 69: Impulse Response for transmit antenna position D.

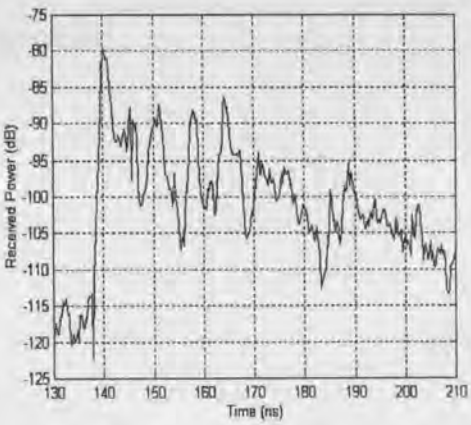

Figure 70: Impulse Response for transmit antenna position F.

F.5 Statistical Analysis

The received power shown as the ordinate in Figures 67-70 is the stochastic variable $W_R(t)$. From Equation (F.8) it can be seen that the instantaneous value of W_R is equal to the product of the constant K_2 and E_0^2. Therefore by the conversion of all measured logarithmic values of W_R to linear values, and then normalising them to the maximum linear value, an array of values representative of Ei^2 is obtained. The substitution of this array and the related time data into Equations (3.24), and (3.23) permits the computation of τ_m and σ_τ respectively. The value of σ_τ calculated from the overall measurement is not equal to the rms delay spread caused by the indoor radio channel alone, an allowance must be made for the system calibration value of delay spread. This value is determined from the open field measurement data obtained in Figure 66. It can be shown [71] that:

$$\tau_m = \tau_{measured} - \tau_{system} \tag{F.13}$$

where:

τ_m - indoor channel mean excess delay,

$\tau_{measured}$ - measurement mean excess delay,

τ_{system} - system calibration mean excess delay.

The relationship between the indoor channel rms delay spread, measured rms delay spread, and system calibration delay spread is given by:

$$\sigma_\tau^2 = \sigma_{measured}^2 - \sigma_{system}^2 \tag{F.14}$$

therefore:

$$\sigma_\tau = \sqrt{\sigma_{measured}^2 - \sigma_{system}^2} \tag{F.15}$$

where:

σ_τ - indoor channel rms delay spread,

$\sigma_{measured}$ - measurement rms delay spread,

σ_{system} - system calibration delay spread.

Table 8 shows the empirical values of τ_m and σ_τ for transmit antenna placements C, J, D, and F. The values were calculated from Equations (3.23), (3.24), (F.13), (F.14), and (F.15) respectively, from measured data using Matlab©.

Table 8: Mean excess delay and rms delay spread

Placement	τ_m (ns)	σ_τ (ns)
C	11.5699	9.8074
J	7.8352	11.5436
D	14.3883	11.0872
F	12.2138	16.4433

F.6 Conclusions

Statistical analysis of the wideband impulse response for the four representative transmit antenna placements (C, J, D, and F), and the fixed receive antenna placement, permitted the calculation of specific values for the static rms delay spread parameter. It should be noted that the calculated values are specific to the antenna placements and for this particular room. The important choice of a venue that provided a static receive level in the absence of motion within the room allowed the values of delay spread to be obtained by the statistical analysis of repeat measurements for the same transmit and receive antenna placements. It is therefore possible to transmit high speed data over the indoor channel using the same antenna placements for which the delay spread statistics were obtained, and by maintaining our static environment, then to determine if there is any perceptible increase in EVM for the received constellation that can be directly attributed to ISI caused by delay spread. By knowledge of the relationship between EVM and systemic noise for the data measurement system, as given in Figure 10, then by deduction the affect, if any,

of σ_τ on EVM can be determined, with the proviso that its impact on the change to EVM magnitude falls within the measurement accuracy of the system. The values obtained for σ_τ at 2.4 GHz are in agreement with those obtained from measurements and analysis performed by other researchers [41], [72], at venues of similar size and comparable construction materials. The calculated values of σ_τ for the 2.4 GHz frequency band in [72] fall within the range of 7.4-23.1 ns. In Chapter 7 we consider the affect of σ_τ on BER.